17430

NATIONAL LIBRARY
OTTAWA

CANADA

BIBLIOTHÈQUE NATIONALE
OTTAWA

NAME OF AUTHOR..David Andreasen.....

TITLE OF THESIS...Fatigue Crack Propagation in Pipeline Steels.....

.....

UNIVERSITY...of Alberta.....

DEGREE FOR WHICH THESIS WAS PRESENTED...M.Sc. Metallurgical Eng.

YEAR THIS DEGREE GRANTED..1973.....

Permission is hereby granted to THE NATIONAL LIBRARY OF CANADA to microfilm this thesis and to lend or sell copies of the film.

The author reserves other publication rights, and neither the thesis nor extensive extracts from it may be printed or otherwise reproduced without the author's written permission.

(Signed).David Andreasen.....

PERMANENT ADDRESS:

[redacted]045-86 ave.....

[redacted]monton alta.....

.....

DATED....June 1.....1973

NL-91 (10-68)

THE UNIVERSITY OF ALBERTA

FATIGUE CRACK PROPAGATION IN PIPELINE STEEL

by

© DAVID H. ANDREASEN

A THESIS

SUBMITTED TO THE FACULTY OF GRADUATE STUDIES AND

RESEARCH IN PARTIAL FULFILLMENT OF THE REQUIREMENTS

FOR THE DEGREE OF MASTER OF SCIENCE

IN METALLURGICAL ENGINEERING

DEPARTMENT OF MINING AND METALLURGY

EDMONTON, ALBERTA

FALL, 1973

THE UNIVERSITY OF ALBERTA

FACULTY OF GRADUATE STUDIES AND RESEARCH

The undersigned certify that they have read, and recommend to the Faculty of Graduate Studies and Research for acceptance, a thesis entitled

FATIGUE CRACK PROPAGATION IN PIPELINE STEEL

submitted by DAVID H. ANDREASEN

in partial fulfillment of the requirements for the degree of Master of Science in Metallurgical Engineering.

Franz Ritter

W. R. Chitwood

Date May 25, 1973

ABSTRACT

The effect of temperature, environment and heat treatment on the fatigue crack propagation rates in a fine grained pipeline steel corresponding to A. P. I. specifications 5L Grade B and/or 5LX-X42 were investigated. Constant deflection bending fatigue tests at 640 c. p. m. were conducted on single edge notched specimens which contained a 1/16 inch diameter key hole notch as a stress riser. A fatigue machine was designed and built specifically for this project. The fatigue tests were performed at -50, -10, 21 and 71 ^{o}C in argon and at -50 and 21^{o} C in hydrogen at ambient pressure. One set of specimens was heat treated to explore the effect of grain size on crack propagation rate. The grain size increased from 0. 022 mm to 0. 026 mm.

The surface plastic zones and reversed plastic zones were photographed to determine if any correlation could be made between the size or shape of the zones and the fatigue crack growth rates. The fatigue fracture surfaces were studied with both the scanning electron microscope and the transmission electron microscope.

In addition to fatigue tests, static tensile tests at strain rates of 0. 2 and 0. 002 in/in/min, cyclic tensile tests and impact tests were carried out at the four test temperatures.

The data were evaluated in terms of the crack propagation rates (da/dN) as a function of ΔK, according to $da/dN = C\ \Delta K^{m}$.

The values of m varied from a low value of 2.66 at 71 °C to a maximum of 6.81 at -10° C after which it decreased to 4.49 at -50 °C. The values of C varied inversely to those of m and it was found that a relationship of the form $m - m_o = A \ln C$ holds for a wide variety of materials. The experimentally determined relationships were compared to a theoretically derived crack growth law due to Tomkins (54) and a close correlation is found if cyclic material properties are used.

Hydrogen at ambient pressure had no significant effect on crack initiation life or initial crack growth rates, however after an incubation period crack growth rates an order of magnitude faster occurred. A critical ΔK value of 20-22 ksi $\sqrt{in}$ was sufficient to cause unstable crack growth. Reversed plastic zone sizes and cyclic stress-strain data show a much better correlation with fatigue properties as these properties are affected by strain ageing.

ACKNOWLEDGEMENTS

I wish to thank Dr. F. H. Vitovec for providing guidance and encouragement over the span of both my undergraduate and graduate studies.

I would also like to extend my appreciation to Mr. T. Forman, Mr. B. Snider, Mr. G. Chaisson and Mr. R. M. Scott for their able technical assistance.

A special acknowledgement to the Steel Company of Canada Limited for supplying the sample material used in this project.

This work was supported by the National Research Council of Canada under Grant number A2926.

TABLE OF CONTENTS

			Page
1.	INTRODUCTION		1
2.	EXPERIMENTAL PROCEDURE AND PROGRAM		3
	2.1	Introduction	3
	2.2	Test Material	3
	2.3	Microstructure	4
	2.4	Charpy Impact Test Results	4
	2.5	Heat Treatment	5
	2.6	Specimen Preparation	6
	2.7	Static and Cyclic Stress-Strain Data Determination	7
		2.7.1 Static Tensile Tests for Stress-Strain Data Determinations	7
		2.7.2 Cyclic Stress-Strain Data Determination	8
	3.0	Calculation of Stress Intensity Factor	8
	4.0	Testing Machine and Testing Procedures	9
	4.1	Eccentrics	10
	4.2	Connecting Rod and Load Cell	10
	4.3	Extension Arm	11
	4.4	Specimen Chamber	11
	4.5	Grips and Temperature Control	12
	4.6	Crack Length Measurement	14
	4.7	Calibration	14

TABLE OF CONTENTS - cont'd

		Page
5.	EXPERIMENTAL RESULTS	15
5.1	Crack Front	15
5.2	Crack Length Versus Number of Cycles	15
5.3	Crack Initiation	16
5.4	Crack Growth Rate Versus ΔK	18
5.5	Fatigue Life	19
5.6	Hysteresis Loops	20
5.7	Cyclic Stress-Strain Curves	20
6.	ANALYSIS AND DISCUSSION	21
6.1	Analysis Based on Fracture Mechanics	21
6.2	Analysis Based on Fatigue Mechanisms	29
6.3	Crack Nucleation	29
6.4	Fatigue Crack Propagation	39
6.5	Analysis of the Tomkins Model	49
SUMMARY AND CONCLUSIONS		56
TABLES		58
FIGURES		82
REFERENCES		127
APPENDIX 1	The Effect of Mean Stress on Fatigue Crack Propagation Rates	134

TABLE OF CONTENTS - cont'd

		Page
APPENDIX 2	Calculation of Temperature Maximum in the Reversed Plastic Zone Calculated from a Cylindrical Heating Source Embedded in a Similar Matrix	137
APPENDIX 3	Maximum Temperature in the Reversed Plastic Zone as Calculated from a Slip Plane Model	140

LIST OF TABLES

Table		Page
I	Chemical Composition and Mechanical Properties of Test Material	59
II	Results of Charpy Impact Tests	60
III	Static Tensile Test Data as a Function of Temperature and Strain Rate	61
IV	Cyclic Stress-Strain Data as a Function of Temperature	62
V	Experimental Data From Cyclic Stress-Strain Tests	63
VI	Experimental Data from the Crack Growth Rate and Stress Intensity Calculations	65
VII	Number of Cycles to Crack Initiation for the Various Testing Conditions	76
VIII	Constants C and m as Determined from Experimental Data	76
IX	Fatigue Life in Cycles for the Various Test Conditions	76
X	Experimental Data Illustrating the ln C and m Relationship	77
XI	Calculations of Diffusion Coefficients for Carbon and Nitrogen in B. C. C. Iron as a Function of Temperature	79
XII	Comparison of Crack Initiation Times with Various Material Properties	80
XIII	Size of Plastic Zones in Steel Specimens	81
XIV	Crack Propagation Rates as a Function of Temperature for the Experimental Data and for the Tomkins Equation	81

LIST OF FIGURES

Figure		Page
1	Microstructure of Test Material	83
2	Schematic Drawing Showing the Test Specimen Orientations with Respect to the Rolling Direction	84
2A	Manganese Sulphide Inclusion Content of Test Material	85
3	Charpy Impact Energy Curves for the Test Material as a Function of Temperature and Specimen Orientation	86
4	Test Specimens used for Cyclic, (upper) and Static Stress-Strain Data Determinations	87
5	Schematic Drawing of the Fatigue Testing Machine	88
6	Photograph of Fatigue Testing Apparatus	89
7	Load versus Time (a) and Load versus deflection loop (b)	90
8	Close up of the Bottom Grips with the Specimen in place.	91
9	Fracture Surface of a Fatigue Test Specimen Which Illustrates the Crack Front	92
10	Typical Crack Length Versus Number of Cycles for the Four Test Temperatures and Argon Environment	93
11	Typical Crack Length Versus Number of Cycles for Specimens Tested in Hydrogen and the Heat-Treated Specimens Tested in Argon	94
12	Crack Propagation Rate as a Function of Stress Intensity Range for Tests in Argon at 20 and 70 °C	95

LIST OF FIGURES - cont'd

Figure		Page
12A	Crack Propagation Rate as a Function of Stress Intensity Range for Tests in Argon at -50 and -10°C	96
13	Crack Propagation Rate as a Function of Stress Intensity Range for the Heat-Treated Specimens Tested in Argon at -50 and 20°C	97
14	Crack Propagation Rate as a Function of Stress Intensity Range for Specimens Tested in Hydrogen at -50 and 20°C	98
15	Static and Cyclic Stress-Strain Curves at the Four Test Temperatures	99
16	Schematic Drawing of the crack Growth Rate Versus the Stress Intensity Range Which Illustrates the Sigmoidal Shape (5)	100
17	Slope m versus ln C for a Wide Range of Materials and Testing Conditions According to Equation 4	101
18	Predicted Relationship Between ln da/dN and ln ΔK as Calculated from the Relationship Between ln C and m Shown in Figure 17	102
19	Relationship between ln (da/dN), ΔK, and m shown as a Surface	103
20	Mean Crack Propagation Rate as a Function of ΔK as Found in This Research for the Four Test Temperatures	104
21	Effect of Ageing Time at Room Temperature after Straining on the Yield Stress and Hardness	105
22	Effect of Strain Rate on the Yield Strength, Ultimate Tensile Strength, and True Stress at Maximum Load as a Function of Test Temperature	106

LIST OF FIGURES - cont'd

Figure		Page
23	Variation of Average Fatigue Life, Crack Propagation Life, and Crack Initiation Life as a Function of Temperature for Tests in Argon	107
24	Variation in Flow Stress as a Function of Strain Rate, Strain and Test Temperature	108
25	Variation of the Cyclic Yield Stress and the Cyclic Ultimate Tensile Stress as a Function of Temperature	109
26	Schematic Illustration of the Plastic Blunting Model for Fatigue Crack Growth (38)	110
27	Fractographs Illustrating Fatigue Striations for Tests at 21 °C in Argon	111
28	Scanning Electron Micrograph for a Fatigue Test at 21 °C in Argon Showing the Localized Patches of Fatigue Striations	112
29	Cycle-dependent Stress Relaxation of a Specimen Initially Subjected to a mean Tensile Stress (63)	113
30	Schematic Illustration of the Stress at the Crack Tip Showing the Reversed and Monotonic Plastic Zones (39)	114
31	Effect of the State of Stress on the Shape of the Fatigue Crack Front. Transition from Plane Stress at the Surface to Plane Strain in the Center of the Specimen	115
32	Surface Plastic Zone Showing the Progressive Formation of Luders Bands as the Crack Propagates	116
33	Photographs of the Surface Plastic Zones at the Four Test Temperatures	117

LIST OF FIGURES - cont'd

Figure		Page
34	Reversed Plastic Zones as Revealed by Etching of the Dense Substructure in the Plastically Deformed Region	118
35	Radius of the Reversed Plastic Zone as a Function of Temperature for Tests in Argon	119
36	Crack Initiation Life, Total Life, and the Inverse of the Reversed Plastic Zone Radius as a Function of Temperature for Tests in Argon	120
37	Scanning Electron Microscope Fractographs of Fatigue Specimens Tested in Hydrogen	121
38	Surface Plastic Zones of Specimens Fatigued in Argon and Hydrogen	122
39	Model of Fatigue Crack Advance due to Shear on 45° Stress Planes (54)	123
40	Surface Plastic Zones for Increasing Crack Length at 21 °C in Argon	124
41	Power Values m and m_t, a Function of Test Temperature	125
42	Slope m_t versus ln C^1 which illustrates the Linear Relationship as shown Previously in Figure 17 for m Versus ln C	126

1 INTRODUCTION

With the recent advances in technology low alloy-low carbon steels in the 50 to 80 ksi yield strength range are now a reality (1). The properties of these new steels are obtained by a combination of grain refinement by means of niobium, vanadium, and rare earth additions, plus a change in the steel processing practice such as rolling to a lower finishing temperature (Low Temperature Thermal Mechanical Treatment, LTTMT) and/or rapid cooling through special quenches or coiling procedure (1)(2)(3)(4). These steels have found uses in such structures as pipelines, refrigerated storage vessels, automobile bumpers, engine mounts and frame members (1). Failure of such structures or components usually result in serious damage.

Fatigue is one of the most common failure mechanisms. Even though fatigue failures have been recognized and studied for more than a century, only recently has structural fatigue been recognized as a field of major concern. The development of low cost high-strength alloys and improved fabrication and joining techniques have led to the production of large structures which must sustain repeated stresses in service. Whereas smaller components can be designed to prevent crack initiation at an increase in cost, large structures must be designed economically, thus the prevention of terminal crack propagation must be considered where much shorter fatigue lives are involved.

Because these advances have taken place in a short period of time much technical data is lacking. In a recent symposium (1) representatives of automobile manufacturers pointed out that more data on formability, corrosion resistance, cyclic yield, and fatigue were required. In another recent paper (6), concerned with metals and alloys for low temperature use, it was pointed out that very little information was available regarding the effect of low temperature on fatigue crack propagation. Clark and Trout (7), have studied the effect of temperature (-100 to 75 °F), and section size on fatigue crack growth rates in a forging grade Ni-Mo-V steel and found that as the temperature decreased the crack growth rate decreased for a given stress intensity. Rolfe and Munse (8), in a study of fatigue crack propagation in mild steel found that as the temperature decreased (78 to -40 °F), the fatigue crack growth rate decreased, however these steels do not resemble the recently developed alloys therefore a close comparison can not be made.

Because little data is available for these steels a study of fatigue crack propagation was initiated. Although fatigue may not be the cause of the final failure, it is often fatigue which causes sub-critical flaws to grow to a size where failure by some other mechanism can take over (6). Fatigue crack growth is affected by many variables, but test temperature and environment seem to be most important and as a result were chosen as the two main variables of this investigation.

2. EXPERIMENTAL PROCEDURE AND PROGRAM

2.1 Introduction

The purpose of this investigation was to study the effect of varying service temperature on the fatigue crack propagation rates in a fine grained pipeline steel. The temperatures selected were -50, -10, 21 and 71 °C, thus ranging from a low ambient temperature to a temperature range where strain ageing effects are significant. To delineate environment effects tests were either performed in dried argon or hydrogen at ambient pressure.

The following data were recorded from the fatigue tests: total fatigue life, number of cycles for crack initiation, crack propagation rate as a function of the range of stress intensity, fatigue striation spacings, and the size of the surface and reversed plastic zone.

In order to analyse and correlate the fatigue data the following additional tests were performed at the four different temperatures: Charpy impact tests, tensile tests at two strain rates (0.002 and 0.2 in/in/min), and cyclic tensile tests.

2.2 Test Material

The test material selected meets A.P.I. 5L Grade B and/or A.P.I. 5LX-X42 specifications. The supply of the 3/8" skelp by S T E L C O is gratefully acknowledged. The material was tested in the as received condition with the exception of one set of test specimens which was given a full anneal by heating to 1750 °F for 15

minutes and then furnace cooled. The chemical composition and mechanical properties are listed in Table 1.

2.3 Microstructure

As in most materials which have been mechanically worked the microstructure has an orientation relationship to the direction of working. The microstructure in the various orientations with respect to the rolling direction is shown in Figure 1. The notation used to describe the orientation with respect to the rolling direction is shown schematically in Figure 2 and will be used throughout the thesis. The microstructure 90° to the rolling direction is a fairly even distribution of pearlite and ferrite. Parallel to the rolling direction the microstructure is "banded". A "banded" structure consists of alternate layers of ferrite and pearlite. The pearlite is separated by two to three grains of ferrite, the average size of which is 0.0223 mm.

Manganese sulphide inclusions are present as indicated by Figure 2A. A. S. T. M. Designation E45 was used to determine the inclusion content (9). The microscopic method was used and it was found that inclusions of Type A were present; their size and distribution density placing this steel below the A. S. T. M. numerical designation of 1, thus indicating a clean steel.

2.4 Charpy Impact Test Results

Impact tests were conducted on the material in a direction 90° to the rolling direction and parallel to the rolling direction as

illustrated in Figure 2. Due to the original plate thickness, the samples were approximately 85% of full size Charpy specimens. As a result the values obtained are comparative only within the group of samples tested. The results are listed in Table II and plotted in Figure 3. The heat-treated specimens tested went from a high value of 73 ft.-lbs. (99 joules) at 70°C to a low value of 4 ft.-lbs. (5.4 joules) at -50°C. The as received specimens went from a high value of 47 ft.-lbs. (63.7 joules) at 70°C to a low of 6.0 ft.-lbs. (8.1 joules) at -50°C. The as received specimens tested 90 degrees to the rolling direction (see Figure 2) went from a high value of 55 ft.-lbs. (74.5 joules) at 70°C to a low of 18 ft.-lbs. (24.4 joules) at -70°C. The two sets of specimens tested parallel to the rolling direction showed at sharp transition at about 10°C, however the specimens tested 90 degrees to the rolling direction did not show this transition and at no time did the energy values fall below 15 ft.-lbs. (20.3 joules). This difference is attributed to the microstructure.

At this point it may be appropriate to mention that no correlation is observed between the impact values and the fatigue life. Kenneford (43) also observed this, in both notched and unnotched specimens.

2.5 Heat Treatment

A number of test specimens were heat treated to increase the ferrite grain size. Since this particular steel contains niobium, the

grain structure can remain stable at relatively high temperatures. Niobium can stabilize grain growth up to 1875 °F in low carbon steels. The test specimens were placed in annealing bags and held at 1750° F for fifteen minutes after the furnace reached temperature. After the soaking time, the furnace was shut off and the test specimens were slowly cooled down to 500 °C before they were removed from the furnace. The heat treatment did not remove the banding but the ferrite grain size increased by 17. 5% from 0. 022 mm to 0. 026 mm. The pearlite did not appear to be affected.

2. 6 Specimen Preparation

Single-edge notched specimens were cut from the plate in the orientation shown in Figure 2. The nominal specimen dimensions were 5 1/2" (139. 7 mm) long by 3/8" (9. 53 mm) thick by 3/4" (19. 05 mm) deep. The specimens were cut from the plate using a continuously cooled band saw. To assure the faces were all 90° to each other, the specimens were finished by milling. No machining operations were performed on the faces perpendicular to the rolling direction. A keyhole type notch used as a stress riser was made by drilling 1/16" (1. 59 mm) diameter hole 3/32" (2. 38 mm) in from the edge. The theoretical stress concentration for this configuration is 3. 25. By drilling a hole rather than machining a notch the orientation of the machining marks were circumferential which does not affect the stress concentration as drastically as does making scratches along the notch root. The metal bridge between the

hole and the specimen edge was cut from the inside to the outer surface with a jewelers saw. In this way damage to the notch root was prevented.

In order to make the crack trace easier to observe in the travelling telescope, the sides of the specimens were polished down to No. 600 grit abrasive. The polishing was done 90° to direction of crack propagation. Some specimens were given a final polish using 6 micron diamond paste. Whereas different finishes on the notch root would affect fatigue life through effects on crack initiation time, it is felt the effect of the two different finishes on the specimen sides is negligible.

2.7 Static and Cyclic Stress-Strain Data Determination

2.7.1 Static Tensile Tests for Stress-Strain Data Determination

Tensile tests were carried out at two strain rates and at the four test temperatures used in this research. Two strain rates, 0.002 in/in/min and 0.2 in/in/min were chosen to indicate whether or not the material was susceptible to strain ageing during straining. In addition tests at two higher temperatures, 180°C and 260°C, were performed at the higher strain rate.

Photographs of the test specimens are shown in Figure 4 and schematically illustrated in Figure 2. The direction of testing with respect to the rolling direction was the same as for the fatigue tests. Testing was performed using an Instron testing machine which was

calibrated to insure that the crosshead movement could be accurately related to the strain. The four test temperatures were maintained by immersing the specimen in a suitable bath for the duration of each test. The two higher temperatures were maintained by enclosing the specimen in a furnace. Data resulting from these tests is listed in Table III.

2.7.2 Cyclic Stress-Strain Data Determination

The cyclic tests were carried out in the fatigue machine using a modified specimen design as shown in Figure 4. The cyclic tests were carried out at the four test temperatures with the control accomplished in the same manner as in the crack propagation tests.

The test procedure involved cycling for a period of time and once the hysteresis loop configuration appeared to be stable a photograph was taken. Immediately after the picture was taken the eccentric was reset to increase the amplitude and the procedure repeated until the specimen failed. The data was evaluated in a method similar to that of Kettunen and Kocks (10), which involved plotting stress versus cumulative plastic strain. The results from these tests are listed in Table IV. The experimental data is given in Table V.

3.0 Calculation of Stress Intensity Factor

The stress intensity factor, K, used in the data analysis is taken from a derivation by Kies (11). The form of the equation is:

$$K = A\, M/Bh^{3/2}\sqrt{1/\alpha^3 - \alpha^3}$$

where A is 4.12 for cantilever loading, M is the bending moment, B and h are the specimen thickness and depth, and α is equal to 1- a/h where a is the total length of crack plus the notch. This equation was also used by Meyn (12) under similar conditions as in this program. The equation is derived for plane strain conditions therefore the plastic zone size should be small compared to the crack length and with the unbroken ligament. The validity of the equation is only compared with experimental data up to a/h being equal to 0.5. A later equation (13) which predicts the same K values for a given specimen size and crack length is accurate up to a/h = 0.8, therefore the equation due to Kies is assumed accurate in the range of a/h values reached in this test program.

4.0 Testing Machine and Testing Procedures

Testing was carried out at 640 cpm on a constant deflection bending fatigue machine which was designed and built for this project. Figures 5 and 6 illustrate the apparatus schematically and as is, respectively.

The specimen is mounted vertically in the bottom grips and an extension arm is attached to the top of the test specimen. The specimen is bent by a variable eccentric which activates the extension arm through a connecting rod which also acts as a load cell. The drive shaft of the eccentric is housed in eccentric bearings which may be

adjusted to change the load range. The lower grip is designed to control the specimen temperature by either heating or cooling a copper extension. The test environment is controlled by a transparent chamber through which the desired gas is flushed during the test. Details of the various parts of the testing machine and procedure are as follows:

4.1 Eccentrics

Two parallel eccentrics are used; one which moves the entire head forward or backward thus changing the center of rotation of the driving eccentric relative to the specimen, the other which changes the deflection amplitude. The amplitude of the driving eccentric is changed by a gear system which may be locked in place once the desired position is determined.

4.2 Connecting Rod and Load Cell

The connecting rod was machined from aluminum alloy 2024-T4 to reduce inertia effects. At each end are self-centering bearings which are threaded into the aluminum rod. By threading the bearings into the rod it is possible to adjust the rod length, making alignment with the position of the extension arm simple. The connecting rod contains a reduced section on which two of four B. L. H. SR-4 strain gauges are mounted. Two of the strain gauges which serve for temperature compensation are mounted on a block of the same material which is attached to the connecting rod.

The load cell was calibrated on an Instron testing machine as

outlined in Section 4. 7.

A Tektronix 561B Oscilloscope combined with a type 3C66 carrier amplifier were used to display the output from the load cell. The most sensitive settings, 10 μ strain/div and full gain were used throughout the test program. The output from the scope was tied in with a Edin model 8002 Oscillograph which provided a visual recording of load versus time. The oscillograph was activated by a timer at intervals of 12. 5 minutes for 8 seconds in order to provide a load recording.

4. 3 Extension Arm

The extension arm is made from a 3/4" steel bar in which a series of various size holes are drilled to reduce the mass. A Linear Variable Differential Transformer (LVDT) is connected to the extension arm to record the deflection amplitude, and in conjunction with the output from the load cell a recording of the load versus deflection hysteresis loop is obtained. A typical load versus time and load versus deflection hysteresis loop is shown in Figure 7.

4. 4 Specimen Chamber

The specimens were all tested under controlled environments at ambient pressure. The chamber was made of a Lucite round which was threaded and sealed into a base plate which is fixed to the lower grip. A glass viewing window and thermocouple holding device are designed into the chamber. A rubber boot was sealed to the top

of the chamber and to a plate fixed to the extension arm thus providing a flexible seal. The impurities in the argon and hydrogen are shown below in parts per million:

	Argon	Hydrogen
Argon	remainder	---
Hydrogen	1 ppm	remainder
Oxygen	5 ppm	5 ppm
Nitrogen	0 ppm	5 ppm
Hydrocarbons	1 ppm	1 ppm
Water	5 ppm	5 ppm
Carbon Dioxide	1 ppm	1 ppm

In addition, the argon and hydrogen were passed through a Matheson Model 450 dryer and a cylinder of anhydrous $CaSO_4$ desiccant to remove additional moisture. The hydrogen was also routed through a liquid nitrogen water trap. The gas entered the chamber through the top plate and a back pressure was maintained by passing the exit gas through an oil bubbler.

4.5 Grips and Temperature Control

In order to obtain the test temperatures the bottom half of the grip system was made from a copper rod encased by a steel round. A slot was milled out of the upper end of the copper rod and the specimen was seated in this slot. The copper lobs were pressed onto the specimen sides by set screws, thus allowing the specimen to contact the copper rod on three surfaces for heat transfer. The back edge of the test specimen was supported against a stainless steel

shim to reduce heat transfer to the testing machine. Another shim was placed at the front edge of the specimen against which two locking bolts pushed. When the specimen was in place the copper lobs were pressed by set screws up to the specimen sides. The top eight inches of the copper rod is centered inside of the thick walled cylinder by a series of set screws to minimize contact area and consequently heat losses are reduced. The copper bar is also insulated and sealed inside the steel holder. The bottom twelve inches of copper rod can be submerged in a Dewar containing either liquid nitrogen, dry ice and acetone, or heated paraffin oil to obtain temperatures of -50, -10 or 71 °C. The bottom grip holder is separated from the main frame by four small stainless steel shims, again to minimize heat transfer.

The top half of the grips which is the extension arm is a box-like system which fits over the specimen and then is held firmly there by a shim and two lock bolts.

The temperature was recorded by a copper-constantan thermocouple which is held against the specimen near the crack plane. It was found that once the temperature reached equilibrium for the various liquids it remained constant. As the crack grew the heat transfer to the upper grip changed and the level of the coolant, or in the case of the higher temperature test, the input current to the heater, was decreased to maintain the correct temperature. A photo-

graph of the grips is shown in Figure 8.

4.6 Crack Length Measurement

The crack length was measured with a 20 power travelling telescope. A rule with 1/64" divisions was placed in the chamber beside the specimen. With this system the crack length could be read to 0.0078 in (0.20 mm) with no difficulty and could be detected at smaller lengths. The readings were taken every 8000 cycles (or every 12.5 minutes) and more often when the crack growth rates were faster as in the cases where hydrogen was used as an environment.

4.7 Calibration

The strain gauges of the load cell were calibrated using an Instron testing machine over a load range of 5 lbs to 100 lbs. Within the load range the load versus displacement plots were linear. A statistical analysis was carried out on the data. A mean value of 0.903 centimeters displacement per ten pounds of load was read on the oscilloscope at a setting of 10 micro strain per division and full gain. The variance and standard deviation were 0.00077 and 0.02774 respectively. The slopes and regression coefficients for the tension and compression calibrations are 0.090 and 0.9998 and 0.0894 and 0.9997 respectively. During the fatigue testing periodic checks were made to insure that the calibration did not change.

5. EXPERIMENTAL RESULTS

The results of this series of tests indicate a definite difference in fatigue crack growth rates as the temperature and atmosphere are varied. Since the results were consistent within each set of tests a large number of repeats was considered unnecessary, however 3 to 7 tests were performed for each testing condition. The experimental data from the crack growth rate versus stress intensity relationship is given in Table VI.

5.1 Crack Front

The typical appearance of the crack front is illustrated in Figure 9. In order that the calculated stress intensity, K, be valid, the deviation of the crack front from linearity must be small. To obtain valid K values according to A. S. T. M. - E 399-70T, the crack trace on either surface must be equal to or greater than 90 % of the "average" crack length; "average" being defined according to A. S. T. M. - E 399-70T point 7. 2. 3 (19). Measurements were made on several specimens and all fell within these limits, with the average of the trace readings being approximately 95% of their "average" crack length. The importance of this is that K is then fairly constant across the crack front since K is a function of the crack length.

5.2 Crack Length Versus Number of Cycles

Shown in Figure 10 is a plot of crack length, a, versus number of

cycles, N, for the four test temperatures of the specimens in the as received condition. Figure 11 shows the same plot for the heat treated specimens and those tested in a hydrogen atmosphere. These curves can be broken into three approximate regions; an initial zone of slow crack growth rate, a zone of increasing crack growth rate, and a slower final zone as the load decreases. The crack growth rates (da/dN) were obtained by measuring the instantaneous slope at each actual data point on the crack length versus number of cycles curves.

In constant deflection amplitude tests both the load and the stress intensity vary as the crack propagates thus one obtains a range of values for the crack propagation rates and the corresponding stressintensities from a single test. It is often practiced to approximate the curves of Figure 10 and 11 by a straight line and correlate this single crack propagation rate with an average stress intensity, so only one pair of data is obtained from a single test.

5.3 Crack Initiation

Crack initiation times were determined by observation with a 20 power travelling telescope. The time of crack initiation is taken as the number of cycles at which the crack first became visible. This was less than 0.0078 " (0.20 mm) of crack. For this reason all crack initiation times are relative to each other. Because of the method of defining crack initiation the relative initiation times are considered valid. True crack initiation occurred before this time, in

fact that there is a high probability that microcracks may be present before cycling begins. Because of the above fact normal statistics are not entirely valid. The crack initiation times are shown below and listed in Table VII.

INITIATION TIMES IN CYCLES (X1000)

Temperature °C	Environment	Cycles
-50	Argon	81.8 ± 9.8*
-10	Argon	58.7 ± 15.6*
21	Argon	34.0 ± 4.7*
71	Argon	50.0 ± 11.0*
-50	Hydrogen	86.0 ave. of 3 tests
-50	Argon (heat treated)	86.0 ave. of 3 tests
21	Hydrogen	40.0 ave. of 3 tests
21	Argon (heat treated)	40.0 ave. of 4 tests

* 90% confidence

A Rank test was used to determine whether the difference in the means of the crack initiation times as a function of temperature was significant. At the 95% confidence level it was found that the crack initiation times were significantly different for each of the temperatures except -10 °C and 71 °C.

The trends indicate that 21° C has the minimum crack initiation time and the value increases as the temperature is decreased or increased.

5.4 Crack Growth Rate Versus ΔK

Data on crack propagation rates as a function of stress intensity are commonly represented within a certain range of ΔK by the equation $da/dN = C \Delta K^m$. The stress intensity range, ΔK, is defined as K maximum minus Kminimum. To check this relationship and determine the constants C and m crack growth rates as calculated from the crack length versus number of cycle graphs were plotted on logarithmic paper against the stress intensity range, ΔK. Shown in Figures 12, 12A, 13 and 14 are the plots of da/dN versus ΔK for the 20 and 70°C tests, the -50 and -10 °C tests, the heat treated specimens, and for those tested in hydrogen respectively. The data is normalized with respect to the mean stress which varied from test to test. The manner in which this is accomplished is shown in Appendix 1.

The data points from each test specimen must be analysed separately because the density distribution of data points varies with ΔK from test to test. This would result in different weights of data points if data from all tests were combined for statistical analysis. In order to use these data properly each test must be individually statistically analysed to determine the relationship between da/dN and ΔK. Once this relationship for each test condition is determined the values of the two constants C and m can also be determined. The values of the constants C and m together with the correlation coefficients are

listed in Table VIII. The actual data points from each test are given in Table VI. The m value as a function of temperature is a maximum at -10° C and decreases as the temperature is increased or decreased. The values of C vary inversely to those of m. The m values for the heat treated specimens at -50 °C are high while those for the heat treated specimens at 21 °C are in line with the as received condition. The effect of hydrogen is difficult to analyse in that only the initial crack growth rates can be correlated with the stress intensities before unstable crack growth occurs. Because only a few data points are available the values of C and m cannot be used comparatively for the tests in hydrogen.

5. 5 Fatigue Life

The number of cycles to failure are listed in Table IX. The values given are the average number of cycles for the crack to grow three-quarters of the way across the net section. The material exhibited the longest fatigue life at -50 °C and the minimum at 21° C while the lives at -10 C and 71 °C were approximately the same. The effect of hydrogen was to decrease the fatigue life by increasing the crack propagation rate. Heat treatment had little effect on the material at 21 °C but increased crack growth at -50 °C thus decreasing the total fatigue life.

5.6 Hysteresis Loops

Load-deflection hysteresis loops were recorded during some of the tests. The area under these loops represents the mechanical energy dissipated in the specimen, the grips and connecting rod. To estimate the energy dissipated in the testing machine calibration tests were conducted using unnotched steel specimens. To calculate the energy dissipated in the notched fatigue specimens the area from the calibrated unnotched specimens was subtracted from the area recorded in the notched specimens. The calibration data indicated that approximately 80% of the total damping energy is dissipated in the fatigue testing machine and 20% of the absorbed energy is due to reversed plastic deformation. The data given in Appendix 2 will be used later to estimate the increase of temperature in the reversed plastic zone.

5.7 Cyclic Stress-Strain Curves

The results of cyclic stress-strain tests are given in Table IV. The stress versus the cumulative strain plot is shown in Figure 15. From the cyclic data it is observed that the order of the flow stress for a given strain is changed with respect to standard tensile test values. The flow stress for the 21 °C and 71 °C tests are now reversed in that the stress for a given strain is higher at 71 °C. These data will be used later in explaining some of the observations.

6. ANALYSIS AND DISCUSSION

In fatigue, cracks develop progressively from the submicroscopic phase of cyclic slip and crack initiation, through a macroscopic crack propagation period, to final fracture.

There are two basic approaches to the development of a mathematical expression which describes crack propagation, one approach is empirical and the other is mechanistic which relates to the structure and properties of the material. To date the most successful overall approach has been based on continuum mechanics. However, to develop materials with high resistance to fatigue crack propagation the metallurgist and materials engineer must combine continuum mechanics with the results of fatigue studies in a mechanistic approach to obtain an expression for crack propagation.

In recognition of this, the experimental results of this thesis will be analysed first on the basis of continuum mechanics and secondly on the basis of fatigue crack propagation mechanisms taking into account metallurgical and environmental factors.

6.1 Analysis Based on Fracture Mechanics

Crack growth studies have been directed towards establishing a relationship between the crack growth rate da/dN and the stress intensity factor, K, (15), (16), or between the crack growth rate, the crack length, a, and the stress, $\Delta\epsilon_g$, (17)(18)(19)(20)(21). The former relationship is represented by:

$$da/dN = C(\Delta K)^m \qquad (1)$$

and the latter relationship by:

$$da/dN = A(\Delta \sigma_g)^{m_1} a^b \qquad (2)$$

where $K = \alpha \sigma_g \sqrt{\pi a}$ (stress intensity factor for a tensile loading of a center notched specimen), α = finite width correction factor, $\Delta K = (K_{max} - K_{min})$, m, m_1 and b are invariant integers, a is the crack length, and C and A are related to material properties.

Frost and Dugdale (18), argued from experimental observations that $m_1 = 3$ and $b = 1$. Liu, (22) (23) used the saturation of absorbed hysteresis energy as a criterion for the onset of crack propagation and arrived at $m_1 = 2$ and $b = 1$.

A work rate model of crack propagation was used by Paris (16) to show that the crack propagation rate should be proportional to the stress intensity and after analysis of numerous experimental data arrived at $m = 4$.

Crooker (5) has shown that the entire fatigue crack growth rate curve for most materials is a sigmoid when plotted on logarithmic coordinates as shown in Figure 16. The power-law relationship which holds in the central portion of the curve is bounded by upper and lower inflection points. The lower inflection point is taken as an indication of non-propagating fatigue cracks. This range may extend down to exceedingly low stress intensity values where the crack propagation rates are of the magnitude of atomic spacing in the crystal lattice.

(10^{-7} - 10^{-8} in/cycle), (10^{-6} - 10^{-7} mm/cycle). The upper inflection point is caused by the onset of rapid unstable crack propagation prior to terminal fracture and thus places a critical range on the fatigue resistance of materials.

Thus all fatigue growth rates which lead to fatigue failure fall within a range of stress intensity factors, bounded at high values by Kc, the fracture toughness, and at low values by a threshold value, Kth. The value of K th is very sensitive to environment and may be shifted to lower values by an aggressive atmosphere.

Recently Donahue et al. (24) modified equation(1) to consider the threshold stress-intensity, Kth, below which no propagation occurs. The authors base their analysis on crack opening displacement which results in m = 2. Their equation is of the form:

$$da/dN = C(K^2 - Kth^2) \qquad (3)$$

In equation(1), m and C are considered separate and independent quantities which represent the crack growth rate dependence on the stress-intensity and on material properties respectively. In the above case m is an invariant integer and the materials influence on crack growth rate resides exclusively in C. The usefulness of such an equation for predicting crack growth rates for a given material is limited because C must be evaluated experimentally.

Originally the exponent m was thought to be invariant as 2 or 4. Crooker (5) has sampled a wide variety of data for steels which show

that the power value can vary between 1.5 and 10. However for most materials of structural significance the values range from approximately 2 to 5.

This shows that both m and C depend on material properties which must be determined by experiment. In the following it will be explored whether there is a relationship between these two values. For this purpose, data for m and ln C were taken from this study and the literature. The data is plotted in Figure 17. The m values range from 2 to 7 for a wide range of materials such as mild steels, high strengh steels, stainless steels, aluminum alloys, titanium alloys, copper alloys, and cobalt alloys. The data indicate a linear relationship between m and ln C of the form:

$$m_o - m = A \ln C \qquad (4)$$

The constant $m_o = -1.3569$ and the slope $A = -0.1024$ with a correlation coefficient of 0.993. Since the structure sensitive constant C is plotted in logarithmic form even small deviations can be significant. It is therefore proposed to modify equation(1)to read as follows:

$$da/dN = C\, Sc\, \Delta K^m \qquad (5)$$

In this form Sc is a structural factor which represents effects of metallurgical reactions and environmental effects. The value of m_o in equation(4)may vary slightly for each class of materials or condition of materials. Equation(5)can be linearized to the following:

$$\ln da/dN = (\ln C + \ln Sc) + m \ln \Delta K \qquad (6)$$

Thus the structural factor Sc would cause a parallel shift in the da/dN versus ΔK curves. To check this postulate, data from the literature were evaluated. The experimental data is given in Table X. The measured ln C values and the values as predicted from equation 4 are shown together with the error analysis.

Anctil and Kula (27) investigated the effect of temperature on the fatigue crack propagation rate in a 4340 steel at -50° F and 80° F. The specimens tested at -50 °F were tempered in the range from 400 °F to 800° F. Statistical evaluation of the data corresponding to equation 4 gave m_o =-1. 240 and A =-0. 102 with a correlation coefficient of 0. 998. Deviation from ln C ranged from -0. 293 to +0. 158 which correspond to errors ranging from -0. 66% to +0. 365%. The tests conducted at room temperature gave m_o =-1. 208 and A = -0. 1025 with a correlation coefficient of 0. 999. Deviation from ln C ranged from -0. 058 to +0. 0381 which correspond to errors ranging from -0. 173% to +0. 104%. If the test results from both temperatures are combined the values are m_o =-1. 212, A = -0. 101 and the correlation coefficient is 0. 999.

Further results on 4340 steel were obtained from data reported by Miller (26). The specimens were austenitized at 1500° F for a half hour then oil quenched and tempered. The tempering temperatures were 200, 500, 1000 and 1400 F. The data was evaluated statistically for the different tempering temperatures and the results are: m_o = -1. 364, A = -0. 1025 with a correlation coefficient of 0. 999. The errors

in ln C range from -0.847% to + 0.817%.

These results indicate that for the range of data investigated, tempering temperature and test temperature have little effect on the constant in equation 4, i.e. Sc = 1.

For Sc = 1, and a given m_o and A, there is a fixed relationship between ln da/dN and ln ΔK as shown in Figure 18. This relationship is found by solving equation (4) for C and substituting this value into equation (1) which results in:

$$\Delta K = (da/dN)^{1/m} \; e^{\frac{1 + m_o/m}{A}} \qquad (7)$$

From the above equation values of ΔK can be calculated for a constant crack growth rate and various values of m. Values of ΔK, and da/dN for constant m values can then be plotted. The relationship between ln da/dN, ln ΔK and m is expressed by a surface in the three dimensional plot shown in Figure 19. As noted from Figure 18 a common intersection point for all lines occurs. This intersection point is determined from the sets of data as follows:

$$da/dN = e^{\frac{m-m_o}{A}} (\Delta K)^m \qquad (8)$$

Consider a constant crack growth rate and:

$$e^{\frac{m_1 - m_o}{A}} (\Delta K)^{m1} = e^{\frac{m_2-m_o}{A}} (\Delta K)^{m2} \qquad (9)$$

All points intersect at a common value of ΔK_i, therefore:

$$e^{\frac{m_1 - m_o}{A} - \frac{m_2 - m_o}{A}} = \frac{(\Delta K_i)^{m2}}{(\Delta K_i)^{m1}} \qquad (10)$$

$$\frac{m_1 - m_2}{m_2 - m_1} \frac{1}{A}$$

or: $\Delta K_i = e$ (11)

and: $\Delta K_i = e^{-1/A}$ (12)

For all the data plotted in Figure 17 and using the value of A as determined, the value of ΔK at which all curves meet is 17300 psi $\sqrt{in.}$ The relationship below a ΔK of 17300 psi $\sqrt{in.}$ no longer holds as it now predicts that materials which would show slower crack growth rates for a given ΔK value now show higher crack growth rates for a given ΔK. In this form no differentiation is made from material to material as all intersect at one value of ΔK, thus indicating that all materials have the same stress sensitivity and a common crack growth rate for this value of ΔK_i. This is additional proof for the modification made to equation (1), since this change will cause the appropriate shifts in the da/dN versus ΔK curves which are necessary to fit observed data.

Test results of this research were also evaluated to determine the values of m_o and A. For this purpose reference is made to Figure 20 which shows the crack propagation rate as a function of the stress intensity range for the four test temperatures. From the plot one observes that the lines for -50 °C and -10 °C intersect at one point while those for 21 °C and 71 °C intersect at another. The point where the 21 °C and 71° C lines intersect is at a higher crack growth rate and lower ΔK value. Cyclic strain ageing should be negligible at the two lower temperatures as compared to the higher temperatures

thus one can postulate that the shift in the point of intersection is caused by strain ageing which takes place during fatigue cycling. The data for -50°C and -10°C was analysed giving m_o = -1.228 and A = -0.0986. The data for 21°C and 71°C gives m_o = -1.543 and A = -0.1029. What has happened, since both slopes (A) are practically the same is that a parallel shift in the curves has occurred. The two higher temperature values have moved above the two lower temperature values. The shift in the two parallel lines is expressed by the difference in the m_o values which corresponds to a difference in the ln C values. This gives Sc as in equation 5, a value of 1.545. This means that strain ageing increases the basic crack growth rate by 55%. As was previously mentioned, both C and m are affected by material properties, therefore superimposed to this is the effect of cyclic strain ageing on m, which is decreased, thus indicating a reduced sensitivity of the crack propagation rate to the magnitude of the stress intensity range.

6. 2 Analysis Based on Fatigue Mechanisms

Fatigue crack initiation and crack propagation is the result of localized reversed plastic deformation. In the case of polycrystalline metals, localized deformation can occur in grains which are favorably oriented with respect to the maximum shear stress, at stresses which are substantially lower than the conventionally defined yield strength of the bulk material. Since grains which are located at the surface are constrained less than those in the interior, yielding at lower stresses occurs and this explains why fatigue cracks normally initiate at the surface. Because these grains are also in contact with the environment, fatigue becomes a surface and environment sensitive failure mechanism. Superimposed to these aspects is the effect of stress concentrations which result in localized plastic strain concentrations. Stress concentrations may be caused by elastic crystalline anisotropy, surface roughness, inclusions, and differences in elastic and plastic properties of multiphase materials.

6. 3 Crack Nucleation

To precisely define what constitutes an initial fatigue crack is very difficult. Microscopic observations of the surface of specimens undergoing cyclic loading indicate that slip bands and microcracks form very early in the cyclic life, however the scale of this deformation is below the range that can be detected by conventional inspection equipment. Therefore the definition for an "engineering size

'crack" is appropriately adopted. Manson and Hirschberg (27) adopted a crack length of 0.003 in (0.076 mm) which can be detected with a low power microscope as the criterion for crack initiation. In this thesis an average crack length of 0.0078 in (0.20 mm) was adopted as a crack initiation criterion.

As well, several dislocation models have been developed to describe the nucleation of fatigue cracks. Almost all of these models rely on the onset and localization of plastic deformation by slip leading to notching of the metal surface. Therefore, the discussion will be based on this "descriptive" model rather than the dislocation models.

In single crystals of favorable orientation, cyclic loading will cause the formation of uniform fine slip bands on the surface and appreciable cyclic strain hardening occurs after only a few cycles. The matrix structure associated with this hardening consists of dislocation debris. After less than 1% of the total life slip begins to concentrate in "persistent slip bands" in which cracks eventually nucleate. Persistent slip band formation is commonly observed in polycrystalline materials as well. The dislocation structure in these bands is a cell structure which is characteristic of a high amplitude fatigue-matrix structure. Flow stress, hardness and hysteresis loop measurements indicate that the persistent slip bands are "softer" than the surrounding material, which means they have both a lower flow

stress and a lower strain hardening rate. The strain amplitude, temperature, and slip character influence the slip distribution and crack nucleation characteristics. As an example, if the stress amplitude is increased the entire specimen surface can be covered with persistent slip bands with a tendency in polycrystalline material for intergranular rather than transgranular crack initiation. The behaviour of persistent slip bands in commercial alloys undergoing low-amplitude fatigue must be similar to the bulk material undergoing large cyclic strains, therefore, the cyclic stress-strains response of alloys undergoing large cyclic strains can be assumed to be representative of what occurs locally at smaller strains and longer lives.

The effect of grain size on fatigue crack initiation has been studied by several authors (28). Generally an increase in grain size results in a reduction of crack initiation life. When slip bands produced by high amplitudes impinge on a grain boundary it causes an offset strain in the boundary which results in a high stress across the boundary. As cycling continues the offset and the stress increase until a crack initiates. The effect of grain size can be illustrated by assuming the same cumulative strain in two grains of different size. For this case the plastic strain increment per cycle $\Delta \varepsilon p = \Delta \ell / \ell$ is the same in each grain, however on this scale ℓ is proportional to the grain size, hence the displacement (offset) $\Delta \ell$ and the resulting

stress will be larger in the larger grain which causes shorter crack initiation periods. Large differences in grain size are required to have a significant effect on fatigue crack initiation times. The increase in grain size from the heat treatment given the test specimens in this thesis was 17. 5% and as a result no significant difference in crack initiation times were observed.

In steels strain ageing may also affect fatigue crack initiation. Strain ageing may be defined as the time dependent property changes which occur following plastic deformation. Ageing effects in steels result from the interaction of point defects, i. e. interstitial atoms such as nitrogen or carbon with dislocations. The rate of change of any property depends on the amount and method of deformation, temperature, time and the solute atom concentration. The interaction effects inhibit plastic flow (29). In the mortal life range, mild steels which exhibit distinct yield points undergo a "softening" at low strain amplitudes and a hardening at higher amplitudes. At low strain amplitudes softening occurs first then hardening occurs (30). The dislocation locking is broken down during cycling and the pronounced yield point disappears. Strain ageing during fatigue (dynamic strain ageing) depends on many variables and is rather complex. Dynamic strain ageing is both a cycle and time dependent phenomenon (31) (32). In addition it is also very sensitive to temperature. Calculations of the diffusion coefficient and the mean time of stay for an atom in an

interstitial position are given in Table XI. As the temperature increases from 21 to 71 °C a factor of 100 difference occurs in both the above properties. One point that is commonly neglected is the increase in temperature that occurs in the slip bands. If one considers that almost 95% of the work of deformation is converted to heat substantial temperature increases can occur in the slip bands. This may significantly modify the ageing kinetics above and beyond overall temperature increase effects. Measurements performed in this research were used to estimate the temperature increase. The maximum temperatures in the reversed plastic zone were calculated by two methods and both gave approximately the same temperature values. A description of the methods and the calculations are shown in Appendices 2 and 3. Temperature increases of at least 100 °C occur, and it is considered that these values are conservative in nature. The increased temperature effects can also be very important when analysing environmental effects as will be discussed later.

The observed effects of environments on fatigue crack initiation are contradictory. Broom and Nicholson concluded that crack initiation was affected by environment while Brashaw and Wheeler concluded that the major effect was on the rate of crack propagation (33).

In summary previous studies have shown that fatigue crack nucleation depends on such properties as flow stress and strain hardening and is influenced by grain size, strain ageing and possibly

environment.

The results of this research will now be analysed.

In the test temperature range used in this investigation, a wide variety of material properties occurred. Temperature dependent ageing reactions are superimposed on the effects which temperature has on the material properties, therefore it is necessary to discuss these aspects before analysing other possible factors.

The sensitivity of this steel to strain ageing has been explored. Figure 21 shows an increase in the yield strength and hardness during ageing at room temperature following plastic deformation. The upper yield strength increased by 23% in 100 hours while the Rockwell D hardness increased by 23% in 20 hours. These ageing times compare with an average time of 1 hour for crack initiation and 6 hours for total fatigue life. It should be kept in mind that localized heating can substantially increase the rate of ageing. At higher temperatures strain ageing can be so rapid that it occurs during straining leading to the well known blue brittleness.

To study the effects of temperature and ageing time tensile tests were performed in the temperature range -50°C to 260°C at strain rates of 0.2 in/in/min and 0.002 in/in/min. Shown in Figure 22 is a plot of yield strength and ultimate tensile strength at the two strain rates as a function of temperature. Also shown in Figure 23 is a plot of fatigue life, crack initiation, and crack propagation time as a function

temperature. The ultimate tensile strength exhibits the commonly observed trend with increasing temperatures; a monotonous decrease with a minimum at approximately 100° C followed by an increase in the blue brittle range. Because simultaneous or prior deformation is necessary for the ageing reaction to occur the yield strength also decreases as the temperatures increase. The values of yield stress increase as the temperature decreases below 21 °C. At the lower strain rates, the stress values are lower but exhibit the same trends indicating the material is strain rate sensitive. Although the bulk yield strength and tensile strength may indicate a trend similar to crack initiation times with respect to temperature these properties may not be as significant as the flow stress since fatigue is caused by reversed plastic deformation.

Flow stresses at different strains are plotted as a function of temperature in Figure 24. The flow stresses show additional characteristics which are different from those of yield strength and ultimate tensile strength.

At the high strain rate the flow stress reaches a minimum value at about 80 °C and a maximum in the blue brittle range at about 190 °C, indicating a lowering of these critical temperatures. Strain rate has a significant effect particularly at -50° C and -10 °C. At these two temperatures the flow stress at the low strain rate is substantially lower than the flow stresses at the higher strain rate. The low-rate

flow stresses increase, at about 20 °C after which they follow parallel to the high strain rate values. This type of behaviour indicates certain ageing reactions are occurring while straining in the 0° C to 20 °C temperature region. This means that two ageing reactions take place, one which appears at 180 °C and the other at about 20 °C. It is well established that the increase in the blue brittle range is caused by interactions of interstitial carbon with dislocations. Nitrogen has a higher diffusivity (see Table XI) than carbon which may cause a similar increase of the flow stress at 20 °C and the low strain rate. It is believed that nitrogen has the greatest effect on the strain ageing process (38) and coupled with the much greater solubility (approx. 100 times) (35) this lower temperature low strain rate effect is plausible. Data from Pugh et al. (36) may partially substantiate this observation. Tensile tests on high purity iron (C 0.0034%, N0.001%) were performed at two strain rates as a function of temperature. A decrease in engineering fracture stress and tensile strength occurred at the low strain rate below room temperature. Although detected in the course of this work a detailed analysis of this aspect is beyond the scope of this thesis.

Referring to Figure 23 which shows fatigue crack initiation life, and total life as a function of temperature, a minimum in fatigue crack initiation life occurs at 21 °C. This decrease may be due to the decrease in yield strength or flow stress, but the further increase with increasing temperature is most likely due to cyclic strain ageing.

This is evident from the cyclic yield stress data shown in Figure 25. The cyclic yield stress as a function of temperature indicates a trend similar to crack initiation time and total life which is shown in Figure 23. A minimum occurs in the cyclic yield stress at 21 °C. The cyclic flow stress, however, does not exhibit a pronounced minimum. The increase in the cyclic yield strength above 21 °C could result from the increased rate of strain ageing.

A comparison of fatigue crack initiation life with other parameters such as strain hardening exponent, grain size, temperature and environment is given on the following page and is also shown in Table XII.

From this table it appears as though the greatest effect on crack initiation time is the test temperature. The environment and grain size do not have any significant effect on crack initiation time and no apparent correlation is observed between the static, cumulative cyclic, or non-cumulative cyclic strain hardening coefficients. It is interesting to observe that the strain hardening exponent, n, from the static tensile tests all show a slightly higher value at the lower strain rate which indicates that ageing is occurring during the test duration.

COMPARISON OF CRACK INITIATION TIME WITH VARIOUS MATERIAL PROPERTIES

Environment	Grain Size (mm)		Temperature °C	Crack Initiation $\times 10^3$	Static n	Cyclic Cumulative n^1	Cyclic non-cumulative n^{11}	m
Argon	0.022	a	- 50	82.0	0.202 *	0.259	0.223	4.495
	0.033	b			0.213 **			
Argon	0.022	a	- 10	59.0	0.216 *	0.175	0.075	6.81
	0.033	b			0.223 **			
Argon	0.022	a	21	34.0	0.209 *	0.186	0.105	5.195
	0.033	b			0.214 **			
Argon	0.022	a	71	50.0	0.193 *	0.212	0.102	2.66
	0.033	b			0.210 **			
Hydrogen	0.022	a	- 50	86.0				
	0.033	b						
Hydrogen	0.022	a	21	40.0				
	0.033	b						
Argon	0.026	a	- 50	86.0				
heat-treated	0.042	b						
Argon	0.026	a	21	40.0				
heat-treated	0.042	b						

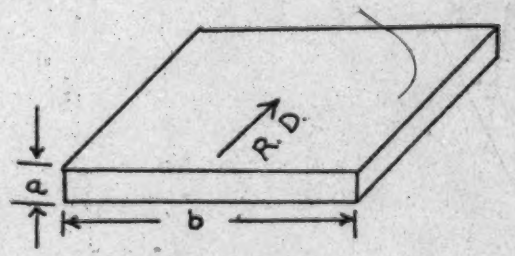

Strain rate 0.2 in/in/min = 0.2 mm/mm/min*
0.002 in/in/min = 0.002 mm/mm/min**

6.4 Fatigue Crack Propagation

Generally fatigue crack propagation is divided into two stages, called Stage I and Stage II. Fatigue cracks form as slip band cracks, (usually crystallographic unless very high amplitudes are used), in the manner discussed in the previous section. Stage I propagation is favored under conditions of low stresses or corrosion fatigue below the air fatigue limit (37). During crack propagation in Stage I slip band cracks continue to grow along planes of maximum shear stress. In polycrystalline materials, Stage I involves many individual slip band cracks which eventually link up. At this point the Stage II propagation begins during which the cracks grow along planes of maximum tensile stress (generally non - crystallographic) until it reaches a critical crack length for which the next load peak produces a tensile failure of the specimen. The fraction of the total fatigue life spent in Stage II crack propagation increases with increasing load amplitude.

It is commonly accepted that strain hardening associated with localized plastic deformation are the dominant factors which control the rate of fatigue crack propagation (38). Laird (38) has proposed a plastic blunting model of fatigue crack propagation which is supported by many observations. This model is schematically illustrated in Figure 26. During the tensile part of the load cycle high localized plastic strains occur at the crack tip. These cause a blunting of the

crack tip and strain hardening in this region. Upon reversal the crack faces are forced together without complete reversal of the load. This causes the crack to advance by an amount which is proportional to the difference of the new surface formed by the extension in the tensile stroke and that regained in the compression part of the cycle. The full compression resharpens the crack and prepares it for the next tensile cycle. This "plastic blunting" process results in the ripples or striations often observed on fatigue fracture surfaces.

Such striations were observed in scanning electron fractographs and transmission electron fractographs as shown in Figure 27. It is generally agreed that each striation corresponds to one cycle of crack growth, thus localized crack growth rates can be calculated by measuring the distance between striations. Measurement of the striation spacing on several electron micrographs gave a crack propagation rate of 10^{-6} in/cycle which agrees very well with the macroscopically measured values. Figure 28 also shows that striations occur in isolated patches while the rest of the fracture surface contains dimples and irregular markings.

The plastic deformation at the crack tip is localized within a small zone which is embedded in an elastic region. On increasing the load amplitude the size of the plastic zone increases as well as the crack propagation rate. Crack propagation models based on fracture mechanics attempt to relate the crack propagation rate to the plastic zone size by

elastic-plastic analysis, however, there is a distinct difference in the plastic zone size caused by unidirectional loading and that caused by fatigue loading.

When a specimen containing a crack is subjected to zero-to-tension loading the plastic zone at the crack tip is subjected to constant strain amplitude cycling. Under these conditions the tensile mean stress present in the plastic zone on the first cycle gradually relaxes to zero during subsequent cycling. This is illustrated in Figure 29. Therefore after several cycles the plastic zone is subject to reversed stressing rather than zero-to-tension loading. Consequently a large zone forms on the first cycle and decreases on subsequent cycling to the "reversed plastic zone". Rice (39) calculated a four fold reduction in the size of the plastic zone for an ideal elastic-plastic material, but this analysis disregards changes due to strain hardening and strain ageing. The sequence of events is illustrated in Figure 30. On the first tensile stroke a large plastic zone is formed due to the high strain and stress concentration resulting from the sharp crack. If crack tip blunting is neglected, the stress concentration factor is effectively infinite and reversed plastic flow commences with the first increment of load reduction, creating a new plastic zone which is embedded in the original zone caused by the first tensile loading.

This initial or "monotonic plastic zone" is larger at the surface because of plane stress conditions than in the interior of the crack front where plane strain conditions exist. An illustration due to Liu (21) is shown in Figure 31. The size of the plastic zone is also affected by strain hardening or softening, strain ageing, temperature, and the environment. For example, in steels which exhibit pronounced yielding plastic deformation initiates by formation of Luders bands. Figure 32 shows a photograph of the surface plastic zone in a steel specimen from this series. One observes the propagation of Luders bands at the elastic-plastic boundary. Furthermore propagation of the plastic zone occurs in increments as indicated by the sequence of curved bands along the crack boundary. Figure 33 shows the surface plastic zones for the four test temperatures. Shown in Figure 34 are the reversed plastic zones as revealed by etching which indicates the dense substructure within the plastic zone. A large difference between the 21°C argon environment and the 21 °C hydrogen environment is evident. The data for the four temperatures is plotted in Figure 35. The size and shape of the reversed plastic zone were measured and the data is listed as follows and given in Table XIII.

SIZE OF PLASTIC ZONES IN STEEL SPECIMENS

Environment	Temperature °C	Radius of Plastic Zone, in, (mm) reversed r_r	surface r_s	r_s / r_r
Argon	-50	4.5×10^{-4} (0.0114)	0.0251 (0.636)	56
	-10	7.0×10^{-4} (0.0178)	0.0270 (0.685)	38
	21	2.0×10^{-3} (0.0510)	0.0368 (0.990)	18
	71	1.0×10^{-3} (0.0259)	0.0490 (1.24)	49
Hydrogen	-50	not detectable	0.0335 (0.85)	
	21	" "	0.049 (1.24)	

Both the surface plastic zone and the reversed plastic zone increase with increasing temperature except in the temperature range where strain ageing is significant, i. e. at 71° C, and here the reversed plastic zone decreased in size. The surface plastic zone is not affected by strain-ageing which is plausible since it forms on the first tensile stroke where strain-ageing is not a factor. The surface zone is actually larger here and this can be related to the decreased yield strength at 71 °C. The effect of strain-ageing on fatigue has been studied by several investigators (32) (40) (41) (42) (31) (29) (43). No complete agreement between the investigations has been reached and this can be well appreciated as dynamic strain-ageing is a complex problem related to many variables. However, Wilson (29), 1970, has concluded that strain-ageing does contribute to fatigue strengthening "at around room temperature" by limiting the spread of fatigue damage.

This result tends to correlate with the reversed plastic zone sizes, as the size at 71 °C where strain ageing is significant, is reduced.

A comparison was made between the plastic zone sizes, crack initiation life, and total fatigue life. No consistant correlation could be found between the surface zone size and the fatigue life. This was also observed by Weiss and Meyerson (44) who made measurements of the surface plastic zone. The inverse of reversed plastic zone size, total fatigue life and crack initiation time are plotted in a relative manner as a function of temperature in Figure 36. It is evident from this figure that fatigue life and crack initiation life correlate with the reversed plastic zone size, i. e., as the zone size increases fatigue life decreases. This can be further expanded to include an observation made by Irwin (45) that the size of the localized plastic zone at the tip of a crack is proportional to the stress intensity, to yield strength ratio squared. Tables III and IV give the static and cyclic tensile test data. From the static tensile data it can be observed that for a common stress intensity the surface plastic zone size should decrease as the temperature is decreased below 21 °C, since the yield strength increases. However, above 21 °C the yield strength decreases which would indicate a larger surface plastic zone. The static tensile data correlate with the Irwin relationship in that the surface plastic zone follows the correct trend with respect to yield strength. As previously mentioned the surface plastic

zones sizes do not correlate with the observed fatigue life. Therefore, it can be concluded that the static tensile data are not sufficient to explain the results. If the cyclic yield stress values are used in the relationship due to Irwin, the trend that the largest reversed plastic zone size occurs at 21 °C for a given stress intensity is observed. It follows from this that as the stress intensity increases the crack growth rate increases as does the reversed plastic zone size. Another interesting point is indicated in Figure 15 which shows the static and cyclic stress-strain curves. The order of the curves with respect to temperature is modified in that the flow curve for 71 °C is above that at 21 °C for the cyclic data. This falls in line with the observed trend in fatigue life which can be correlated with the amount of plasticity. This means that for a given stress the amount of strain at 71 °C is less than that at 21 °C.

The results of the above discussion definitely indicate that the use of cyclic data and reversed plastic zone sizes are much better suited to predicting observed fatigue behaviour than static tensile data and surface plastic zone sizes.

It is interesting to note that hydrogen increases the surface plastic zone size but decreases the reversed plastic zone sizes to values which are below detectability. This indicates the strong interaction of hydrogen with the reversed plastic strain which results in the brittle nature of crack propagation in hydrogen. This is also visible from the

scanning electron micrographs shown in Figure 37. In hydrogen fatigue striations are absent which indicates a low level of plastic deformation. There have been at least 3000 papers (48) concerned with the effect of hydrogen in metals which have resulted in three proposed basic interactions between hydrogen and metals; however, most of these papers have dealt with the effect of hydrogen under static loading conditions or as in the case of dynamic loading, the effect of hydrogen on high strength alloys.

Elsea and Fletcher (47) have observed under static loading that crack propagation is a discontinuous series of crack initiations and propagations. Williams, (48) found no temperature dependence on crack growth rate between -10 and 59 °C for a 4130 steel in the presence of hydrogen. Bernstein (46), in a review, states that hydrogen can cause embrittlement between -100 and +100°C with the most severe effect around room temperature. Vitovec (49) has found the plastic deformation in the presence of hydrogen accelerates attack. In creep tests the reduction in area and rupture times were also reduced. Jackson (50) has also found that straining in the presence of hydrogen can reduce the breaking stress of steel. It has also been found that tensile stresses across iron and steel membranes significantly increase the solubility of hydrogen in these membranes (51).

Just recently Beachem (51), 1972, has proposed a new model for hydrogen assisted cracking. The model suggests that the presence of

sufficiently concentrated hydrogen dissolved in the lattice just ahead of the crack tip aids whatever deformation processes the microstructure will allow. This new model does not support the embrittlement theories in that it predicts hydrogen unlocks dislocations thus allowing them to move or multiply at reduced stresses rather than lock them in place. The model also proposes that the fracture modes are dependent on the chemistry of the steel, the heat treatment, the microstructure, the crack tip stress intensity factor, and the rate of supply of hydrogen to the crack tip which determines the concentration there.

With this background the test results will now be discussed. The crack length, a, versus number of cycles graphs are shown in Figure 11. The ΔK versus da/dN curves for the specimens tested in hydrogen are shown in Figure 14. As can be observed the fatigue lives are considerably shorter at both -50°C and 21°C in the presence of hydrogen. The crack growth rate increased by an order of magnitude under these conditions.

The test results indicate that an incubation period is required, either for the hydrogen to attain some critical concentration within the material or for the stress to reach some critical value (46) (52). The result of a 21°C test which was begun in argon then changed to hydrogen indicate that the presence of a sharp crack, i. e. higher stress or strain, reduce the incubation time required, as unstable crack propagation began very soon after the change. A photograph of this particular

test is shown in Figure 38. The surface plastic zone is almost non-existant at the start where argon was used but becomes evident when the hydrogen is introduced and rapid crack growth begins. A critical stress intensity factor range (ΔK_{IC}) of 20 - 22 ksi$\sqrt{in}$ is necessary for the onset of rapid propagation. This stress intensity range under the the other test conditions did not cause rapid crack growth.

Reference will now be made to the Table of reversed plastic zone sizes and surface plastic zone sizes. These are also illustrated in Figures 33 and 34. These figures and tables indicated that hydrogen increases the surface zone size but substantially decrease the reversed plastic zone size and the amount of fracture surface deformation. The surface zone size increase tends to agree with Beachem's new model as this zone is formed on the first tensile stroke which simulates the semi-static wedge loaded tests used in his report. This increase in surface plastic deformation may result from hydrogen reducing surface layers which inhibit dislocation motion. The decrease in plasticity as observed on the fracture surfaces and from reversed plastic zone measurements do not agree with Beachem's model. Under dynamic loading there are several conditions which would make a bad situation worse. These are: the presence of hydrogen while plastic deformation is occurring, the formation of a large plastic surface zone which provides a greater surface area for hydrogen to diffuse through, and a

very important consideration which is the local temperature rise due to cycling which can accelerate the diffusion of hydrogen into the matrix ahead of the crack.

6. 5 Analysis of the Tomkins Model

The fundamental problem in developing crack propagation theories is the determination of the displacements in the vicinity of the crack tip and relating these to the nominal stress or strain by a realistic stress-strain law. This problem has been approached in several different ways. These include the Bilby-Cottrell-Swinden (53) theory of continuously distributed dislocations, elastic-plastic analysis, and elastic-plastic measurements. Many of these theories give basic crack growth laws of the form $da/dN = C\ \Delta K^m$ which is identical to equation(1). In these laws m is a constant, not borne out by experiment and C is the only parameter which depends on material properties. From this point of view Tomkins (54) proposed a model which comes closest to reality. He used the Bilby-Swinden analysis, a power hardening law, and a plastic decohesion crack advance criterion (55). The power value m is a function of the cyclic strain hardening behaviour. For these reasons the Tomkins model will be used to analyse the data of this research. It is therefore expedient to review Tomkins analysis before using his equation to evaluate the experimental data.

The model is derived for a ductile metal under tension-compression loading. A schematic diagram of the crack tip configuration is shown in Figure 39. It was noted in some photographs (Figure 40), that slip bands of this nature were present.

During the tensile half of the cycle plastic flow occurs on two narrow bands at $\mp 45^{o}$ to the crack tip. On increasing the strain to the tensile strain limit a new surface is formed by shear decohesion along the inner edges of the flow bands where the shear strain gradient is a maximum. The theory assumes that on the closing half of the cycle, the shear flow is reversed without significant re-cohesion. It appears as though this assumption is justified (33).

The Dugdale (55) model of plastic cohesive forces is applied to the fatigue problem since the shear strain is concentrated in a narrow band. The plastic zones are replaced by distributions of plastic shear stress, S, acting on the $\mp 45^{o}$ lines, of length D. For the plane strain case the exact form of S is not known, but it is assumed that it should be above the maximum nominal shear stress of material near the tip and approximately at the flow stress at the other end of the zone of length D. The equilibrium stress condition is given by Bilby and Swinden (53), from an analysis using linear dislocation arrays to represent a crack. The crack is represented by a continuous distribution of edge dislocations with their Burgers vectors perpendicular to the crack plane.

The dislocations in the regions of plastic relaxation are assumed to experience a shear resistance acting along the slip lines and to be edge dislocations with their Burgers vector making an angle $\pm\Theta$ with the crack. The equilibrium stress condition is given by:

$$D/a = \sqrt{2}\left[\sec(\pi\sigma/2S2) - 1\right] \qquad (12)$$

Equation(12) gives the ratio of plastic shear band length, D, to crack length, a, for a given applied stress, σ, and plastic shear stress. Experimental results indicate that S can be approximated by $\bar{S}$, an average stress acting over the length, D, and equation(12) becomes:

$$D/a = \sec(\pi\sigma/2\bar{S}2) - 1 \qquad (13)$$

Equation(13) is of the form:

$$A = \sec x - 1 \qquad (14)$$

If the $\sigma/2\bar{S}$ ratio is small then equation(14) can be expanded by the power series for sec x and the result is:

$$D/a = \pi^2/8(\sigma/2\bar{S})^2\left[1 + \pi^2/8(\sigma/2\bar{S})^2\right] \qquad (15)$$

Equation(15) is approximated once more in that the second term is multiplied by 1/32 whereas the value from the secant expansion is 5/192. Due to the nature of the secant expansion only the first two terms are significant. Up to this point the deformation zone size D, as a function of the crack length and stress is approximately known. A relationship between the amount of de-cohesion δ, and the deformation zone size is necessary. At the crack tip where the applied strain exceeds the fracture strain de-cohesion begins, implying that increased plastic strain is

accomodated by the formation of a new crack surface. The amount of new crack surface is given by:

$$\delta = f \varepsilon_p D \qquad (16)$$

where δ is the crack growth increment per cycle. The f is a geometric factor which is approximately 1.5 but due to the effect of the free surface reducing the transverse strain in the crack tip region is assumed to be closer to 1, therefore:

$$\delta = \varepsilon_p D \qquad (17)$$

Equation(17) is found to be generally true from experimental results. This is partially substantiated by Figure 36 which shows the size of the reversed plastic zone and fatigue life plotted versus the temperature. As the zone size increases the fatigue life decreases which is what equation(17) predicts.

The cyclic stress-strain curve of a material can be represented by the following relationship:

$$\Delta \sigma = B(\Delta \varepsilon_p)^{n'} \qquad (18)$$

Since crack growth occurs in the tensile half of the cycle $\sigma = \Delta\sigma/2$, this is substituted into equation(15) which gives:

$$D/a = \pi^2/32\,(\Delta\sigma/2\bar{S})^2 \left[1 + \pi^2/32\,(\Delta\sigma/2\bar{S})^2\right] \qquad (19)$$

The assumption that the crack extension per cycle is $\Delta\varepsilon_p D$ is now used. As the crack grows, the crack length, a, increases and by combining equation(17) and(19) the crack growth rate per cycle is:

$$da/dN = \Delta\varepsilon_p D = \pi^2 \Delta\varepsilon_p (\Delta\sigma)^2\, a/32(2\bar{S})^2 \left[1 + \pi^2/32\,(\Delta\sigma/2\bar{S})^2\right] \qquad (20)$$

The value of $2\bar{S}$ is replaced by an equivalent tensile stress T. substitution of equation(18) into equation(20) gives:

$$da/dN = \pi^2/8\,(B/2T)^2\left(1+\pi^2/8\,(B/2T)^2\Delta\epsilon_p{}^{2n^1}\right)\Delta\epsilon_p{}^{2n^1+1}\,.\,a \qquad (21)$$

Unless very high strain fatigue is considered $\Delta\sigma/2T \ll 1$ and equation (21) becomes

$$da/dN = \pi^2/8\,(B/2T)^2\,\Delta\epsilon_p{}^{2n^1+1}\,.\,a \qquad (22)$$

Equation(22) can also be expressed in terms of the stress range as well by substituting $\Delta\epsilon_p = (\Delta\sigma/B)^{1/n^1}$. This results in:

$$da/dN = \pi^2\,\Delta\sigma^{2n^1+1/n^1}\,.\,a/8\;B^{1/n^1}\,(2T)^2 \qquad (23)$$

A comparison of equation(23) and equation(1) using test data of this investigation will be made in the following section.

For comparison equation(23) may be rewritten to compare with equation(1):

$$da/dN = C^1\,\Delta\sigma^{m_t}\,a \qquad (24)$$

where $m_t = (2n^1+1)\,/\,n^1$ and (24a)

$$C^1 = \pi^2/8\;B^{1/n^1}\,(2T)^2 \qquad (24b)$$

For comparison equation(1) reads:

$$da/dN = C\,(\Delta K)^m$$

where C and m are experimentally determined. The stress intensity for notched bending tests used in this research is given by:

$$K = \Delta\sigma\left[1/(1-a/h)^3 \;-\; (1-a/h)^3\right]^{1/2} \qquad (25)$$

where h is the depth of the specimen. For the purpose of comparing results a crack length of a = 0.2 inches and a stress of 13670 psi is

assumed. This gives a stress intensity range of 20,000 psi$\sqrt{in.}$ To evaluate the Tomkins equation the cyclic strain hardening exponent n^1 as calculated from the total accumulated strain, and n^{11} as calculated from the strain amplitude of each cycle were used. The data is listed below and is also given in Table XIV.

Crack Propagation Rate (in / cycle)

Test Temperature °C	Experimental	Tomkins	
		n^1	n^{11}
-50	7.85×10^{-7}	7.02×10^{-6}	2.65×10^{-7}
-10	1.90×10^{-6}	1.14×10^{-6}	1.90×10^{-11}
21	3.13×10^{-6}	4.36×10^{-6}	1.41×10^{-9}
71	1.67×10^{-6}	5.02×10^{-6}	1.59×10^{-9}

The Tomkins equation gives crack propagation rates which are reasonably close to the experimentally determined ones, provided that cyclic stress-strain data based on accumulated strain are used. The trend observed with temperature is not well represented by Tomkins analysis but this is not surprising when considering the approximations made in the derivation. Furthermore, strain cycling experiments may not fully represent the cyclic strain ageing effects of a small plastic zone at the tip of a crack. In a further comparison the exponent m from equation(1)and the exponent m_t from equation(24a) were plotted as a function of temperature. These are shown in Figure 41. The curves show that m_t calculated from the cumulative strain hardening exponent n^1 is somewhat larger than the experimental value but the trend

with temperature compares favorably. Strain hardening exponents calculated from the strain amplitude show no correlation.

A further check of the Tomkins equation was made by checking the relation between ln C^1 and m_t according to equation (4). These are plotted in Figure 42. One observes that the values calculated from the Tomkins equation fall slightly above the experimental values but the trend is the same and linear relationship holds.

with temperature compares favorably. Strain hardening exponents calculated from the strain amplitude show no correlation.

A further check of the Tomkins equation was made by checking the relation between ln C^1 and m_t according to equation (4). These are plotted in Figure 42. One observes that the values calculated from the Tomkins equation fall slightly above the experimental values but the trend is the same and linear relationship holds.

SUMMARY AND CONCLUSIONS

The main results of this investigation which pertains to cyclic bending fatigue tests in environments of argon and hydrogen in the temperature range from -50 to 71° C are summarized as follows:

1. Fatigue crack initiation life and total fatigue life in argon decrease with increasing temperature until a minimum is reached at room temperature from which they increase as strain ageing becomes significant at higher temperatures.
2. Crack initiation times are not affected by hydrogen.
3. The monotonic plastic zone at the surface is very much larger than the reversed plastic zone.
4. Hydrogen increases the size of the monotonic surface plastic zone, but decreases the reversed plastic zone to values which are below the range of microscopic observation. This concurs with the brittle crack propagation mode observed by scanning electron microscopy.
5. Within a certain range of stress intensities, the crack propagation rate can be expressed by the equation, $da/dN = C(\Delta K)^m$. The power value m represents the sensitivity of the crack propagation rate to the stress intensity range.
6. A decrease in the test temperature causes a decrease of the crack propagation rate and a decrease of the sensitivity to the stress intensity range.

7. Cyclic strain ageing causes a decrease in the crack propagation rate at 71 °C compared with that of 21° C and a decrease in the sensitivity of the crack growth rate to the stress intensity range.

8. There is a relationship between ln C and m of the form $m_o - m = A \ln C$ which is the same for a material in different heat treated conditions and at different test temperatures provided no strain ageing occurs during cycling.

9. Tomkins model for fatigue crack propagation can reasonably well represent experimental results but refinements of the mathematical analysis are possible and necessary.

10. A more detailed study into the effects of localized heating in the crack tip area is required so that one can better understand the tip conditions for crack growth analysis.

11. Crack initiation life, total life, and crack propagation life are proportional to the inverse of the reversed plastic zone size.

12. Mean stress has a significant effect on fatigue crack propagation rates within a certain stress range.

TABLES

TABLE I

CHEMICAL COMPOSITION OF THE TEST MATERIAL

ELEMENT	WEIGHT %
Carbon	0.2
Manganese	0.82
Niobium	0.012
Phosphorous	0.006
Sulphur	0.021
Tin	0.05*
Nickel	0.05*
Chromium	0.05*
Molybdenum	0.05*
Copper	0.05*
Vanadium	0.005*

GIVEN MATERIAL PROPERTIES 20 °C

PROPERTY	VALUE	Mega N/m^2
Yield Stress	48,000 psi	331.2
Tensile Strength	65,000 psi	448.4
Fracture Strain	.265 in/in at .010 in/min	
Reduction of Area	33%	

* Less than.

TABLE II

CHARPY IMPACT TESTS

All values given are the average of two tests.

Set #1 - Condition of material: 954°C full anneal
Orientation: Parallel to the rolling direction.

Temperature °C	Energy Foot-pounds	Joules
70	73.0	99.0
22	55.0	74.5
0	10.0	13.55
-10	8.8	11.90
-25	6.5	8.8
-50	4.0	5.42

Set #2 - Condition of material: as received
Orientation: Perpendicular to the rolling direction.

Temperature °C	Energy Foot-pounds	Joules
70	55	74.5
22	35	47.5
0	25	33.9
-25	20	27.1
-50	23	31.2
-70	18	24.4

Set #3 - Condition of material: as received
Orientation: Parallel to rolling direction.

Temperature °C	Energy Foot-pounds	Joules
70	47.0	63.7
22	30.0	40.7
0	8.5	11.5
-25	8.0	10.85
-50	6.0	8.12

TABLE III

STATIC TENSILE TEST DATA AS A FUNCTION OF STRAIN RATE AND TEMPERATURE

TEMPERATURE °C and Strain Rate in/in/min(mm/mm/min)	n*	Yield Stress psi(mega N/m^2)	U. T. S. (eng) psi (mega N/m^2)	Fracture Strain $\ln l_f/l_o$	U. T. S. $P\,l_f/Al_o$ psi (mega N/m^2)	Fracture Strain $\ln A_o/A_f$
- 50						
0.2	0.202	6.6×10^4(455)	7.56×10^4(521)	0.279	9.32×10^4(642)	0.942
0.002	0.213	6.0×10^4(412)	7.13×10^4(491)	0.286	8.68×10^4(598)	0.820
- 10						
0.2	0.216	5.89×10^4(406)	7.34×10^4(501)	0.203	8.60×10^4(593)	0.956
0.002	0.223	5.12×10^4(353)	6.60×10^4(455)	0.266	8.00×10^4(550)	0.836
21						
0.2	0.209	5.51×10^4(380)	6.92×10^4(477)	0.233	8.12×10^4(560)	0.849
0.002	0.214	5.14×10^4(355)	6.65×10^4(459)	0.209	7.65×10^4(527)	0.850
71						
0.2	0.193	4.74×10^4(327)	6.32×10^4(436)	0.263	7.42×10^4(512)	0.928
0.002	0.210	4.51×10^4(310)	6.15×10^4(424)	0.201	7.10×10^4(489)	0.992
180						
0.2	0.239	4.31×10^4(297)	6.62×10^4(456)	0.173	74.7×10^4(515)	0.817
260						
0.2	0.281	3.65×10^4(252)	6.78×10^4(468)	0.300	8.45×10^4(583)	0.844

*n = strain hardening exponent

TABLE IV

CYCLIC STRESS-STRAIN DATA AS A FUNCTION OF TEMPERATURE AT 640 C. P. M.

Temperature °C	n'	Fracture Strain in/in mm/mm	Yield Strength psi(mega N/m^2)	Ultimate Strength psi (mega N/m^2)
-50	0.2595	0.01862	4.55×10^4 (314)	4.99×10^4 (344)
-10	0.1756	0.01725	3.28×10^4 (226)	4.42×10^4 (305)
21	0.1867	0.01676	2.35×10^4 (162)	4.40×10^4 (304)
71	0.2126	0.01754	2.75×10^4 (189)	4.30×10^4 (297)

TABLE V

Experimental Data From the Cyclic Stress-Strain Tests

Temperature °C	Stress psi (mega N/m^2)	Strain in/in	N cycles @ 640 cpm
- 50	6649 (45.84)	0.00150	1280
	13305 (91.73)	0.00321	1280
	21445 (147.86)	0.00478	1280
	27356 (188.61)	0.00629	1280
	32543 (224.31)	0.00738	1280
	38451 (265.11)	0.00895	1280
	45477 (313.55)	0.01093	480
	46217 (318.65)	0.01230	427
	47141 (325.03)	0.01332	427
	48066 (331.40)	0.01469	374
	48066 (331.40)	0.01572	320
	49913 (344.14)	0.01657	320
	46212 (318.62)	0.01691	214
	48988 (337.76)	0.01811	214
	48063 (331.38)	0.01862	214
- 10	7079 (48.81)	0.00155	1280
	13409 (92.45)	0.00303	1280
	20869 (143.88)	0.00477	1280
	28700 (197.88)	0.00645	1280
	32800 (226.15)	0.00740	1280
	36531 (251.87)	0.00887	960
	39134 (269.82)	0.01062	640
	40624 (280.09)	0.01156	362
	41376 (285.28)	0.01237	320
	40624 (280.09)	0.01327	320
	41003 (282.71)	0.01378	320

Failed prematurely due to accidental notch.

Temperature °C	Stress psi (mega N/m^2)	Strain in/in	N cycles @ 640 cpm
21	6867 (47.34)	0.00147	1280
	16576 (114.29)	0.00354	1280
	23680 (163.27)	0.00516	1280
	30386 (209.50)	0.00685	1280
	34730 (239.45)	0.00825	1280
	37098 (255.78)	0.00958	1280
	39466 (272.11)	0.01142	640
	40255 (277.55)	0.01238	640
	41440 (285.72)	0.01326	320
	41834 (288.34)	0.01444	320
	42624 (293.88)	0.01529	374
	43413 (299.32)	0.01621	374
	44202 (304.76)	0.01676	320
71	9039 (62.32)	0.00157	1280
	13182 (90.89)	0.00322	1280
	21097 (145.46)	0.00508	1280
	27499 (189.59)	0.00680	1280
	31277 (215.65)	0.00802	640
	34667 (239.02)	0.00981	480
	35786 (246.74)	0.01059	427
	36919 (254.55)	0.01202	375
	38058 (262.40)	0.01310	320
	38804 (267.54)	0.01410	374
	39550 (272.69)	0.01467	320
	40493 (279.19)	0.01575	320
	41449 (285.78)	0.01664	320
	43321 (298.69)	0.01754	374

NOTE: Metallographic inspection of the specimens indicated that many micro-cracks develop during the test. This would mean that the true stress would be higher than that calculated had the true cross sectional area been known. This is particularly true near the latter part of the test where high strains are encountered.

TABLE VI

EXPERIMENTAL DATA FROM THE CRACK GROWTH RATE AND STRESS INTENSITY CALCULATIONS

Test Number	Environment	Temperature °C	Crack Growth Rate μin/cycle (m/cycle)	Stress Intensity psi$\sqrt{in}$ ($MNm^{-3/2}$)	ln C	m
26	Argon	- 50	1.0 (2.54 E-8)	19680 (21.63)	-61.61343	4.83
			1.21 (3.07 E-8)	20600 (22.64)		
			1.38 (3.51 E-8)	21260 (23.36)		
			1.51 (3.83 E-8)	21714 (23.86)		
			2.14 (5.44 E-8)	23600 (25.93)		
			2.49 (6.32 E-8)	24230 (26.62)		
			3.07 (7.79 E-8)	24800 (27.25)		
			3.75 (9.53 E-8)	25780 (28.33)		
9	Argon	- 50	1.33 (3.38 E-8)	25706 (28.24)	-59.78046	4.55
			1.5 (3.81 E-8)	26600 (29.23)		
			2.01 (5.11 E-8)	28300 (31.09)		
			2.6 (6.6 E-8)	29414 (32.91)		
			4.02 (1.02 E-7)	33290 (36.56)		
8	Argon	- 50	1.07 (2.72 E-8)	24200 (26.59)	-51.07308	3.72
			1.31 (3.30 E-8)	24700 (27.14)		
			1.38 (3.51 E-8)	25500 (28.02)		
			1.45 (3.68 E-8)	25600 (28.13)		
			1.62 (4.11 E-8)	25790 (28.34)		
			1.99 (5.05 E-8)	26800 (29.45)		
			2.36 (5.99 E-8)	28000 (30.78)		
			2.65 (6.73 E-8)	29414 (32.32)		
			2.82 (7.18 E-8)	29665 (32.60)		

Test Number	Environment	Temperature °C	Crack Growth Rate μin/cycle (m/cycle)	Stress Intensity psi√in($MNm^{-3/2}$)	ln C	m
18	Argon	- 50	2.25 (5.72 E-8)	21346 (23.45)	-56.67474	4.38
			3.38 (8.59 E-8)	23143 (25.43)		
			4.0 (1.02 E-7)	24789 (27.24)		
			4.3 (1.09 E-7)	24500 (26.92)		
			5.32 (1.35 E-7)	25630 (28.16)		
31	Argon	- 50	1.97 (5.0 E-8)	25664 (28.19)	-60.64211	4.67
			2.17 (5.51 E-8)	26309 (28.91)		
			2.25 (5.72 E-8)	26500 (29.12)		
			2.34 (5.94 E-8)	26745 (29.38)		
			2.61 (6.63 E-8)	27155 (29.83)		
			2.81 (7.14 E-8)	27500 (30.21)		
			3.05 (7.75 E-8)	28000 (30.76)		
			3.12 (7.93 E-8)	28400 (31.19)		
24	Argon	- 50	1.28 (3.25 E-8)	22018 (21.99)	-61.65813	4.81
			1.62 (4.15 E-8)	22782 (25.03)		
			2.09 (5.31 E-8)	25681 (27.12)		
			2.51 (6.38 E-8)	26200 (28.78)		
			3.55 (9.02 E-8)	26800 (29.45)		
			3.93 (9.98 E-8)	27580 (30.30)		

Test Number	Environment	Temperature °C	Crack Growth Rate μin/cycle (m/cycle)	Stress Intensity psi√in (MNm$^{-3/2}$)	ln C	m
11	Argon Load Variation	- 50	Start			
			1.23 (3.12 E-8)	23244 (25.54)		
			1.56 (3.96 E-8)	24141 (25.51)		
			1.68 (4.27 E-8)	24825 (27.28)		
			1.77 (4.49 E-8)	26137 (28.73)		
			Decrease Load			
			0.0 (0.0)	17740 (19.50)		
			" "	" "		
			" "	" "		
			" "	" "		
			" "	" "		
			Increase Load			
			1.69 (4.27 E-8)	30182 (33.16)		
			2.08 (5.28 E-8)	31209 (34.29)		
			6.42 (1.63 E-7)	32500 (35.72)		
			7.82 (1.98 E-7)	32740 (35.97)		
48	Argon Heat Treated	- 50	1.89 (4.80 E-8)	20020 (21.98)	-115.02896	10.29
			2.31 (5.87 E-8)	20270 (22.27)		
			3.05 (7.75 E-8)	20680 (22.72)		
			3.57 (9.07 E-8)	21115 (23.19)		
			3.84 (9.75 E-8)	21430 (23.54)		

Test Number	Environment	Temperature °C	Crack Growth Rate μin/cycle (m/cycle)	Stress Intensity psi$\sqrt{in}$ ($MNm^{-3/2}$)	ln C	m
33	Argon Load Variation	- 50	Start			
			2.34 (5.94 E-8)	22582 (24.81)		
			2.46 (6.25 E-8)	24361 (26.76)		
			2.73 (6.93 E-8)	25550 (28.07)		
			2.75 (6.98 E-8)	26170 (28.76)		
33	Argon Load Variation	- 50	Decrease Load			
			1.59 (4.04 E-8)	19422 (21.34)		
			1.13 (2.87 E-8)	19417 (21.33)		
			1.07 (2.72 E-8)	19690 (21.63)		
			1.15 (2.92 E-8)	20260 (22.26)		
			Increase Load			
			4.07 (1.03 E-7)	21000 (23.07)		
			5.87 (1.49 E-7)	37660 (41.38)		
			7.05 (1.79 E-7)	33768 (37.10)		
27	Argon Heat Treated	- 50	2.20 (5.59 E-8)	22470 (24.69)	-121.07533	10.79
			2.66 (6.76 E-8)	22720 (24.97)		
			2.98 (7.57 E-8)	23100 (25.35)		
			3.57 (9.07 E-8)	23300 (25.61)		
			5.01 (1.27 E-7)	24160 (26.55)		
			5.60 (1.42 E-7)	24270 (26.66)		

Test Number	Environment	Temperature °C	Crack Growth Rate μin/cycle (m/cycle)	Stress Intensity psi√in($MNm^{-3/2}$)	ln C	m
36	Hydrogen	- 50	1.25 (3.18 E-8)	18815 (20.67)	-132.67635	12.07
			1.59 (4.04 E-8)	19522 (21.45)		
			3.63 (9.22 E-8)	21078 (23.16)		
			18.99 (4.82 E-7)	23600 (25.93)		
			22.55 (5.73 E-7)	24250 (26.64)		
47	Hydrogen	- 50	Unstable (not sufficient data)			
12	Argon	- 10	1.11 (2.82 E-8)	20980 (23.05)	- 84.65299	7.17
			1.79 (4.55 E-8)	21309 (23.41)		
			2.67 (6.78 E-8)	22120 (24.30)		
			2.91 (7.39 E-8)	22990 (25.26)		
			3.04 (7.72 E-8)	23105 (25.38)		
62	Argon	- 10	1.04 (2.64 E-8)	18424 (20.24)	- 73.46250	6.08
			1.42 (3.61 E-8)	18930 (20.80)		
			1.77 (4.49 E-8)	19882 (21.78)		
			2.44 (6.19 E-8)	20890 (22.95)		
			4.58 (1.16 E-7)	23220 (25.51)		
			4.78 (1.21 E-7)	23440 (25.75)		

Test Number	Environment	Temperature °C	Crack Growth Rate μin/cycle (m/cycle)	Stress Intensity psi√in(MNm$^{-3/2}$)	ln C	m
29	Argon	- 10	1.26 (3.2 E-8)	17456 (19.18)	-83.72695	7.18
			1.6 (4.06 E-8)	17930 (19.69)		
			1.82 (4.62 E-8)	18400 (20.22)		
			2.15 (5.46 E-8)	18650 (20.49)		
			2.58 (6.55 E-8)	19290 (21.19)		
5	Argon	21	3.5 (8.89 E-8)	24414 (26.82)	-65.99174	5.28
			4.06 (1.03 E-7)	25380 (27.88)		
			5.06 (1.29 E-7)	26520 (29.14)		
			6.12 (1.55 E-7)	27575 (30.29)		
			6.72 (1.71 E-7)	27580 (30.30)		
			6.92 (1.76 E-7)	27850 (30.59)		
			7.07 (1.79 E-7)	27950 (30.70)		
20	Argon	21	3.01 (7.65 E-8)	22750 (24.99)	-66.31154	5.37
			3.92 (9.96 E-8)	23300 (25.60)		
			5.24 (1.33 E-7)	23966 (26.33)		
			7.25 (1.84 E-7)	25063 (27.54)		
			9.37 (2.38 E-7)	26666 (29.30)		
17	Argon	21	1.52 (4.00 E-8)	16560 (18.19)	-62.38602	5.04
			1.58 (4.01 E-8)	16755 (18.40)		
			1.78 (4.52 E-8)	16800 (18.61)		
			1.95 (4.95 E-8)	17684 (19.31)		
			2.17 (5.48 E-8)	17737 (19.49)		
			2.52 (6.40 E-8)	17807 (19.56)		

Test Number	Environment	Temperature °C	Crack Growth Rate μin/cycle (m/cycle)	Stress Intensity psi√in($MNm^{-3/2}$)	ln C	m
19	Argon	21	2.25 (5.73 E-8)	22524 (24.75)	-69.54131	5.64
			3.61 (9.17 E-8)	24751 (27.19)		
			5.79 (1.57 E-7)	26700 (29.34)		
			6.36 (1.61 E-7)	26750 (29.36)		
			7.23 (1.84 E-7)	27833 (30.57)		
40	Argon	21	1.32 (3.35 E-8)	17996 (19.77)	-76.30173	6.40
			1.66 (4.22 E-8)	18630 (20.47)		
			2.13 (5.41 E-8)	19664 (21.61)		
			2.52 (6.40 E-8)	19937 (21.91)		
			4.34 (1.10 E-7)	21640 (23.78)		
32	Argon	21	1.19 (3.02 E-8)	17001 (18.68)	-51.45910	3.91
			1.55 (3.94 E-8)	17200 (18.89)		
			1.82 (4.62 E-8)	17964 (19.74)		
			2.18 (5.54 E-8)	18562 (20.39)		
			2.38 (6.04 E-8)	19700 (21.64)		
			2.66 (6.74 E-8)	20100 (22.08)		
			3.05 (7.75 E-8)	20260 (22.26)		
			3.60 (9.14 E-8)	21300 (23.40)		
			3.86 (9.80 E-8)	21534 (23.66)		

Test Number	Environment	Temperature °C	Crack Growth Rate μin/cycle (m/cycle)	Stress Intensity psi√in ($MNm^{-3/2}$)	ln C	m
6	Argon Heat Treated	21	2.48 (6.29 E-8)	20377 (22.38)	-58.68549	4.61
			2.61 (6.63 E-8)	21265 (23.36)		
			3.10 (7.87 E-8)	21836 (23.99)		
			4.06 (1.03 E-7)	22726 (24.97)		
54	Argon Heat Treated	21	1.39 (3.53 E-8)	20800 (22.85)	-68.76316	5.56
			2.22 (5.64 E-8)	21860 (24.02)		
			2.89 (7.34 E-8)	23593 (25.92)		
			3.86 (9.80 E-8)	24500 (26.90)		
14	Hydrogen	21	Initial Growth			
			1.38 (3.51 E-8)	18141 (19.93)	-49.45584	3.68
			1.89 (4.80 E-8)	18951 (20.82)		
			2.22 (5.64 E-8)	19734 (21.68)		
			2.44 (6.19 E-8)	20418 (22.44)		
			2.77 (7.04 E-8)	21790 (23.94)		
			Rapid Unstable Crack Growth			
49	Hydrogen	21	Initial Growth			
			1.93 (4.90 E-8)	19218 (21.12)	-62.58971	5.01
			2.46 (6.25 E-8)	20408 (22.42)		
			3.40 (8.64 E-8)	21356 (23.46)		
			4.23 (1.07 E-7)	22624 (24.88)		
			5.50 (1.39 E-7)	23733 (26.07)		
			Rapid Unstable Crack Growth			

Test Number	Environment	Temperature °C	Crack Growth Rate μin/cycle (m/cycle)	Stress Intensity psi$\sqrt{in}$ ($MNm^{-3/2}$)	ln C	m
50	Hydrogen	21	1.06 (2.69 E-8)	19272 (21.27)	-76.90022	6.39
			1.11 (2.82 E-8)	19435 (21.35)		
			1.39 (3.53 E-8)	20182 (22.17)		
			1.89 (4.80 E-8)	21000 (23.07)		
			2.31 (5.87 E-8)	21636 (23.77)		
			2.83 (7.18 E-8)	22545 (24.77)		
			3.61 (9.17 E-8)	23350 (25.65)		
			4.25 (1.08 E-7)	23950 (26.32)		
			Did not fail rapidly, probably due to excess water vapour in gas.			
10	Argon	71	1.44 (3.66 E-8)	19150 (21.04)	-44.42163	3.14
			1.61 (4.09 E-8)	19570 (21.50)		
			1.76 (4.47 E-8)	20663 (22.70)		
			1.97 (5.00 E-8)	21217 (23.31)		
			3.37 (8.56 E-8)	24985 (27.45)		
45	Argon	71	.976 (2.48 E-8)	18011 (19.79)	-35.61907	2.22
			1.26 (3.20 E-8)	20020 (21.99)		
			1.46 (3.71 E-8)	20640 (22.67)		
			1.66 (4.22 E-8)	23514 (25.84)		
			2.00 (5.08 E-8)	24300 (26.69)		
			2.20 (5.59 E-8)	25180 (27.60)		

Test Number	Environment	Temperature °C	Crack Growth Rate μin/cycle (m/cycle)	Stress Intensity psi$\sqrt{in}$ ($MNm^{-3/2}$)	ln C	m
0	Argon	71	2.16 (5.49 E-8)	18857 (20.72)	-38.89628	2.62
			2.53 (6.43 E-8)	20240 (22.24)		
			3.10 (7.87 E-8)	21942 (24.12)		
			3.68 (9.35 E-8)	23200 (25.49)		
			4.19 (1.06 E-8)	24266 (26.66)		

TABLE VII

INITIATION TIMES IN CYCLES (X1000)

Temperature °C	Environment	Cycles
-50	Argon	81.8 ± 9.8*
-10	Argon	58.7 ± 15.6*
21	Argon	34.0 ± 4.7*
71	Argon	50.0 ± 11.0*
-50	Hydrogen	86.0 ave. of 3 tests
-10	Argon (heat treated)	86.0 ave. of 3 tests
21	Hydrogen	40.0 ave. of 3 tests
21	Argon (heat treated)	40.0 ave. of 4 tests

* 90% confidence

TABIE VIII

CONSTANTS, ln C and m AS DETERMINED FROM EXPERIMENTAL DATA

Temperature °C	m	ln C	r
-50	4.49 ± 0.25	-58.57366 ± 2.47434	0.992
-10	6.81 ± 0.687	-80.61415 ± 6.76132	0.961
21	5.195 ± 0.421	-63.86812 ± 4.26183	0.981
71	2.66 ± 0.499	-39.64566 ± 4.84359	0.994

TABLE IX

FATIGUE LIFE IN CYCLES FOR THE VARIOUS TEST CONDITIONS

Environment	Temperature °C	Number of Cycles (X1000) to failure
Argon	-50	293 ± 30*
Argon	-10	231 ± 28*
Argon	21	132 ± 16*
Argon	71	233 ± 11*
Argon (heat treated)	-50	240 average of 3 tests
Argon (heat treated)	21	142 average of 3 tests
Hydrogen	-50	150 average of 3 tests
Hydrogen	21	90 average of 4 tests

* 90% confidence level
minimum of 4 tests

TABLE X

Experimental Data Illustrating the ln C and m Relationship With Error Analysis Included

Anctil and Kula (25) 4340 (austinize and oil quench) Tests at -45 °C

Tempering Temperature °C	m	ln C actual	ln C predicted	Δln C	Error %
204	3.31	-44.27079	-44.56357	-.29278	-.66
260	2.95	-41.10966	-41.03761	-.07205	.175
316	2.46	-36.14817	-36.23839	-.09022	-.249
371	3.05	-42.16087	-42.01704	.14383	.341
427	3.15	-43.15419	-42.99647	.15772	.365

m_o = -1.23994
A = -.10210
correlation coefficient = .99818

Tests at 23 °C

204	2.97	-41.20369	-41.21557	-0.01188	-0.0288
260	2.49	-36.51809	-36.47997	0.03812	0.104
316	2.23	-33.94951	-33.91486	0.03465	0.102
371	2.25	-34.05335	-34.11217	0.05882	-0.173

m_o = -1.20761
A = -0.10136
correlation coefficient = .99991

Miller (26) 4340 815 (austinize and oil quench) Tests at 23 °C

93	6.73	-78.85654	-78.94421	-0.08767	-0.111
260	3.29	-45.01169	-45.39306	-0.38137	-0.847
538	3.17	-44.27123	-44.22267	0.04856	0.109
760	3.95	-52.25742	-51.83020	0.42722	0.817

m_o = -1.36415
A = -0.10253
correlation coefficient = .99979

Experimental Data used in Tomkins Equation (54)

Temperature of Test °C	m_t	$\ln C^l$ actual	$\ln C^l$ predicted	$\Delta \ln C^l$	Error %
- 50	5.85	-70.08638	-69.85155	0.23483	0.335
- 10	7.69	-89.15345	-88.96664	0.18690	0.209
21	7.35	-85.49979	-85.43450	0.06529	0.0764
71	6.70	-78.34404	-78.68192	-0.33788	-0.432

m_o = -0.87384
A = -0.09626
correlation coefficient = .9995

Temperature of test °C	m	ln C actual	ln C predicted	Δ ln C	Error %
- 50	4.49	-58.57366	-57.77986	0.7938	1.3552
- 10	6.81	-80.61415	-80.52053	0.09362	0.116
21	5.19	-63.86812	-64.60697	0.73885	1.157
71	2.66	-39.64566	-39.75432	-0.10866	-0.274

m_o = -1.38699
A = -0.10180
correlation coefficient = .99926

TABLE XI

VALUES OF CONSTANTS TAKEN FROM A. S. M. PUBLICATION "DIFFUSION IN BODY CENTERED CUBIC METALS" 1964

Values for Nitrogen

Relaxation Time τ_R (sec)	Mean Time of Stay 3/2 τ_R (sec)	D cm^2/sec	Temperature
3.996×10^{3}	5.994×10^{3}	5.685×10^{-21}	223° K
8.058	12.0	2.819×10^{-18}	263° K
2.33×10^{-1}	0.349	9.745×10^{-17}	293° K
2.52×10^{-3}	0.0038	9.016×10^{-15}	343° K

Values for Carbon

Relaxation Time τ_R (sec)	Mean Time of Stay 3/2 τ_R (sec)	D cm^2/sec	Temperature
2.75×10^{4}	4.125×10^{4}	8.255×10^{-22}	223° K
39.46	59.2	5.76×10^{-19}	263° K
0.9399	1.41	2.417×10^{-17}	293° K
7.922×10^{-3}	1.19×10^{-2}	2.86×10^{-15}	343° K

TABLE XII

COMPARISON OF CRACK INITIATION TIME WITH VARIOUS MATERIAL PROPERTIES

Environment	Grain Size (mm)	Temperature °C	Crack Initiation No. x 10^3	Static n	Cyclic Cumulative n^1	Cyclic non-cumulative n^{11}	m
Argon	0.022 a	- 50	82.0	0.202 *	0.259	0.223	4.495
	0.033 b			0.213 **			
Argon	0.022 a	- 10	59.0	0.216 *	0.175	0.075	6.81
	0.033 b			0.223 **			
Argon	0.022 a	21	34.0	0.209 *	0.186	0.105	5.195
	0.033 b			0.214 **			
Argon	0.022 a	71	50.0	0.193 *	0.212	0.102	2.66
	0.033 b			0.210 **			
Hydrogen	0.022 a	- 50	86.0				
	0.033 b						
Hydrogen	0.022 a	21	40.0				
	0.033 b						
Argon heat-treated	0.026 a	- 50	86.0				
	0.042 b						
Argon heat-treated	0.026 a	21	40.0				
	0.042 b						

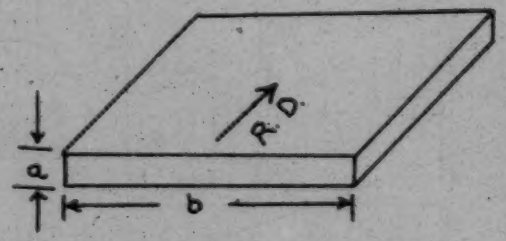

Strain rate 0.2 in/in/min = 0.2 mm/mm/min*
0.002 in/in/min = 0.002 mm/mm/min**

TABLE XIII

SIZE OF PLASTIC ZONES IN STEEL SPECIMENS

Environment	Temperature °C	Radius of Plastic Zone, in (mm) reversed r_r	surface r_s	r_s / r_r
Argon	-50	4.5×10^{-4} (0.0114)	0.0251 (0.636)	56
	-10	7.0×10^{-4} (0.0178)	0.0270 (0.685)	38
	21	2.0×10^{-3} (0.0510)	0.0368 (0.990)	18
	71	1.0×10^{-3} (0.0259)	0.0490 (1.240)	49
Hydrogen	-50	not detectable	0.0335 (0.85)	
	21	" "	0.049 (1.24)	

TABLE XIV

CRACK PROPAGATION RATE (IN/CYCLE)

Test Temperature °C	Experimental	Tomkins n^{I}	Tomkins n^{II}
-50	7.85×10^{-7}	7.02×10^{-6}	2.65×10^{-7}
-10	1.90×10^{-6}	1.14×10^{-6}	1.90×10^{-11}
21	3.13×10^{-6}	4.36×10^{-6}	1.41×10^{-9}
71	1.67×10^{-6}	5.02×10^{-6}	1.59×10^{-9}

FIGURES

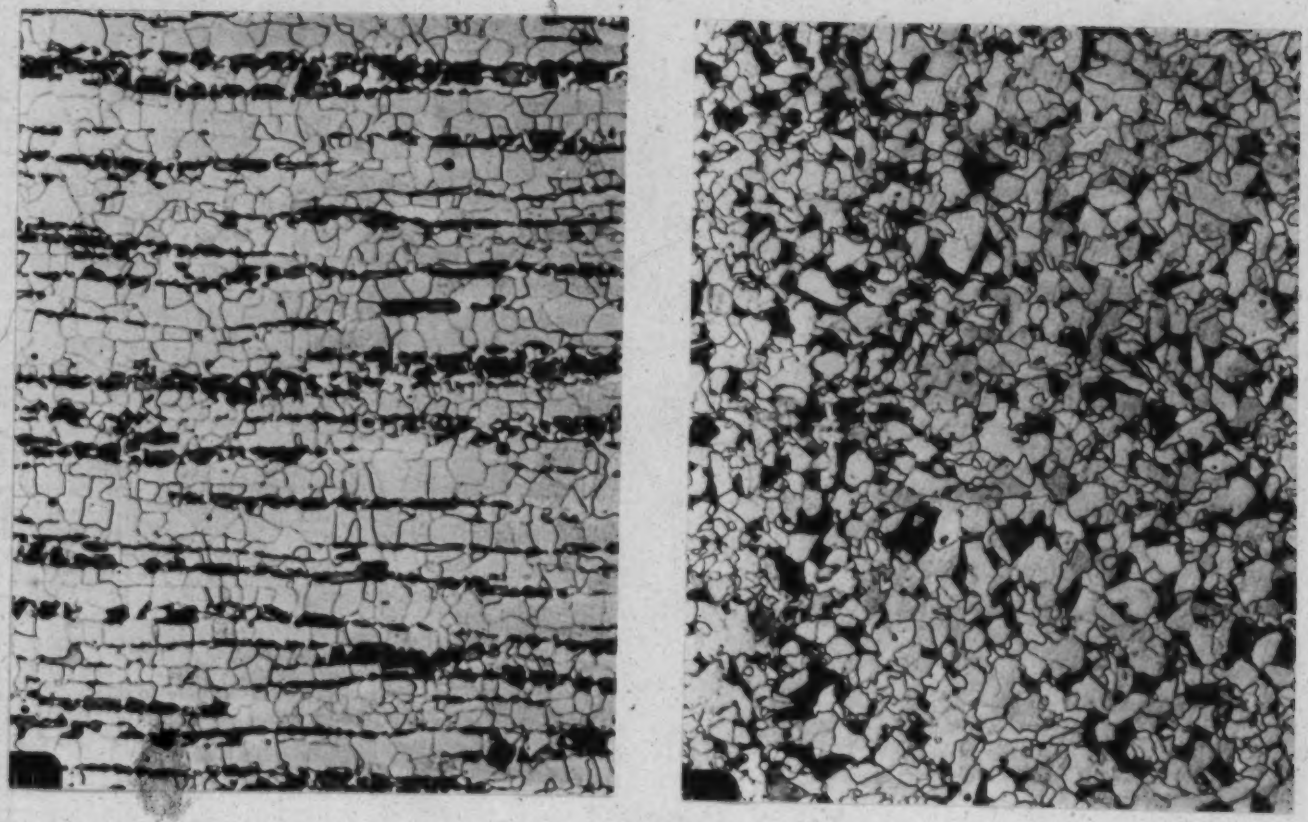

Parallel to the rolling direction

Perpendicular to the rolling direction

Figure 1. Microstructure of test material. (X200)

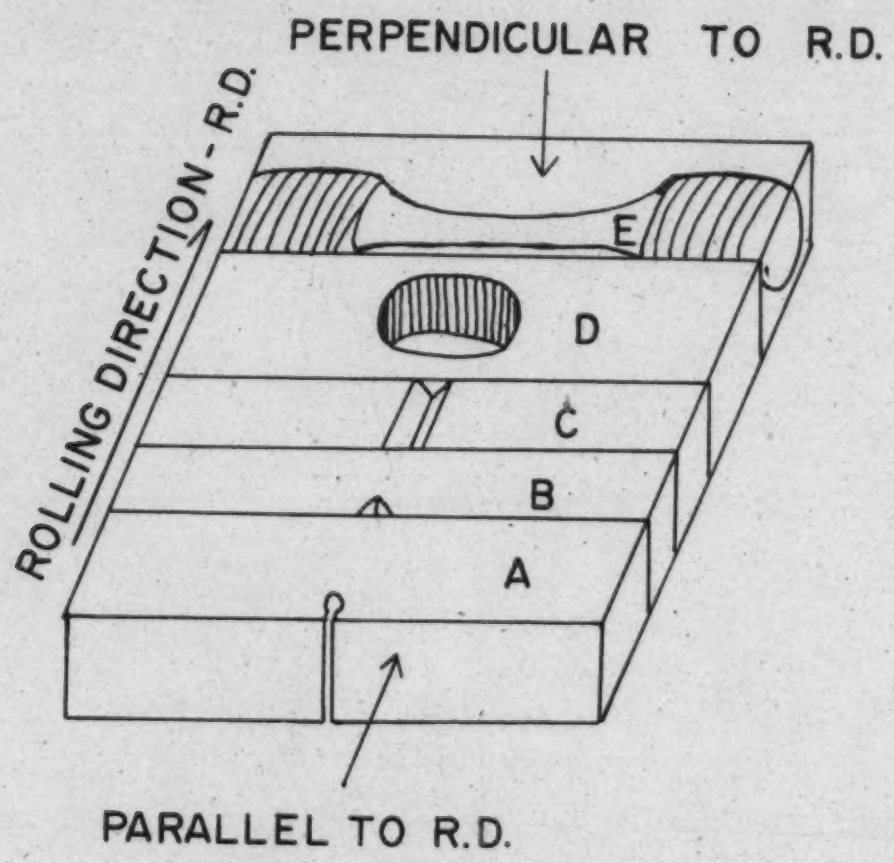

Figure 2. Schematic drawing showing the test specimen orientations with respect to the rolling direction.

A. Fatigue test specimen (parallel to R. D.).
B. Charpy impact test specimen (parallel to R. D.).
C. Charpy impact test specimen (perpendicular to R. D.).
D. Cyclic stress-strain specimens (parallel to R. D.).
E. Static tensile specimens (parallel to R. D.).

Figure 2A. Manganese sulphide inclusion content of test material (X200)

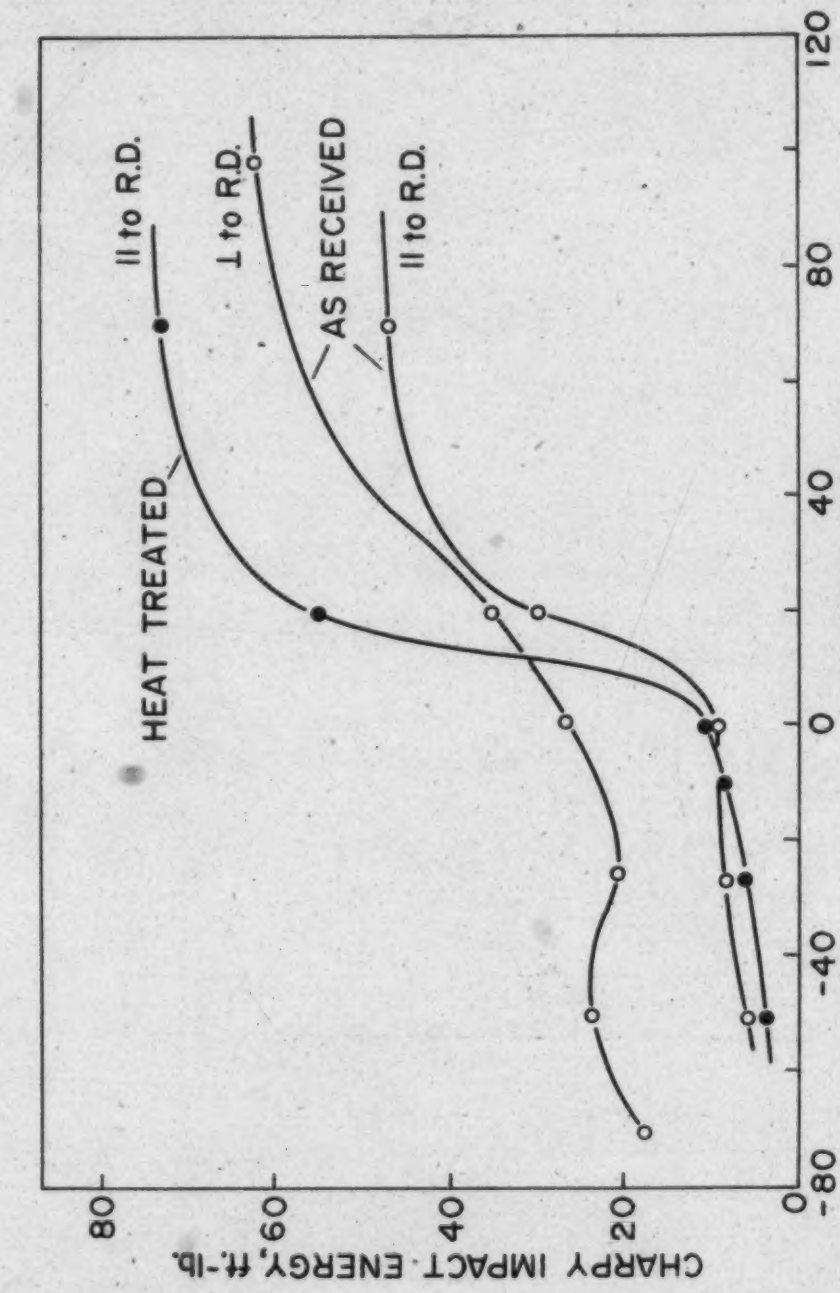

Figure 3. Charpy impact energy curves for the test material as a function of temperature and specimen orientation.

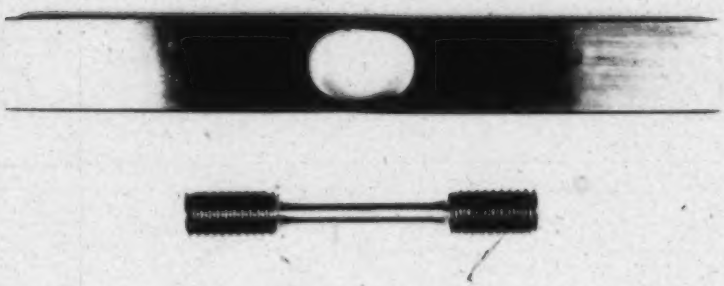

Figure 4. Test specimens used for cyclic, (upper) and static stress-strain data determinations.

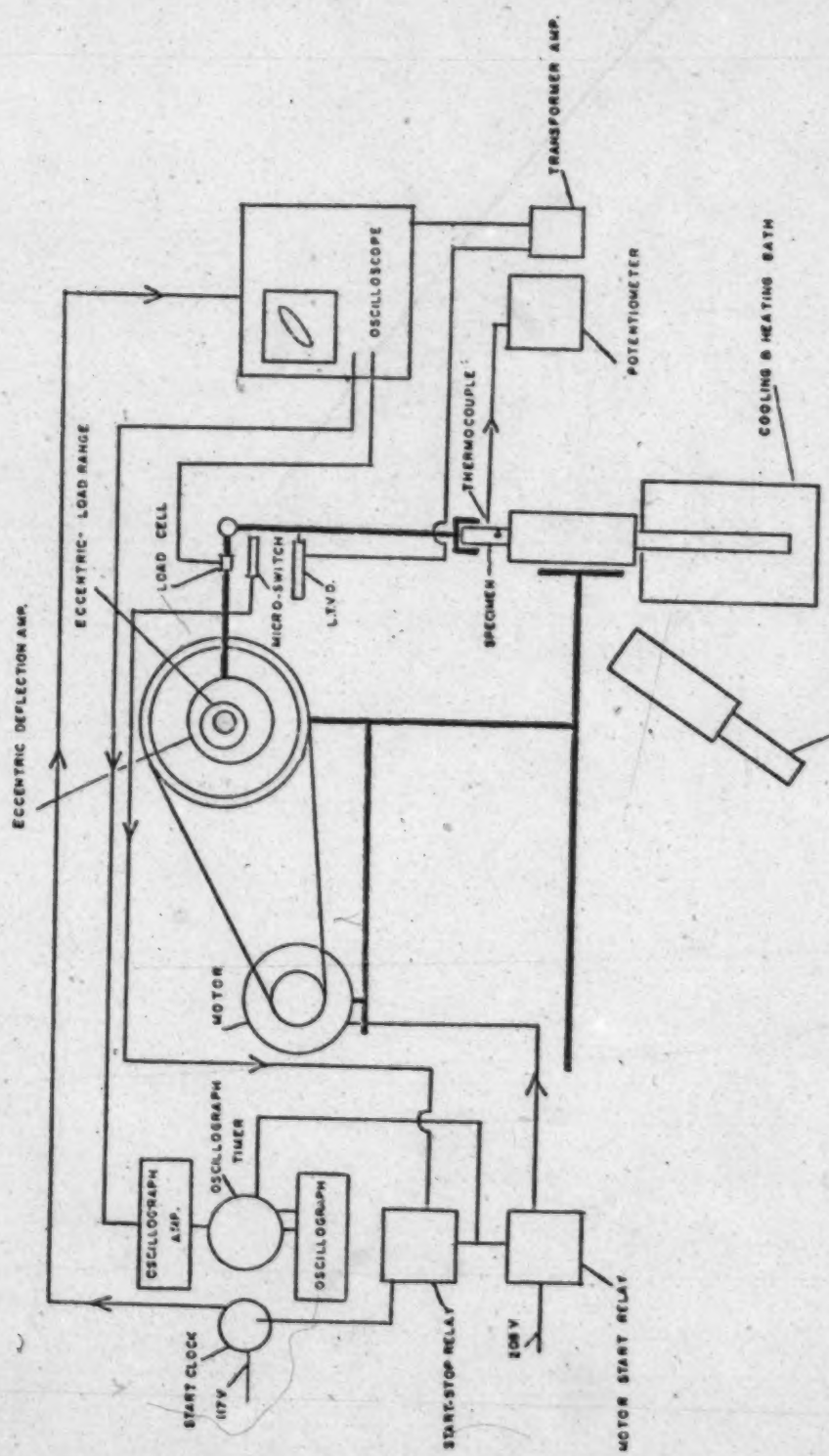

Figure 5 Schematic drawing of the fatigue testing machine.

Figure 6. Photograph of fatigue testing apparatus.

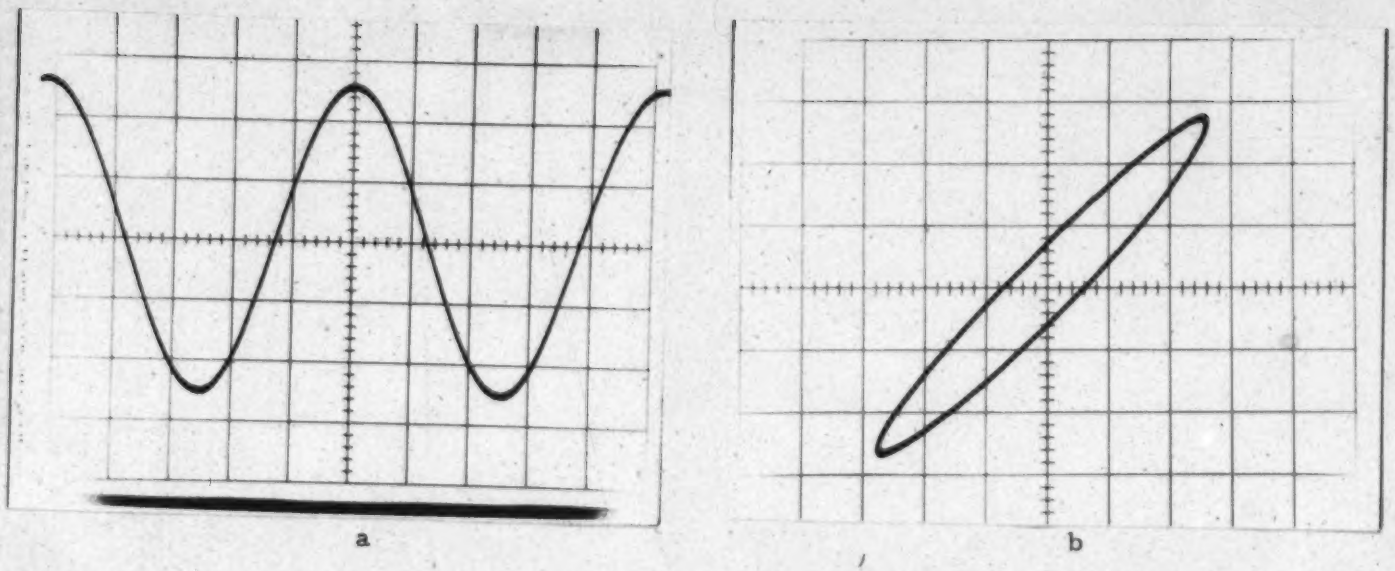

Figure 7. Load versus time (a) and load versus deflection loop (b)

Figure 8. Close up of the bottom grips with the specimen in place.

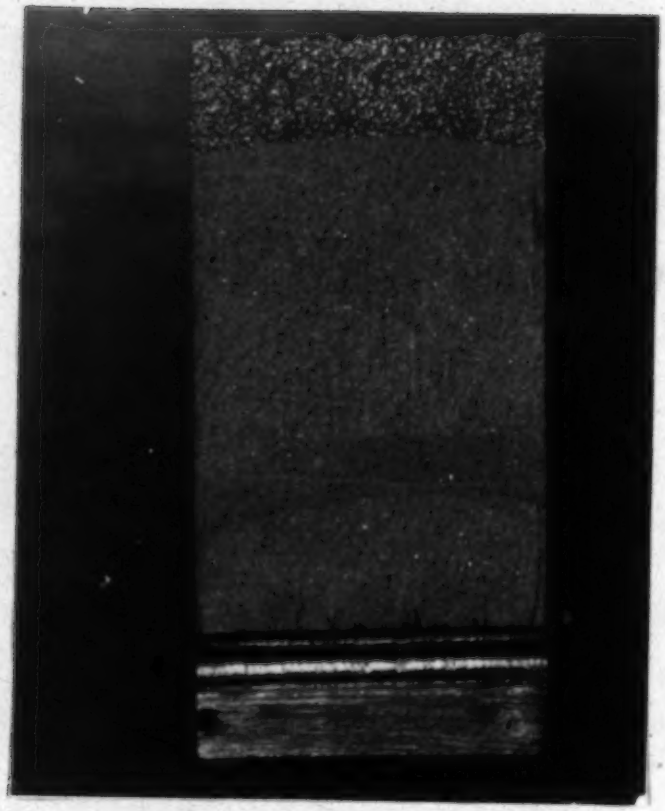

Figure 9. Fracture surface of a fatigue test specimen which illustrates the crack front (X5. 4).

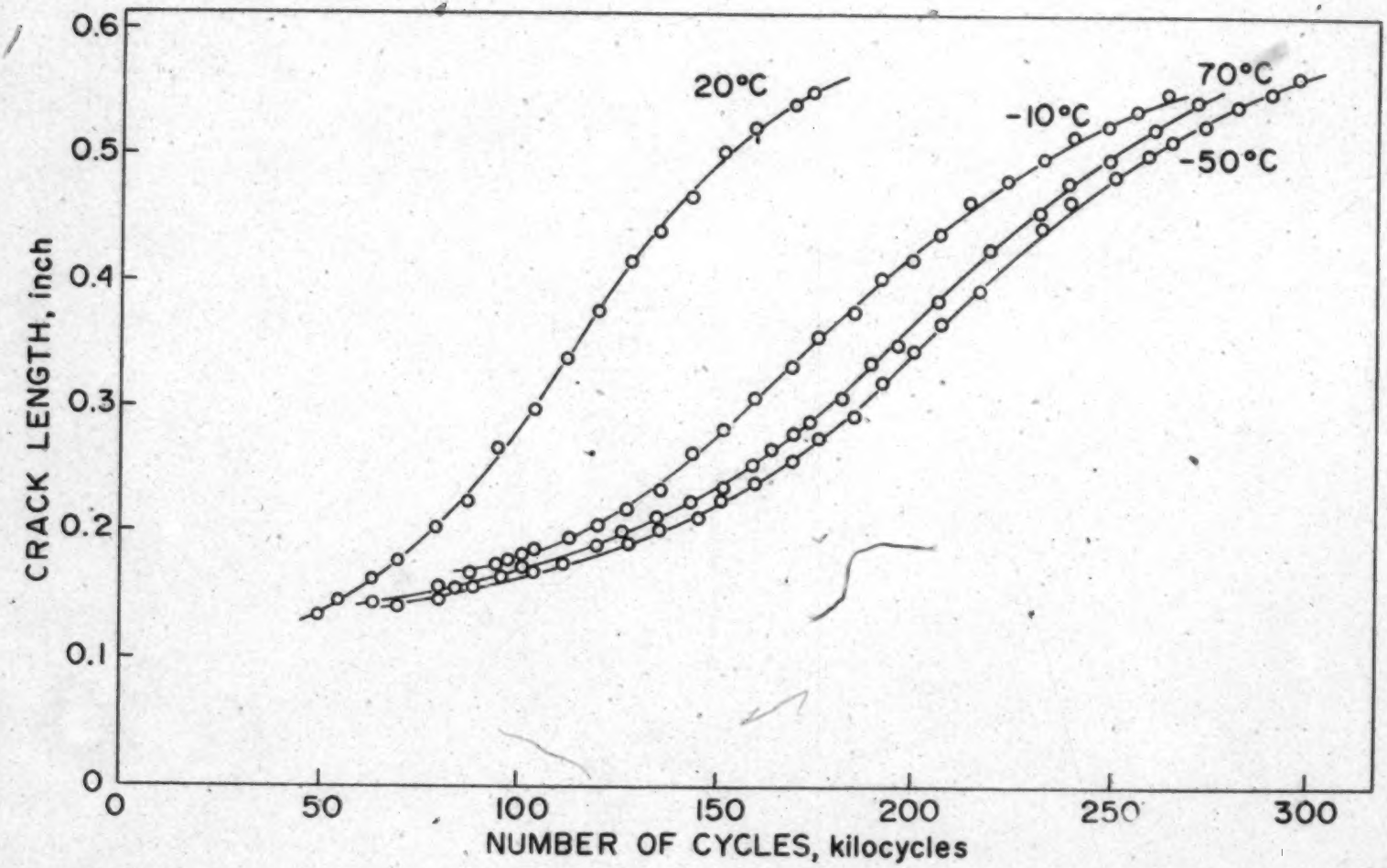

Figure 10. Typical crack length versus number of cycles for the four test temperatures and argon environment.

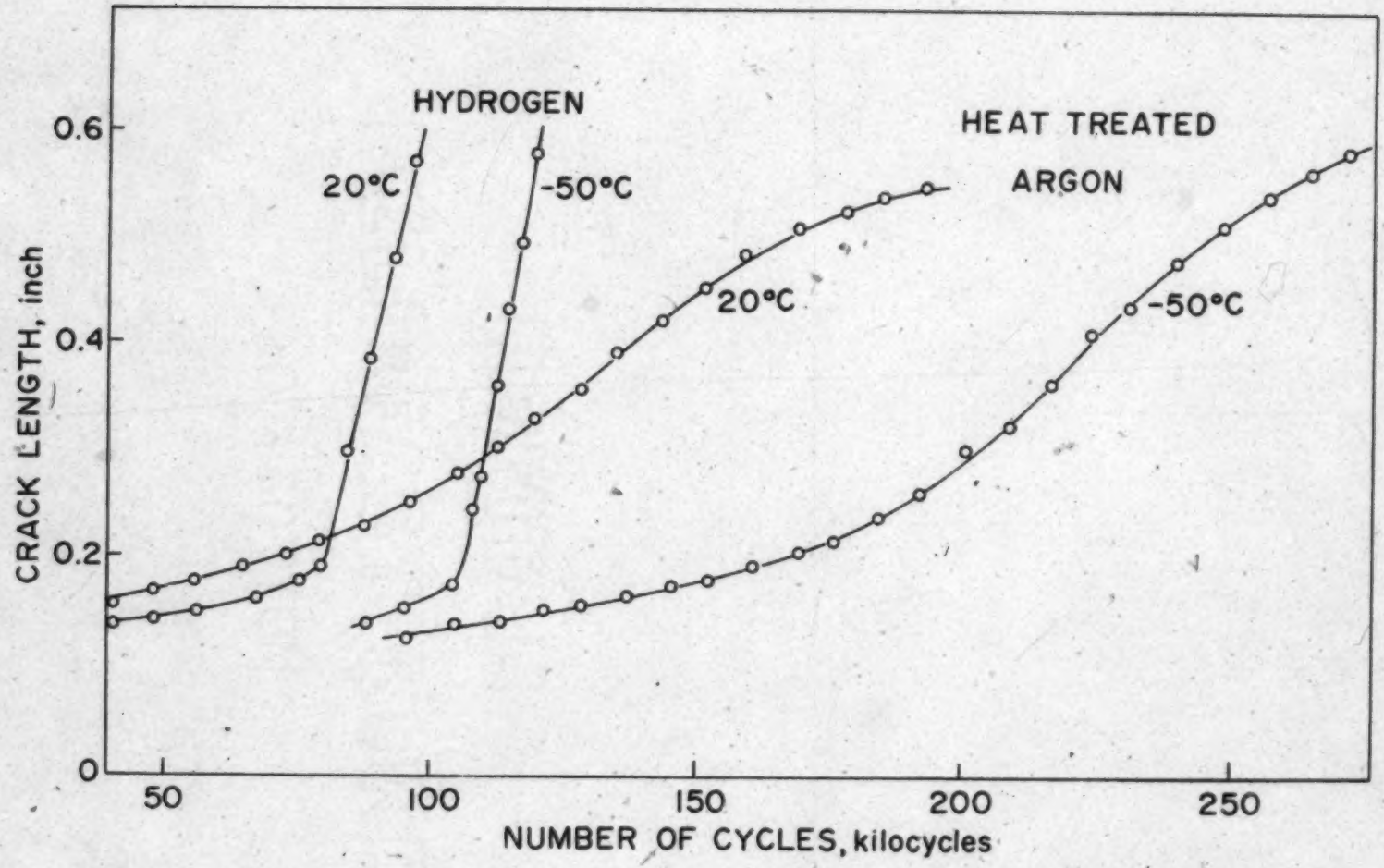

Figure 11. Typical crack length versus number of cycles for specimens tested in hydrogen and the heat-treated specimens tested in argon.

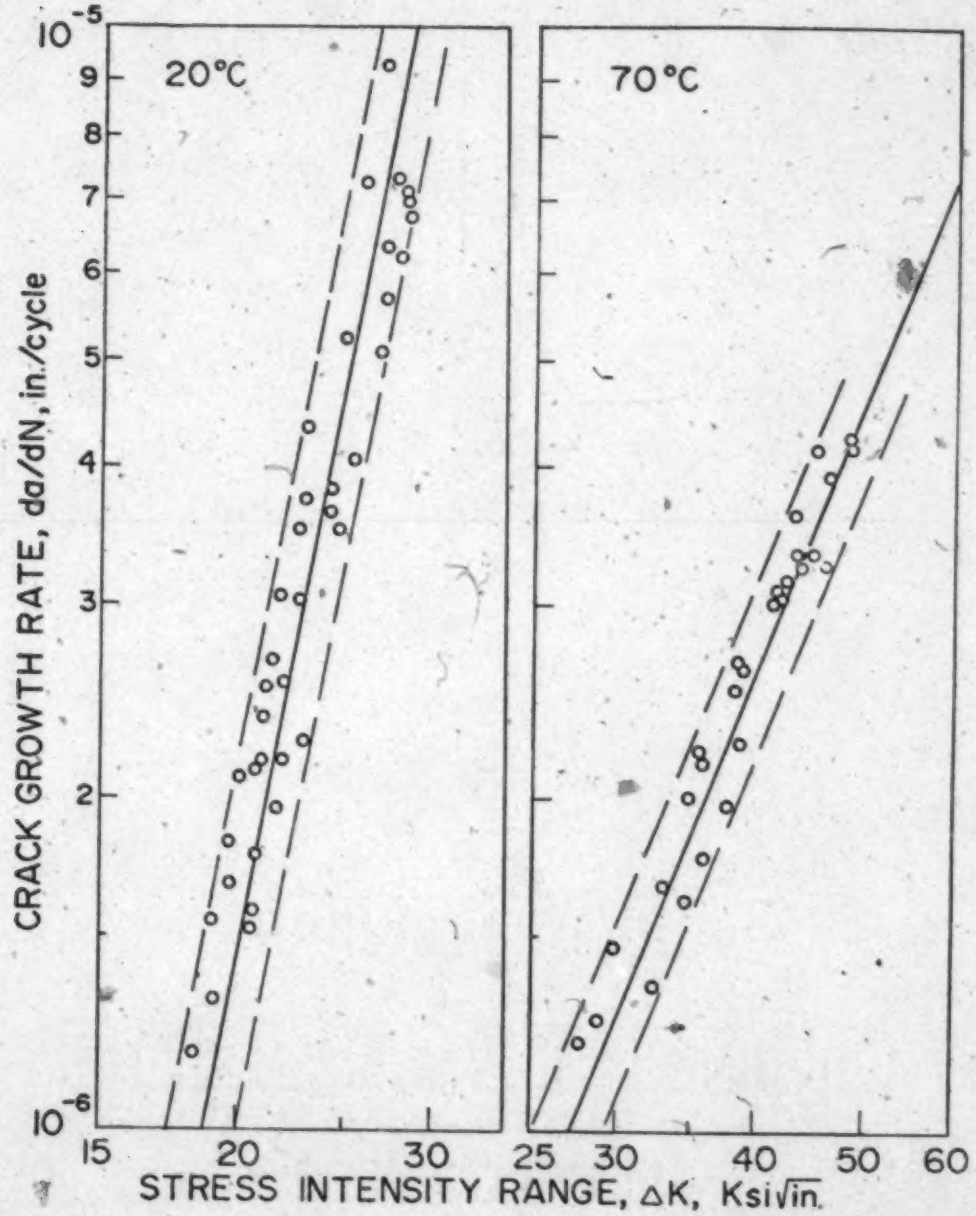

Figure 12. Crack propagation rate as a function of stress intensity range for tests in argon at 20 and 70°C.

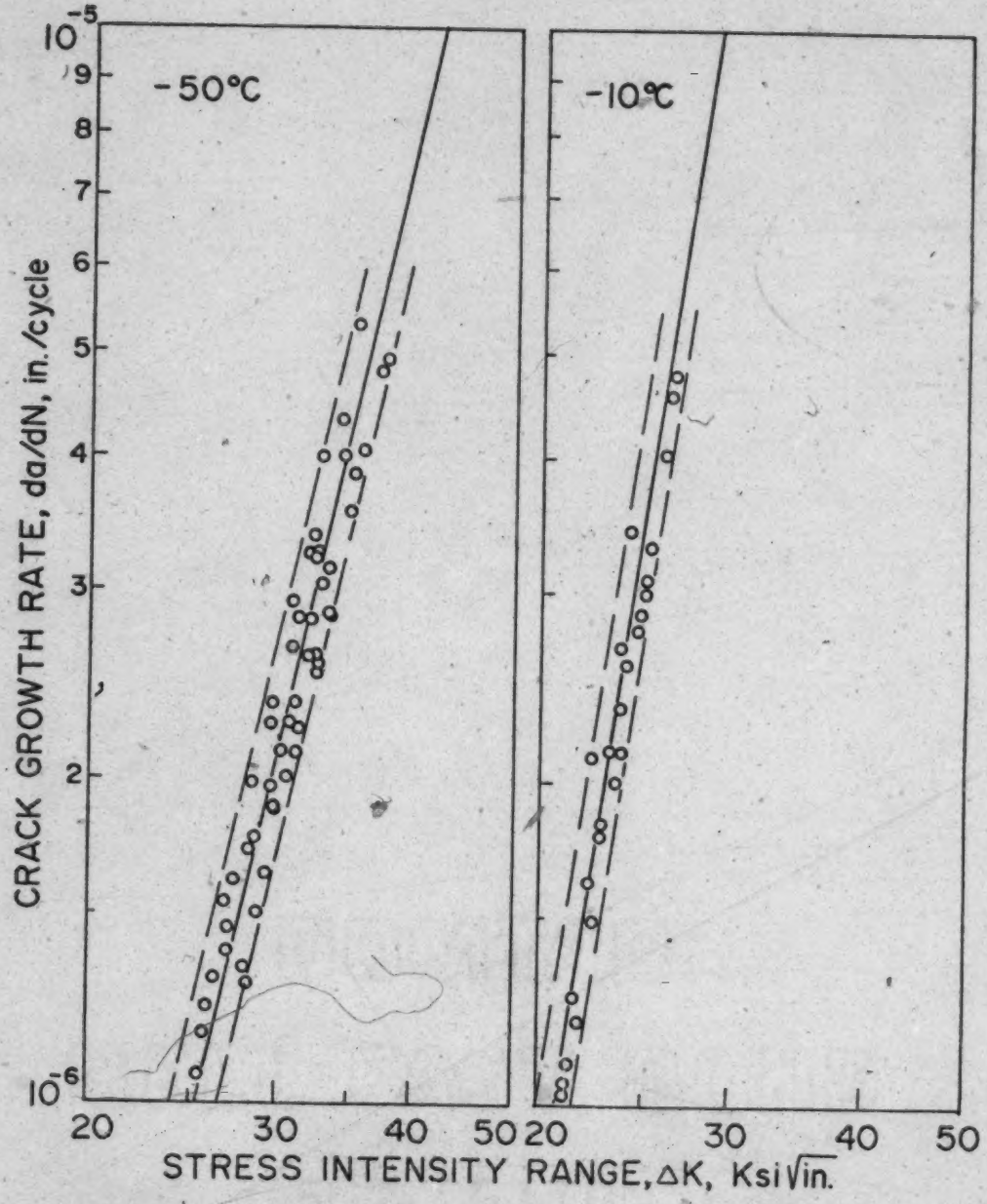

Figure 12A. Crack propagation rate as a function of stress intensity range for tests in argon at -50 and -10°C.

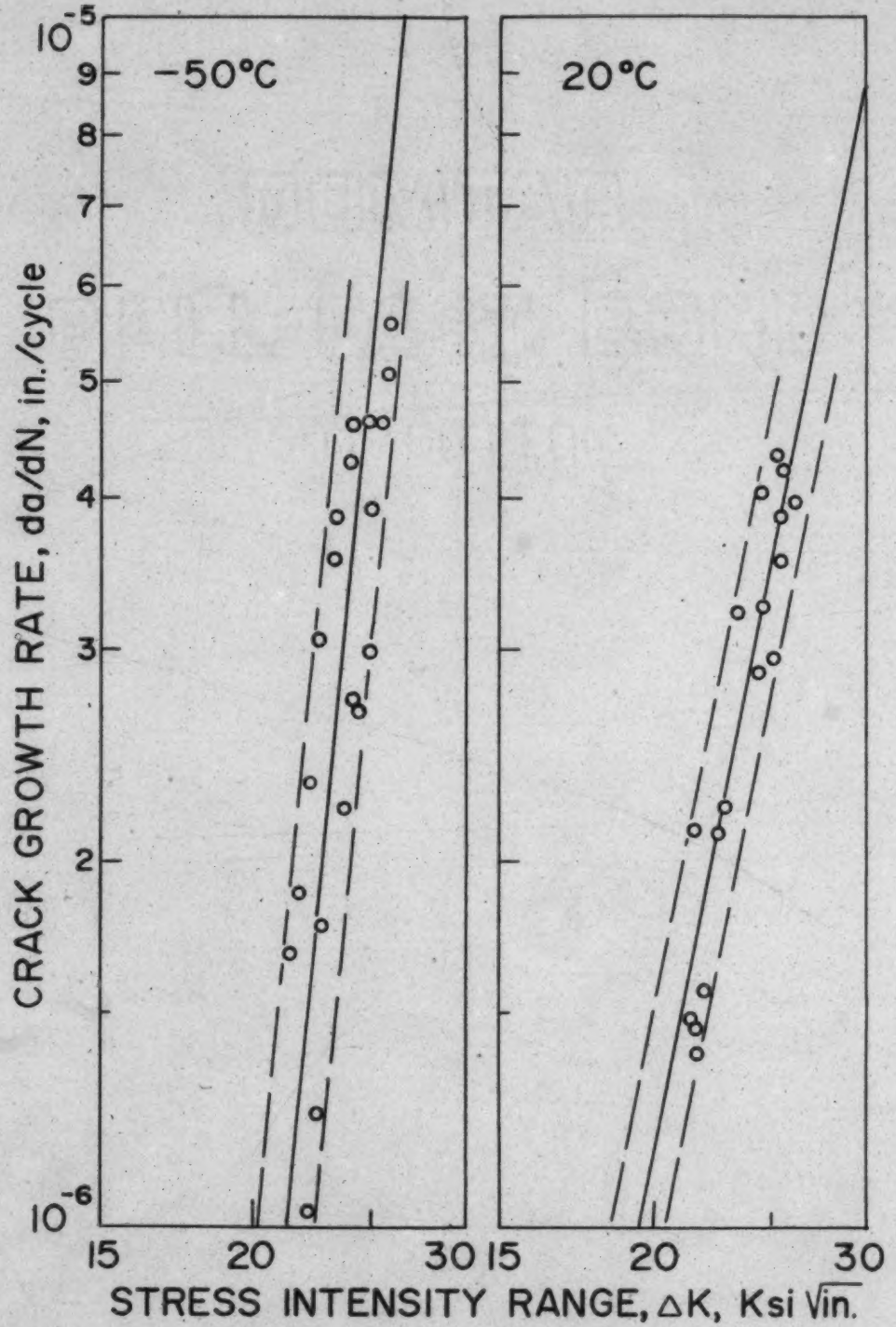

Figure 13. Crack propagation rate as a function of stress intensity range for the heat treated specimens tested in argon at -50 and 20 °C.

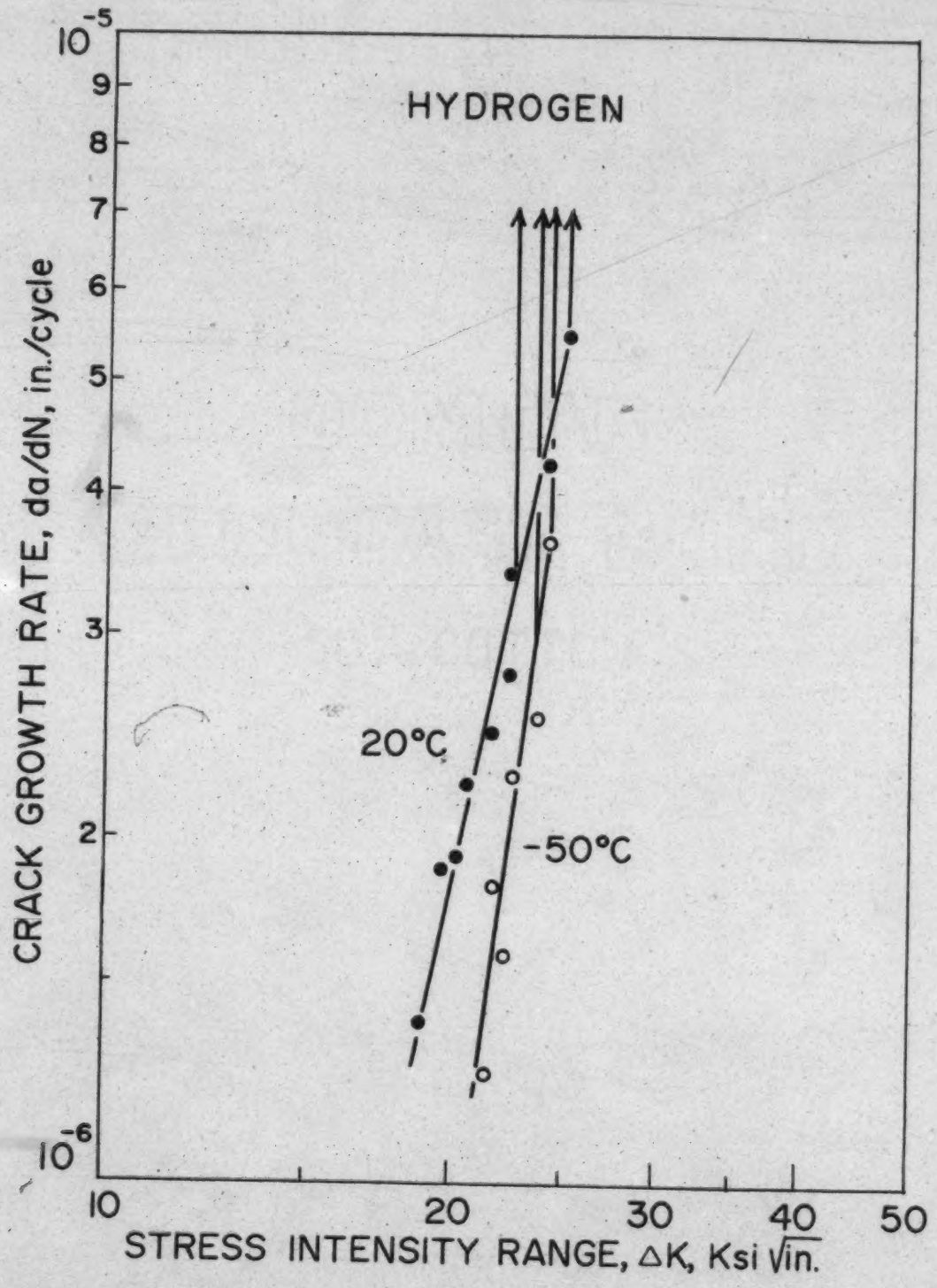

Figure 14. Crack propagation rate as a function of stress intensity range for specimens tested in hydrogen at -50 and 20° C.

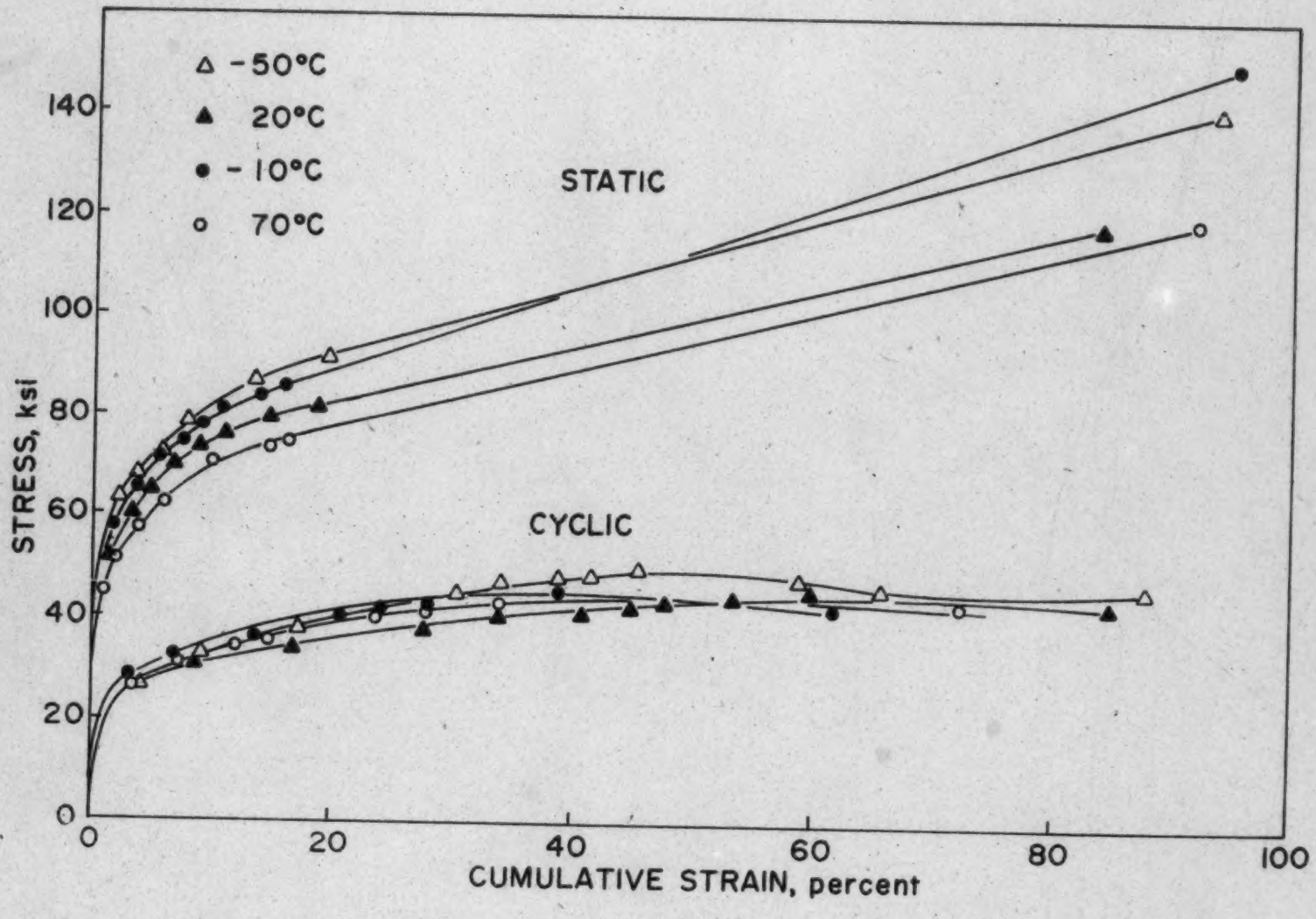

Figure 15. Static and cyclic stress-strain curves at the four test temperatures.

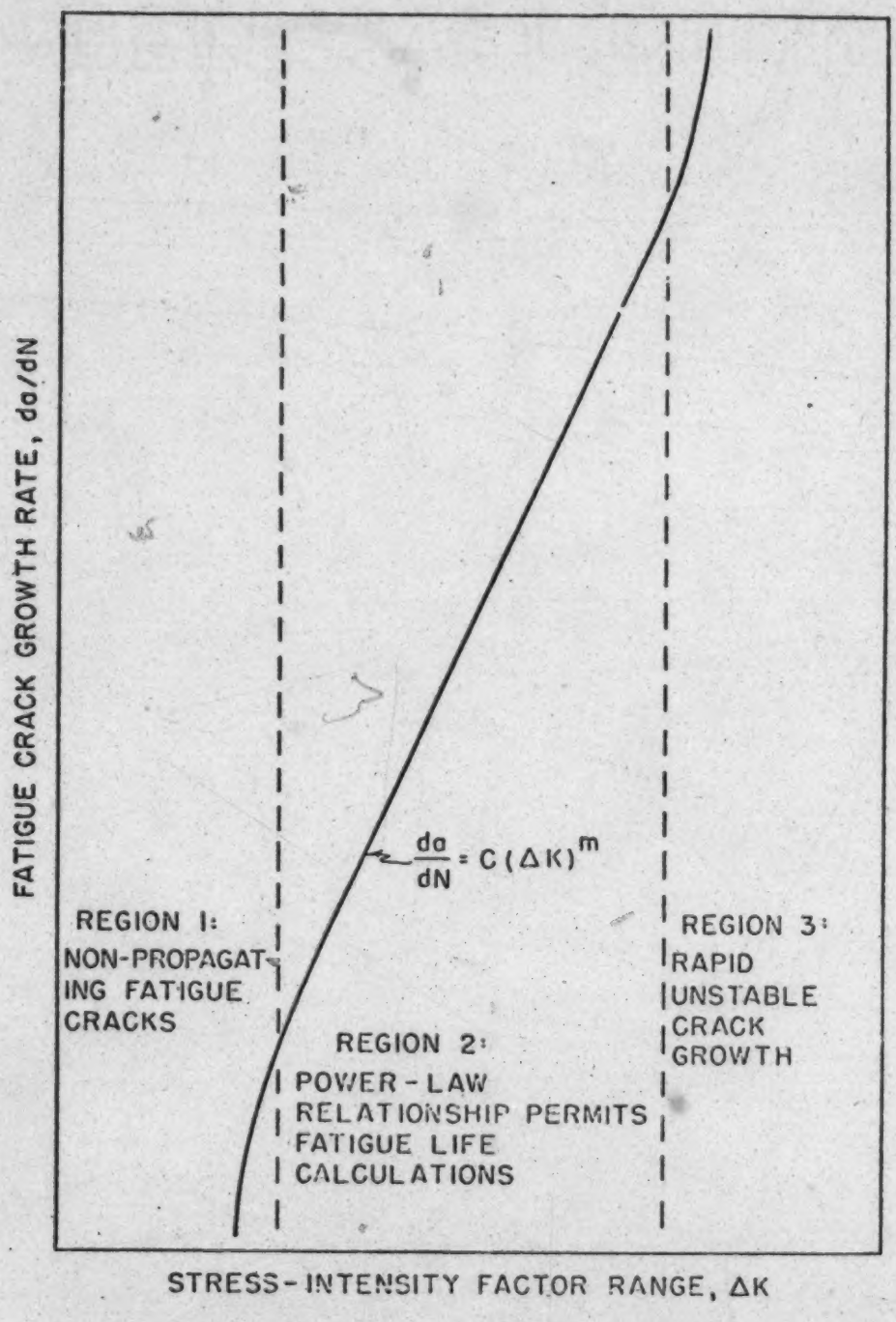

Figure 16. Schematic drawing of the crack growth rate versus the stress intensity range which illustrates the sigmoidal shape (5).

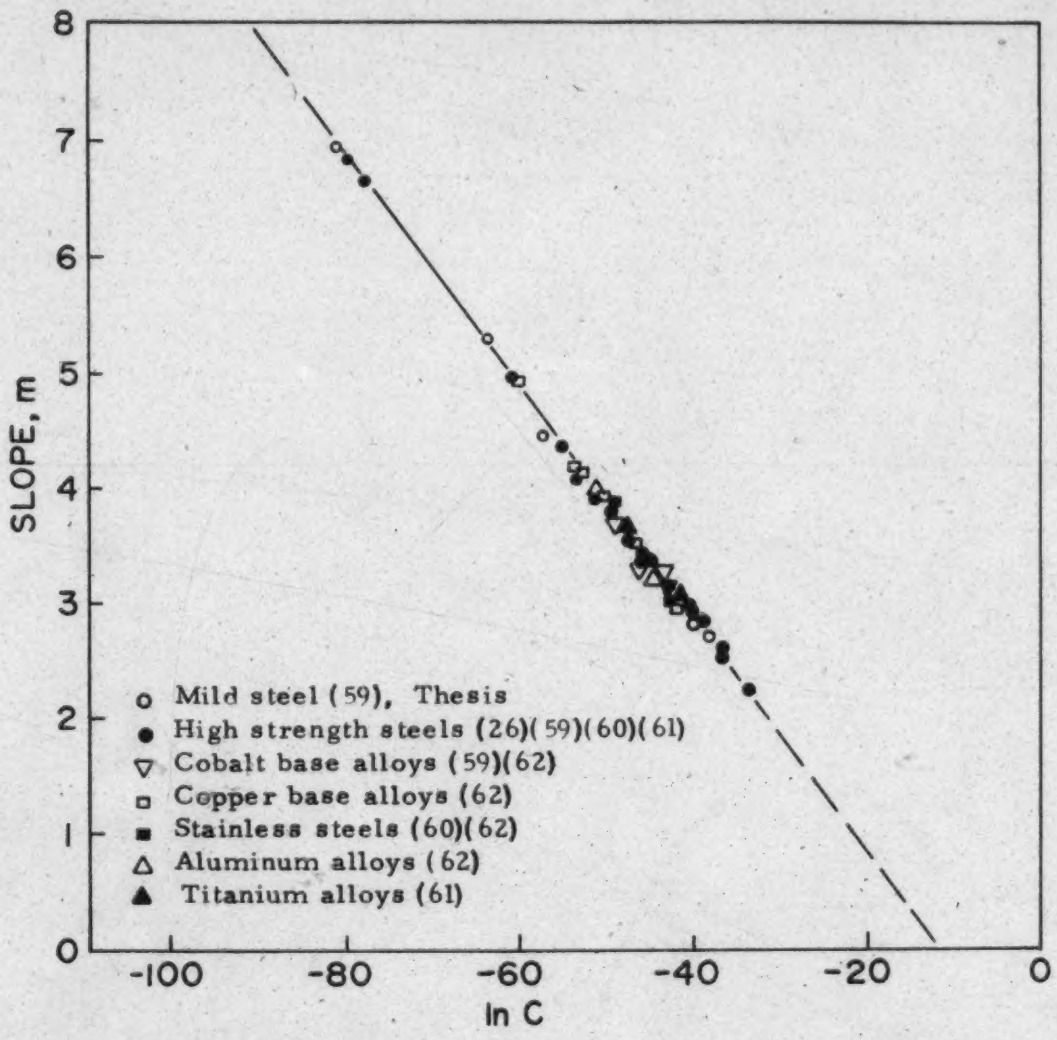

Figure 17. Slope m versus ln C for a wide range of materials and testing conditions according to equation (4).

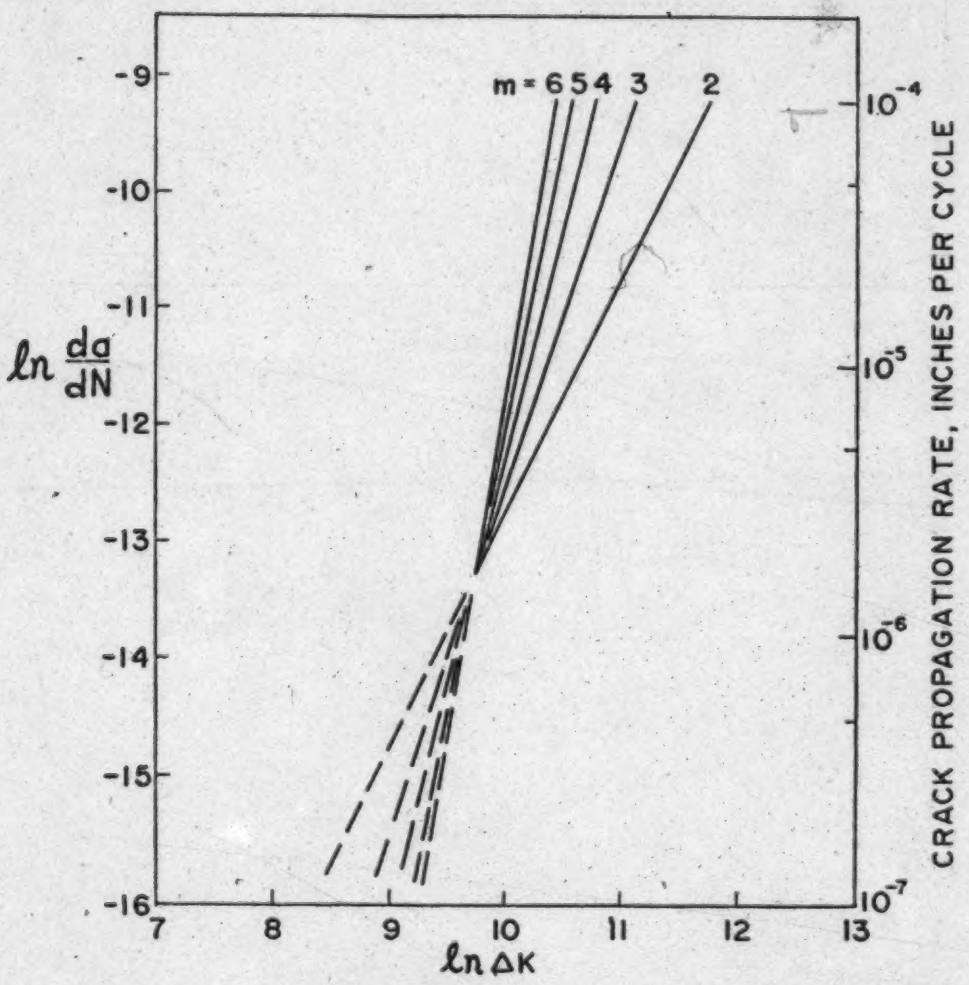

Figure 18. Predicted relationship between ln(da/dN) and lnΔK as calculated from the relationship between ln C and m shown in Figure 17.

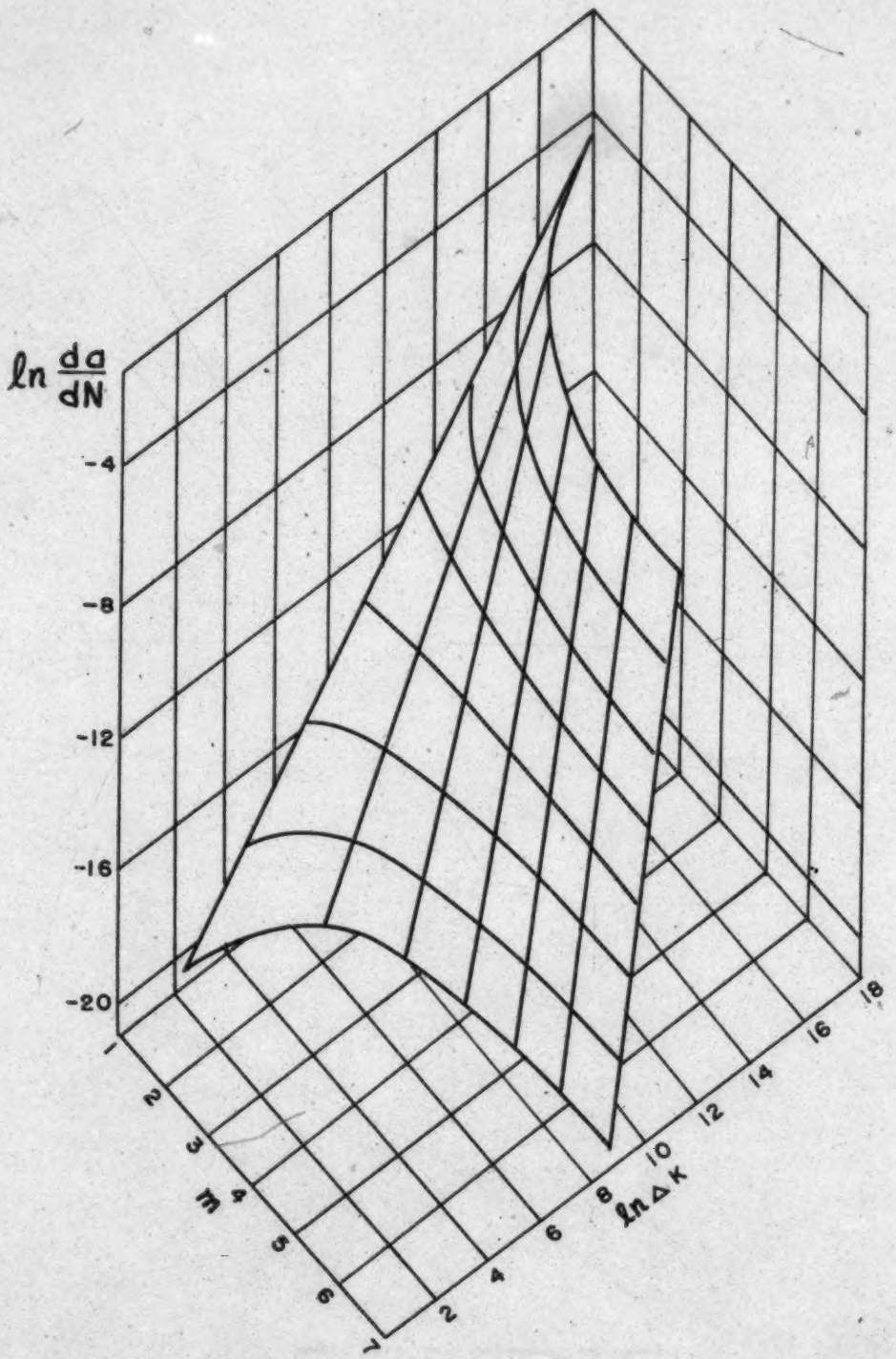

Figure 19. Relationship between ln(da/dN), ln ΔK, and m shown as a surface.

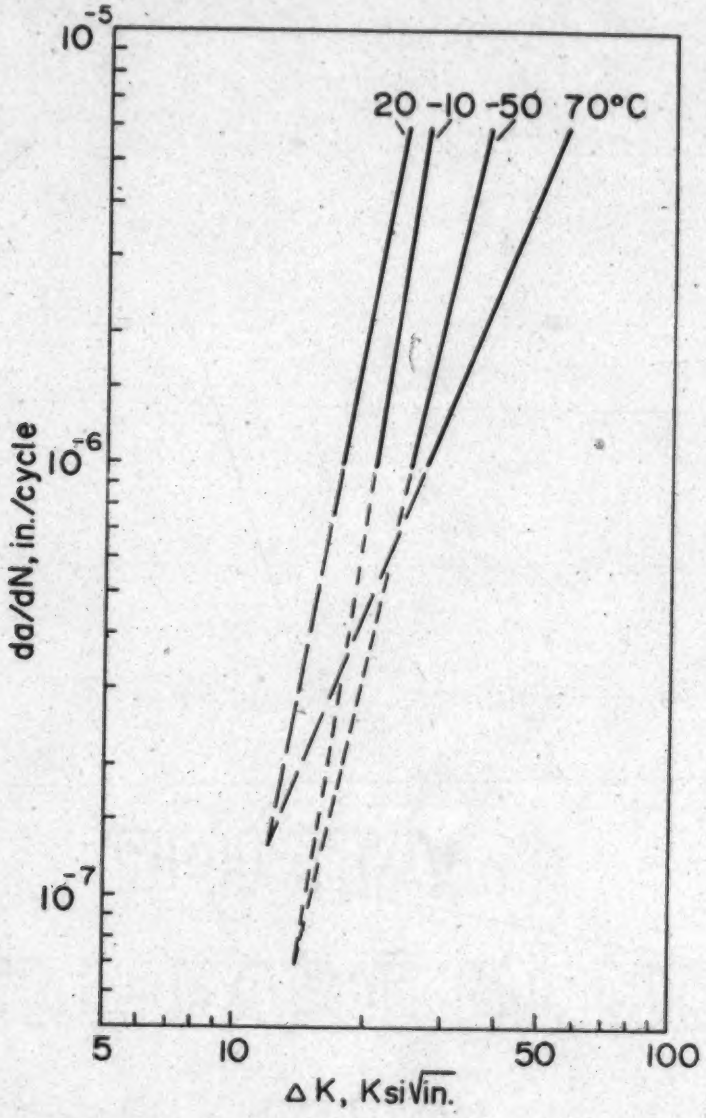

Figure 20. Mean crack propagation rate as a function of ΔK as found in this research for the four test temperatures.

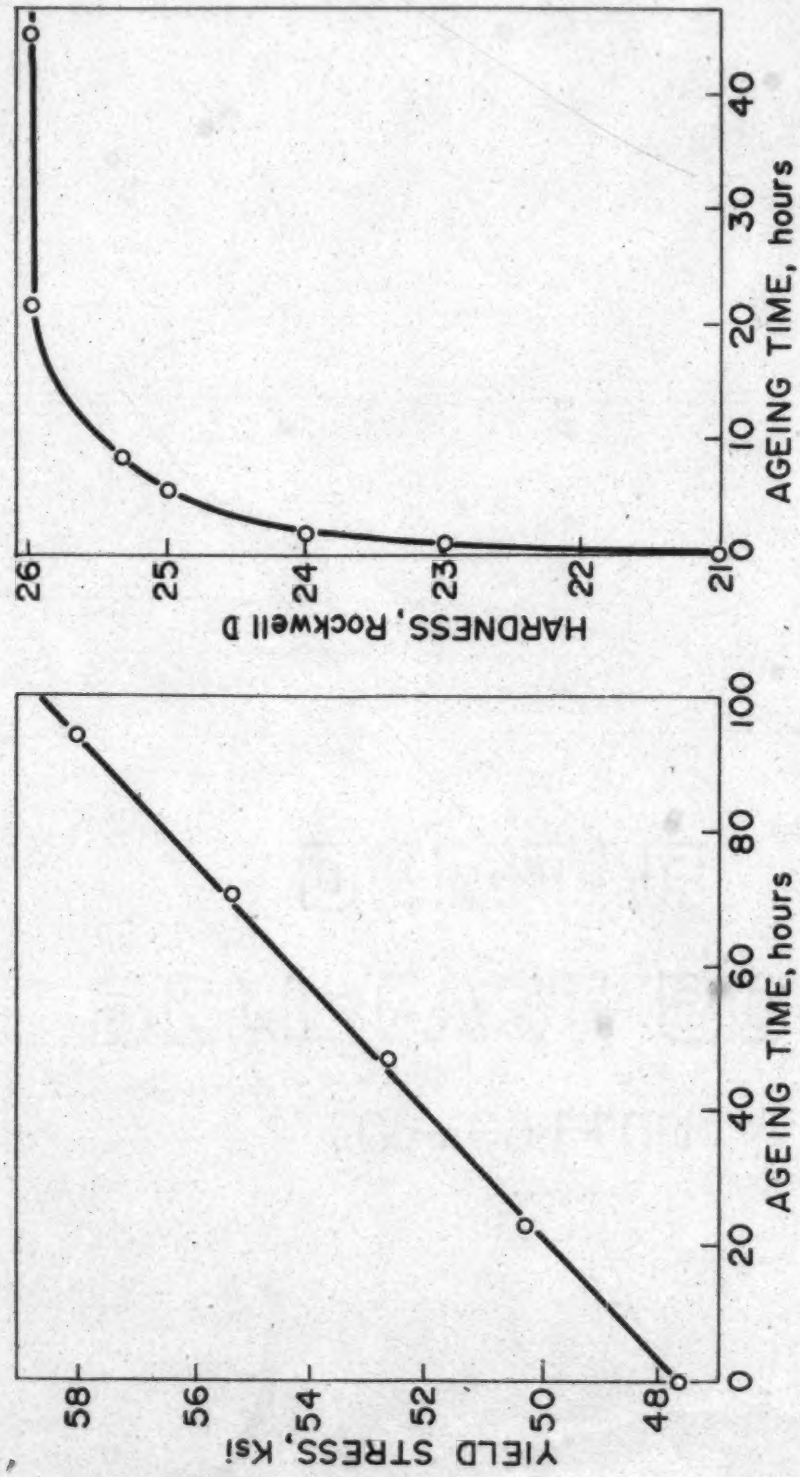

Figure 21. Effect of ageing time at room temperature after straining on the yield stress and hardness.

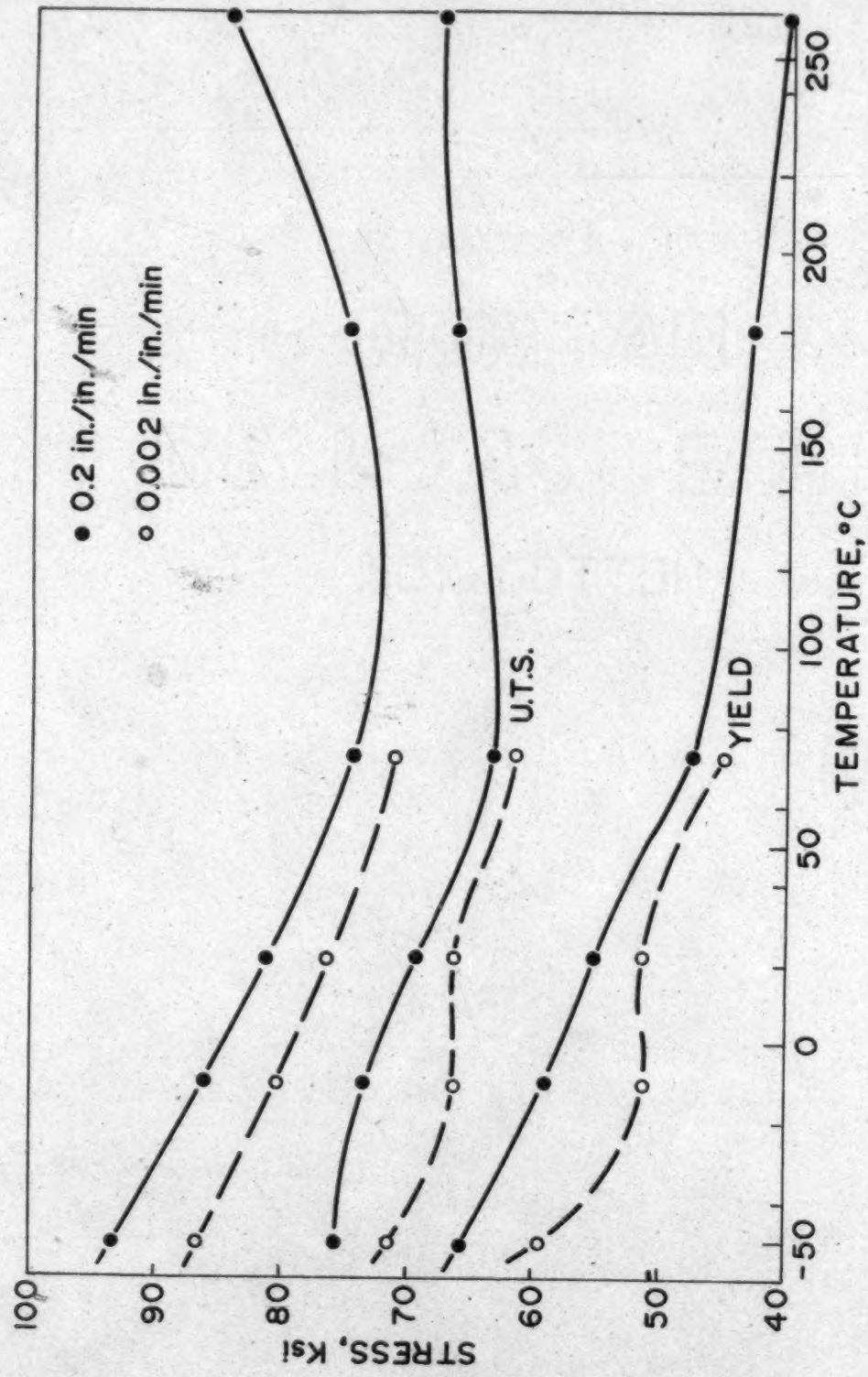

Figure 22. Effect of strain rate on the yield strength, ultimate tensile strength, and true stress at maximum load as a function of test temperature.

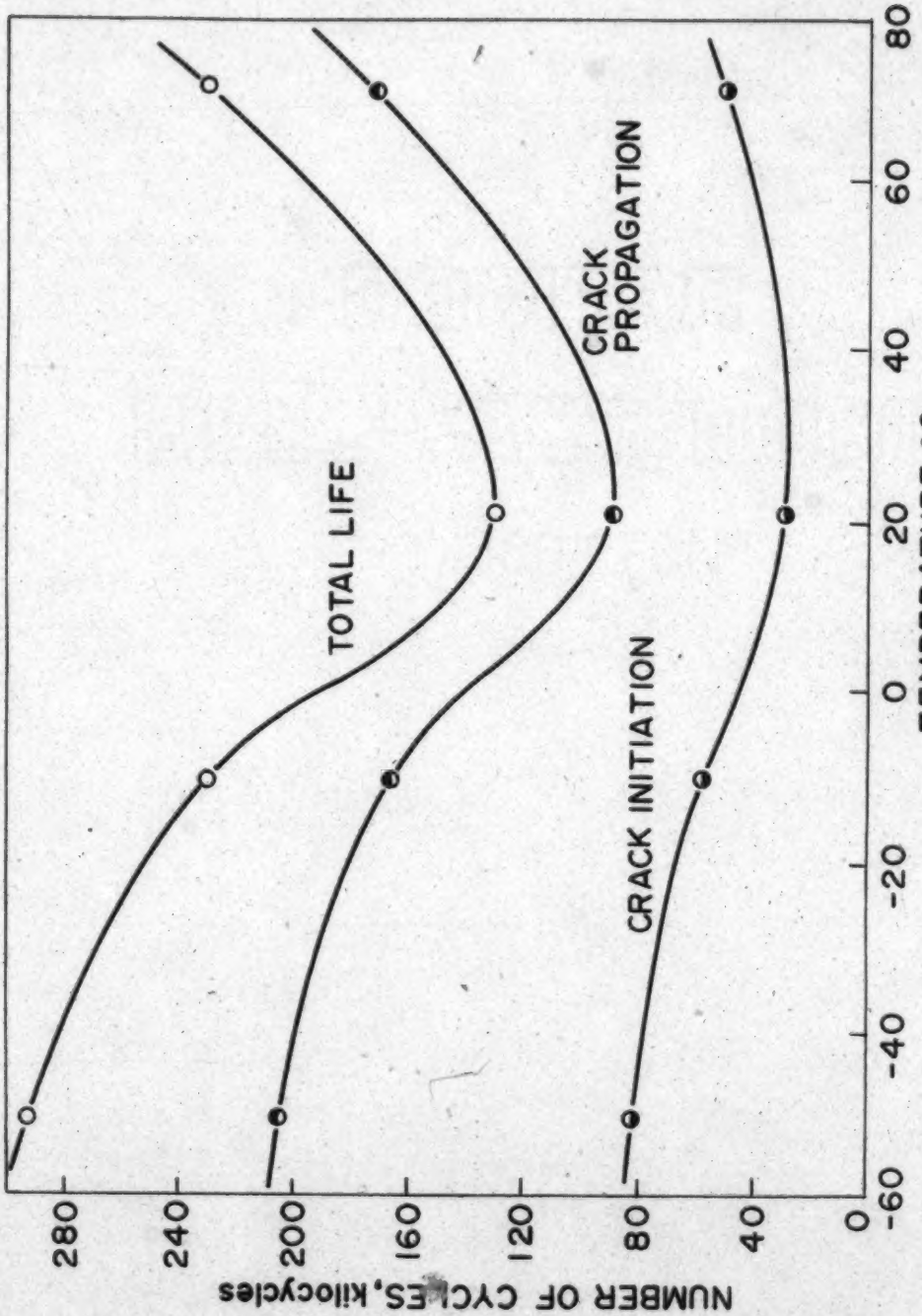

Figure 23. Variation of average fatigue life, crack propagation life, and crack initiation life as a function of temperature for tests in argon.

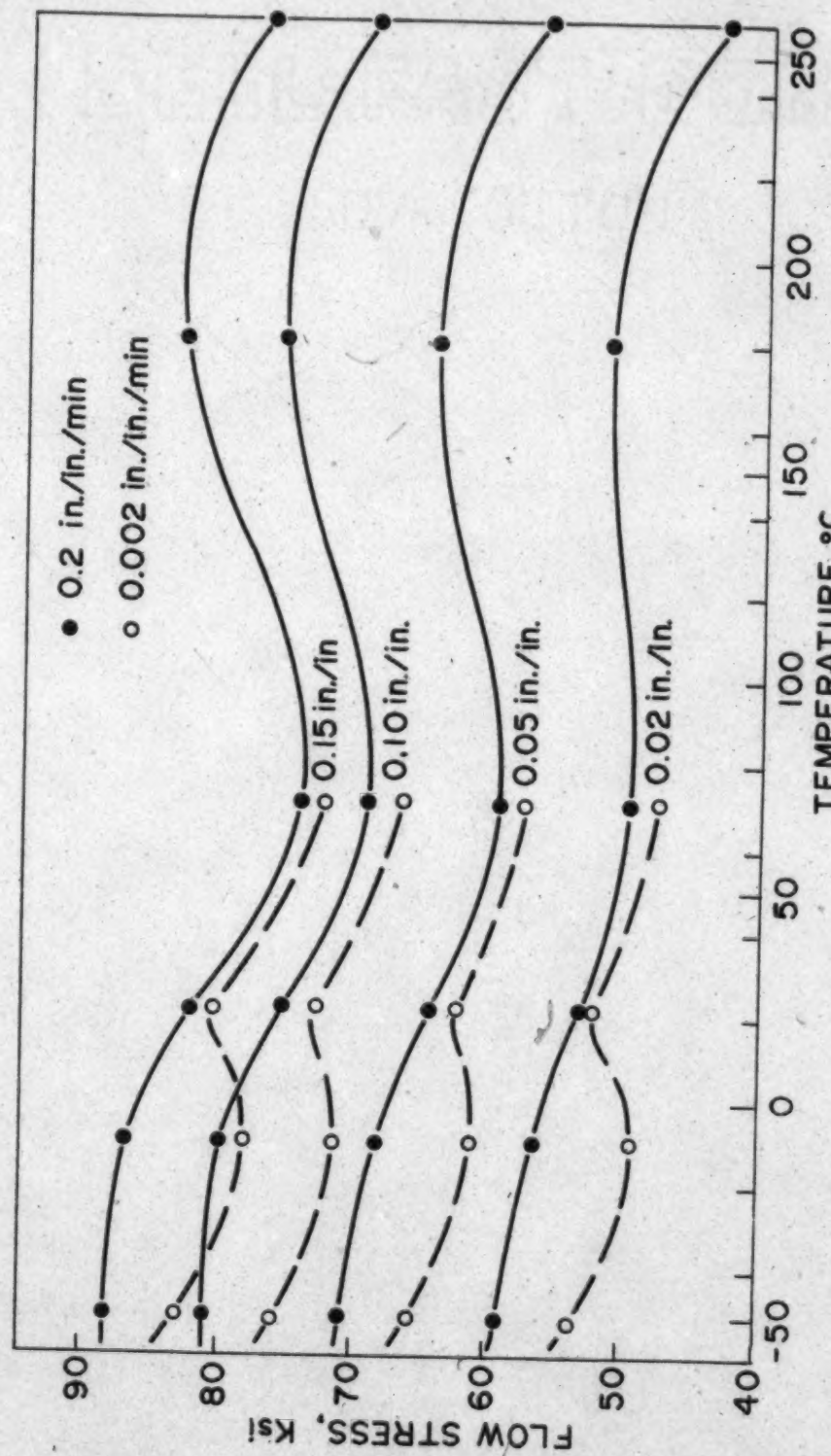

Fatigue 24. Variation in flow stress as a function of strain rate, strain and test temperature.

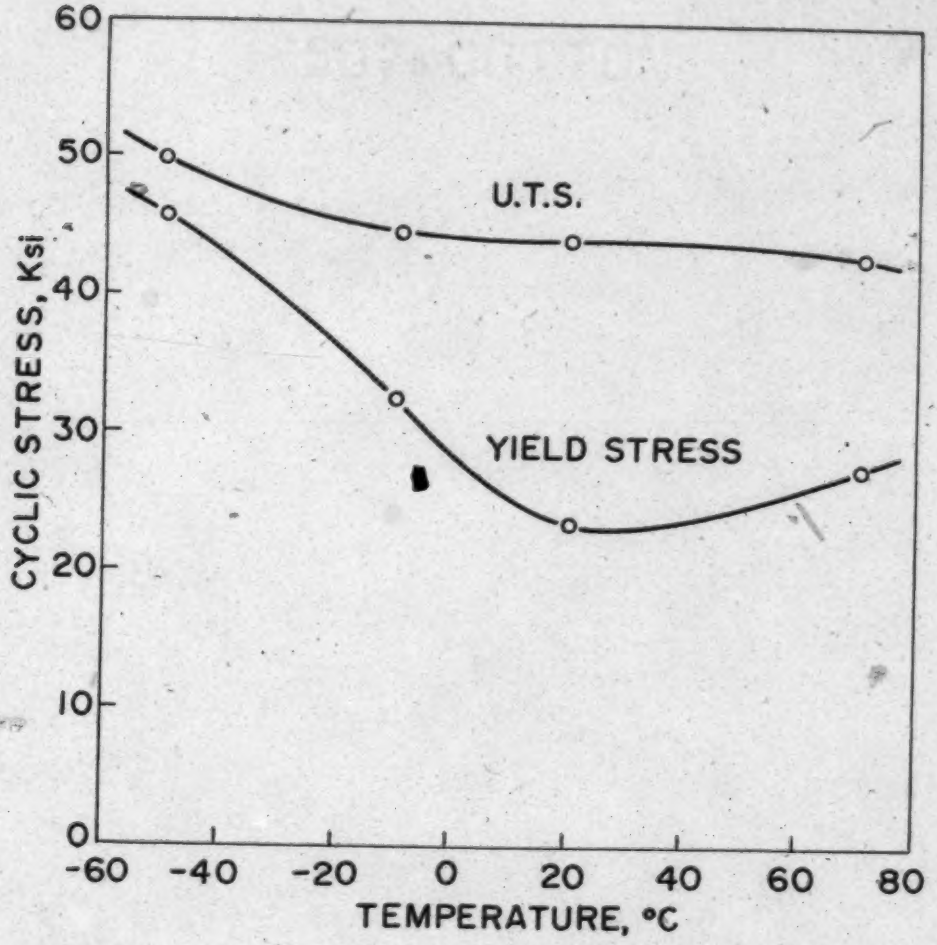

Figure 25. Variation of the cyclic yield stress and the cyclic ultimate tensile stress as a function of temperature.

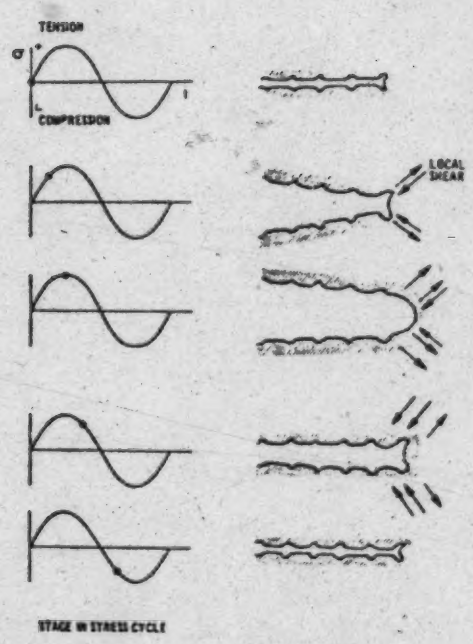

Figure 26. Schematic illustration of the plastic blunting model for fatigue crack growth (38).

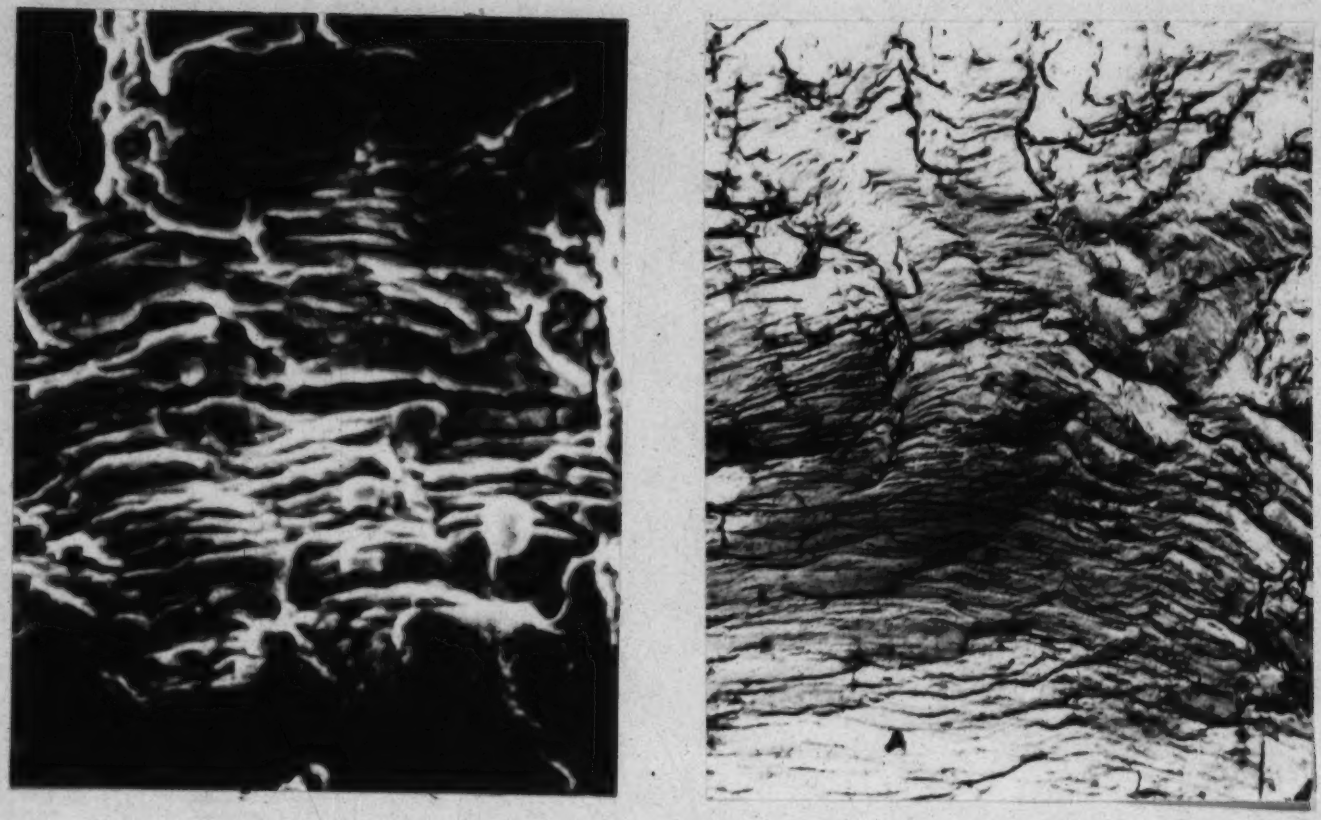

Scanning electron micrograph (X12500)

Transmission electron micrograph (X9200)

Figure 27. Fractographs illustrating fatigue striations for tests at 21°C in argon.

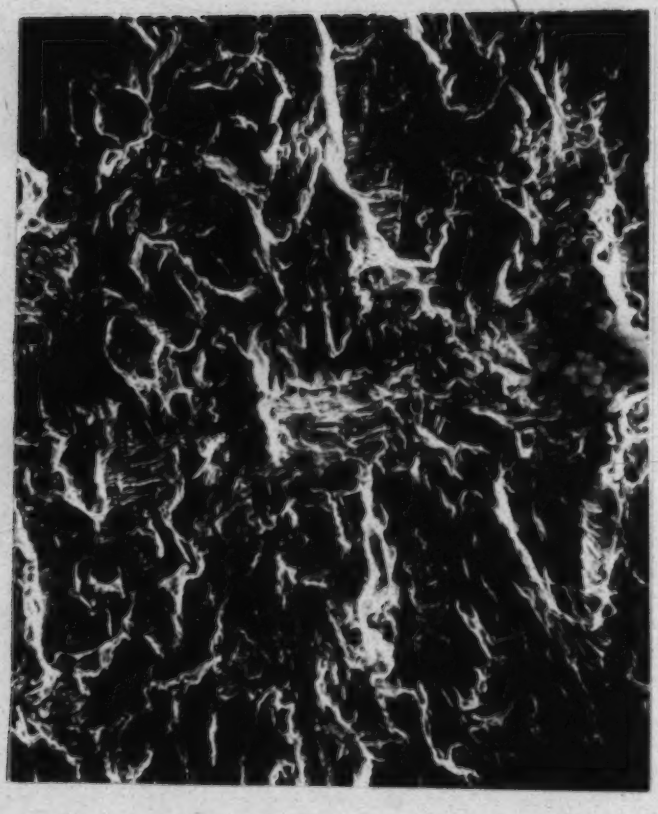

Figure 28. Scanning electron micrograph for a fatigue test at 21 °C in argon showing the localized patches of fatigue striations.

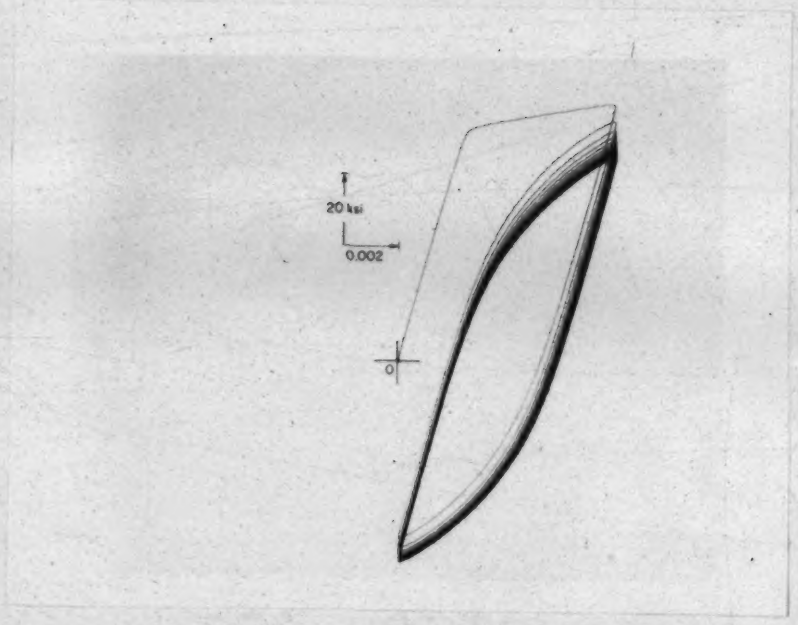

Figure 29. Cycle-dependent stress relaxation of a specimen initiatially subjected to a mean tensile stress(63).

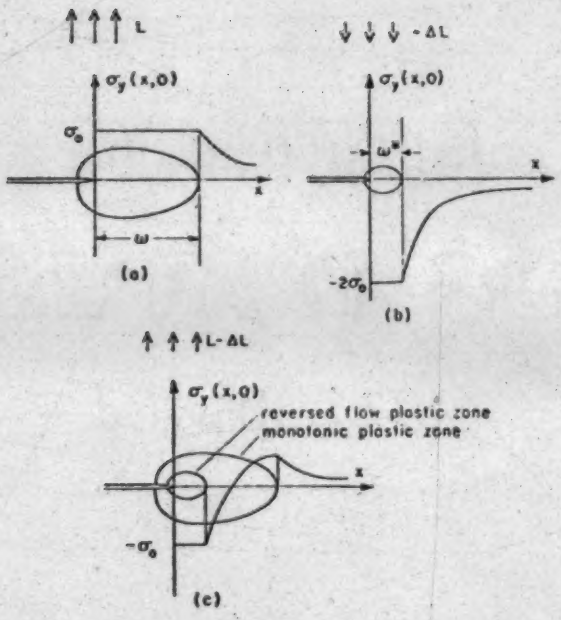

Figure 30. Schematic illustration of the stress at the crack tip showing the reversed and monotonic plastic zones (39).

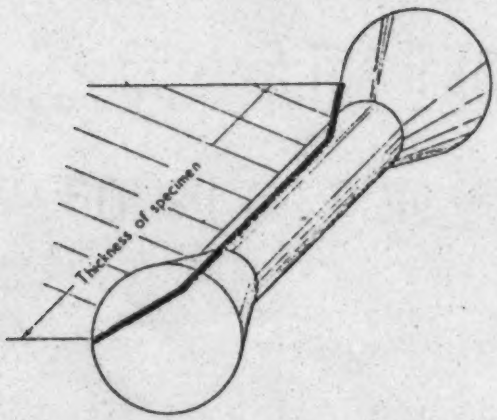

Figure 31. Effect of the state of stress on the shape of the fatigue crack front. Transition from plane stress at the surface to plane strain in the center of the specimen.

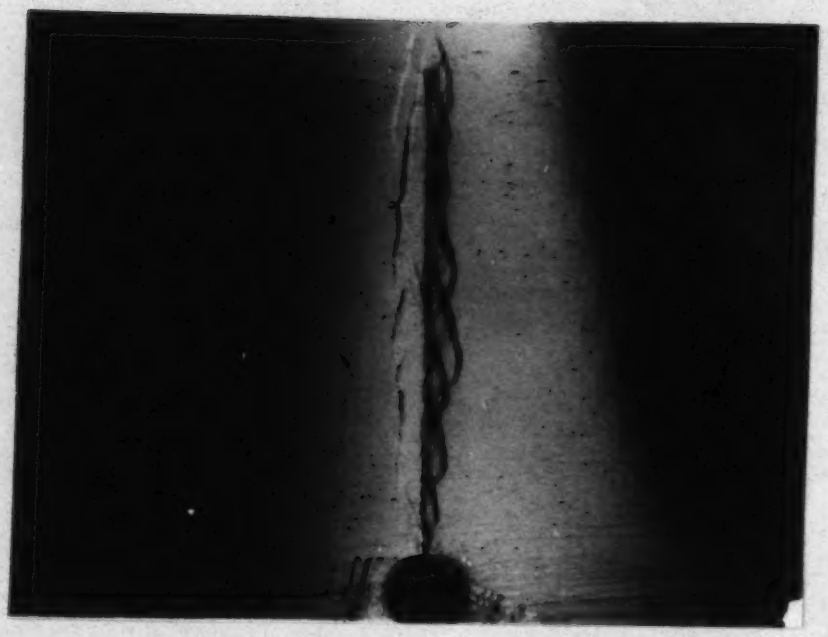

Figure 32. Surface plastic zone showing the progressive formation of Luders bands as the crack propagates.

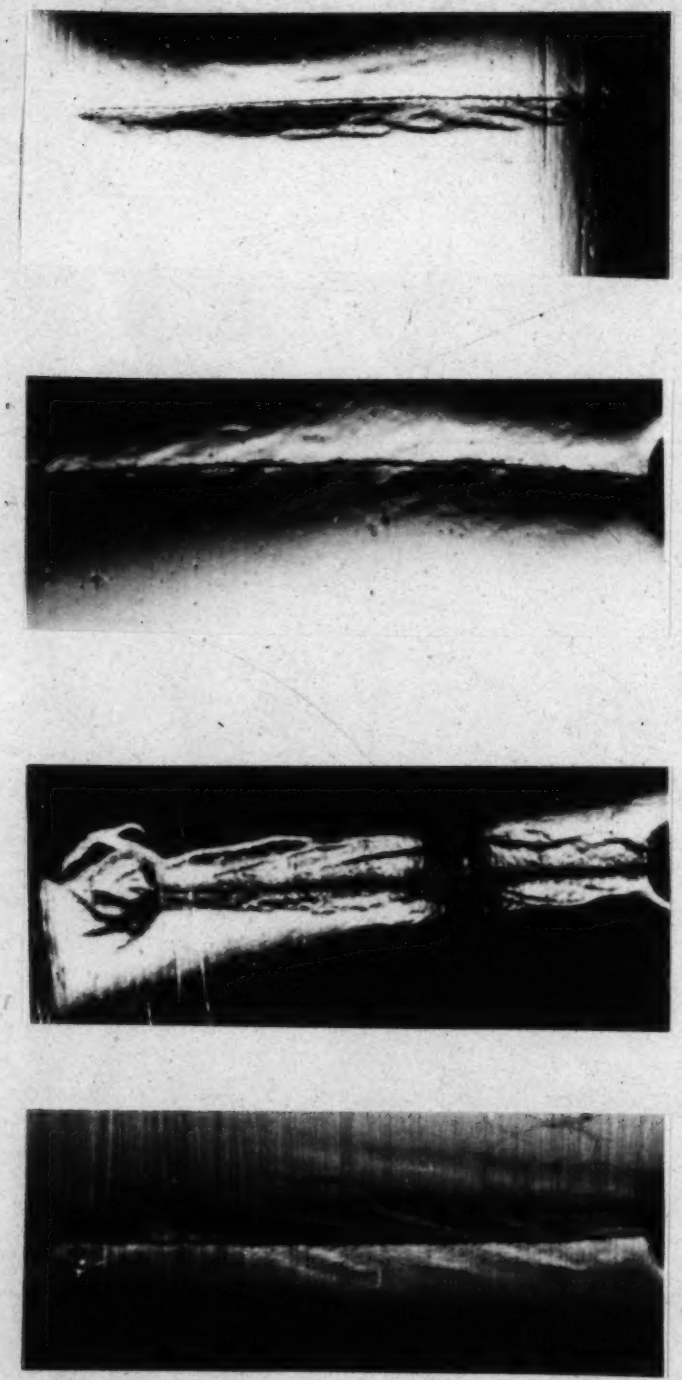

Figure 33. Photographs of the surface plastic zones at the four test temperatures.

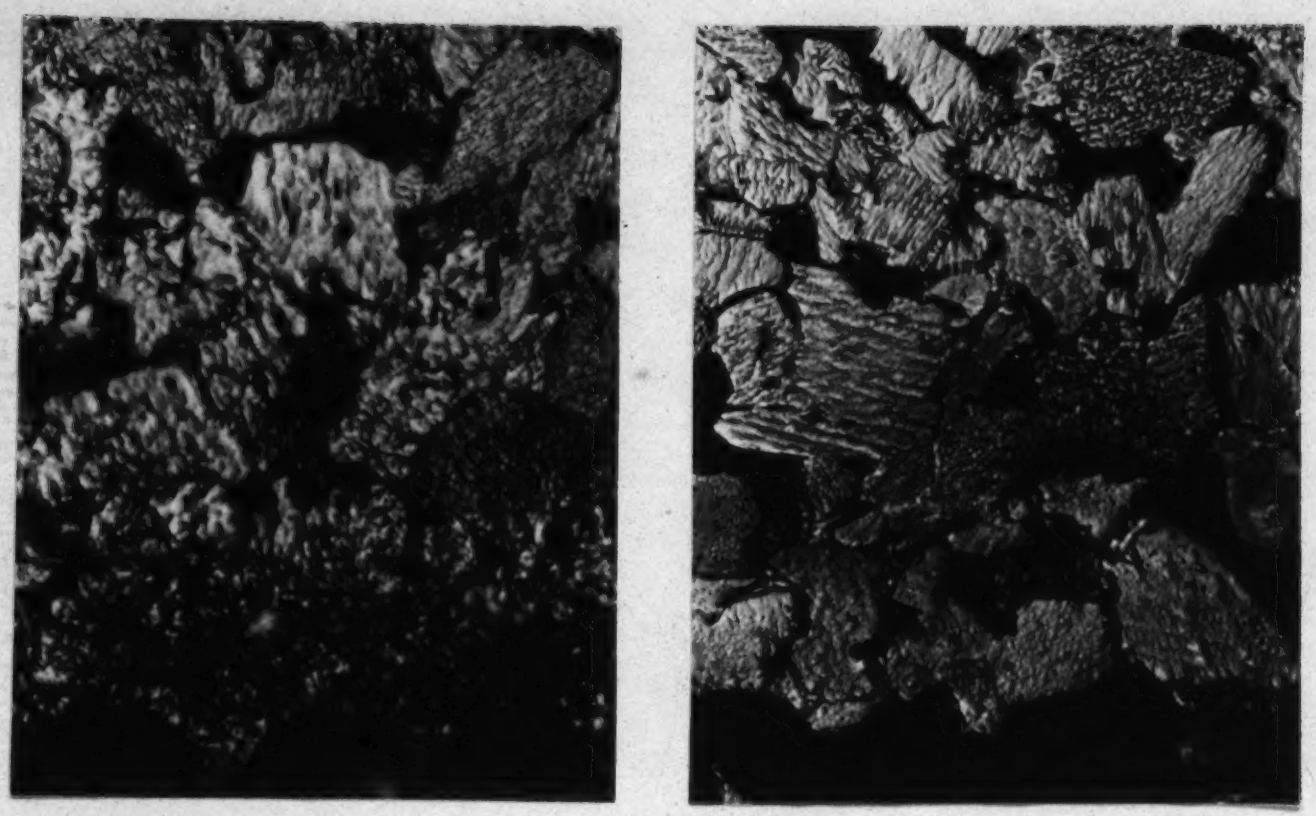

21° C, argon

21 °C, hydrogen

Figure 34. Reversed plastic zones as revealed by etching of the dense substructure in the plastically deformed region (X1000).

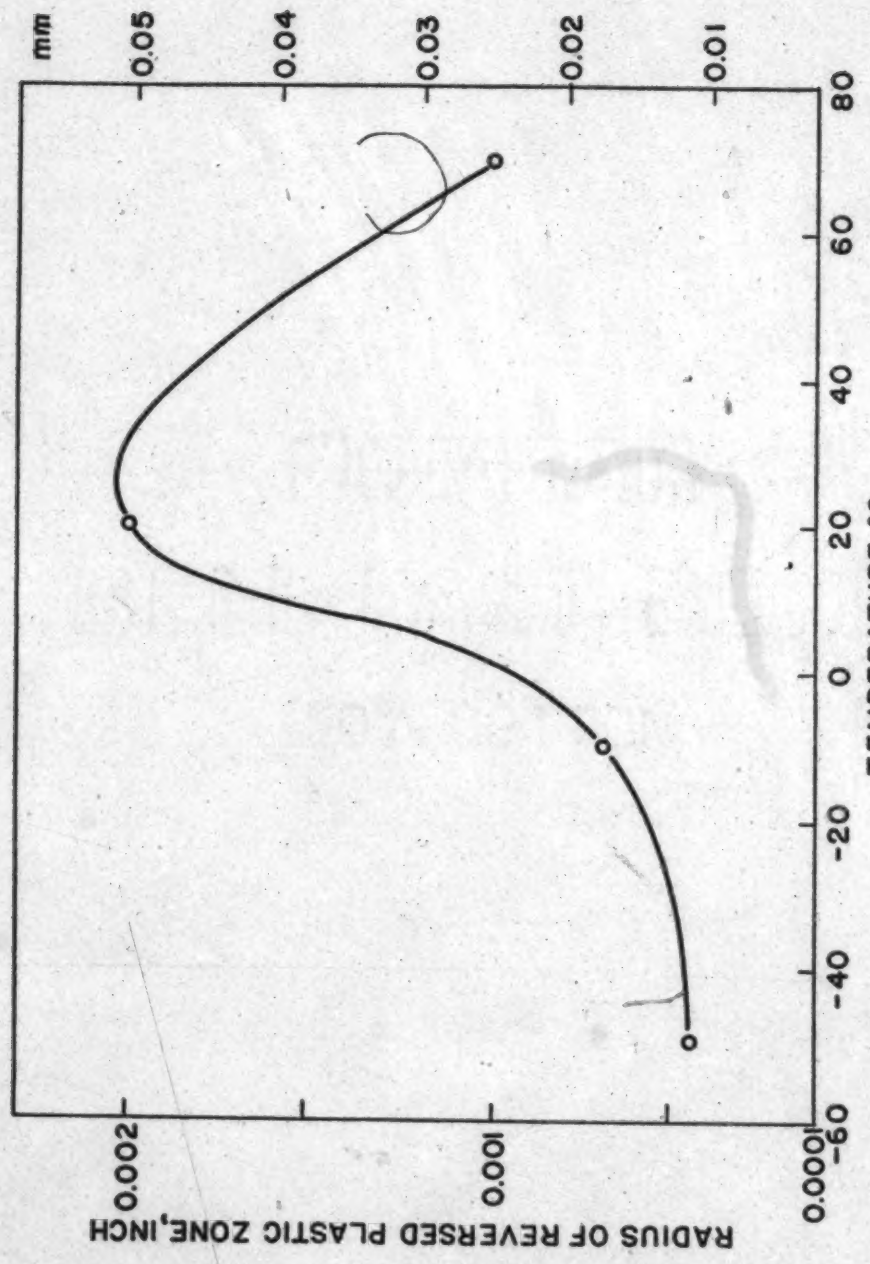

Figure 35. Radius of the reversed plastic zone as a function of temperature for tests in argon.

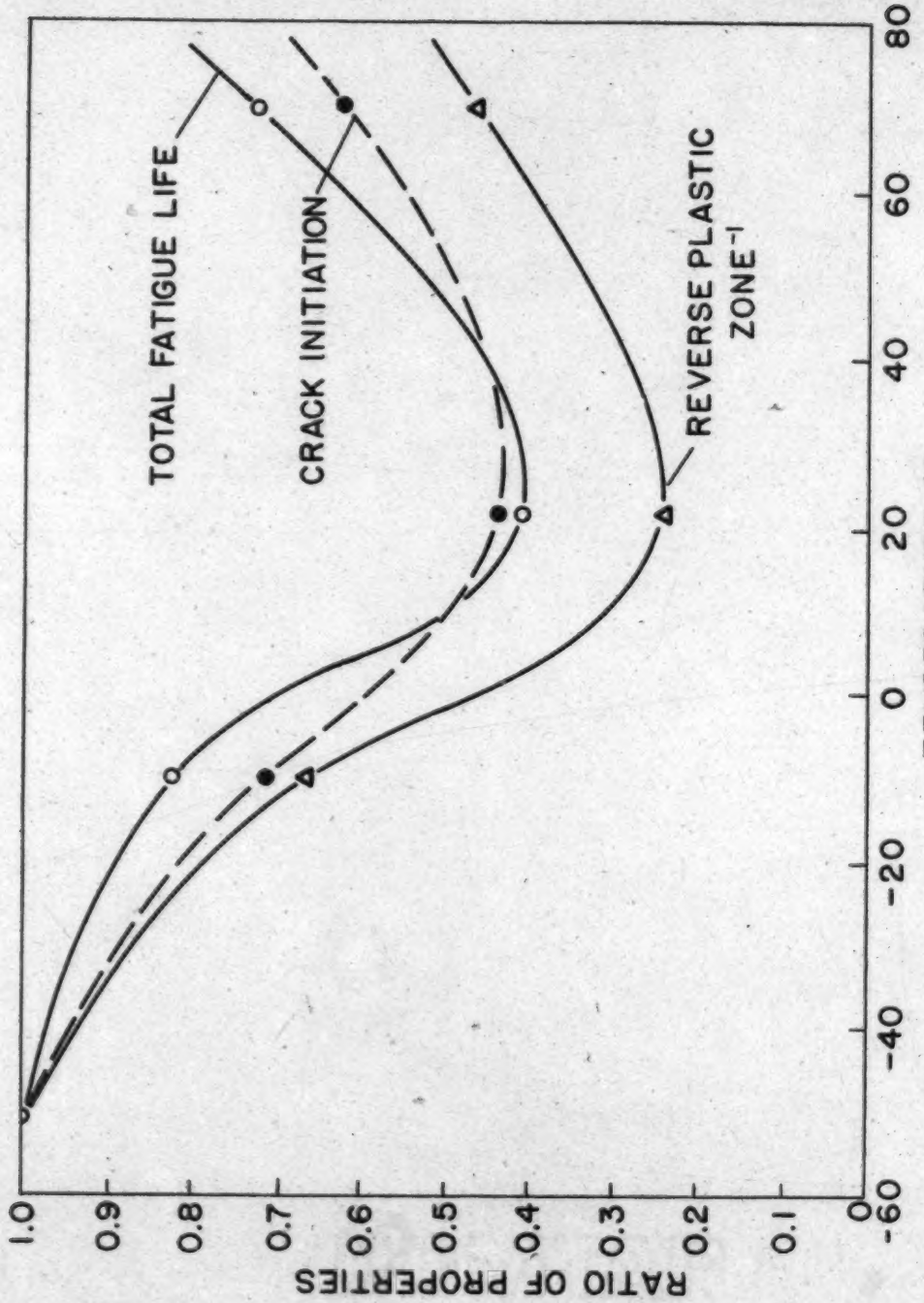

Figure 36. Crack initiation life, total life, and the inverse of the reversed plastic zone radius as a function of temperature for tests in argon.

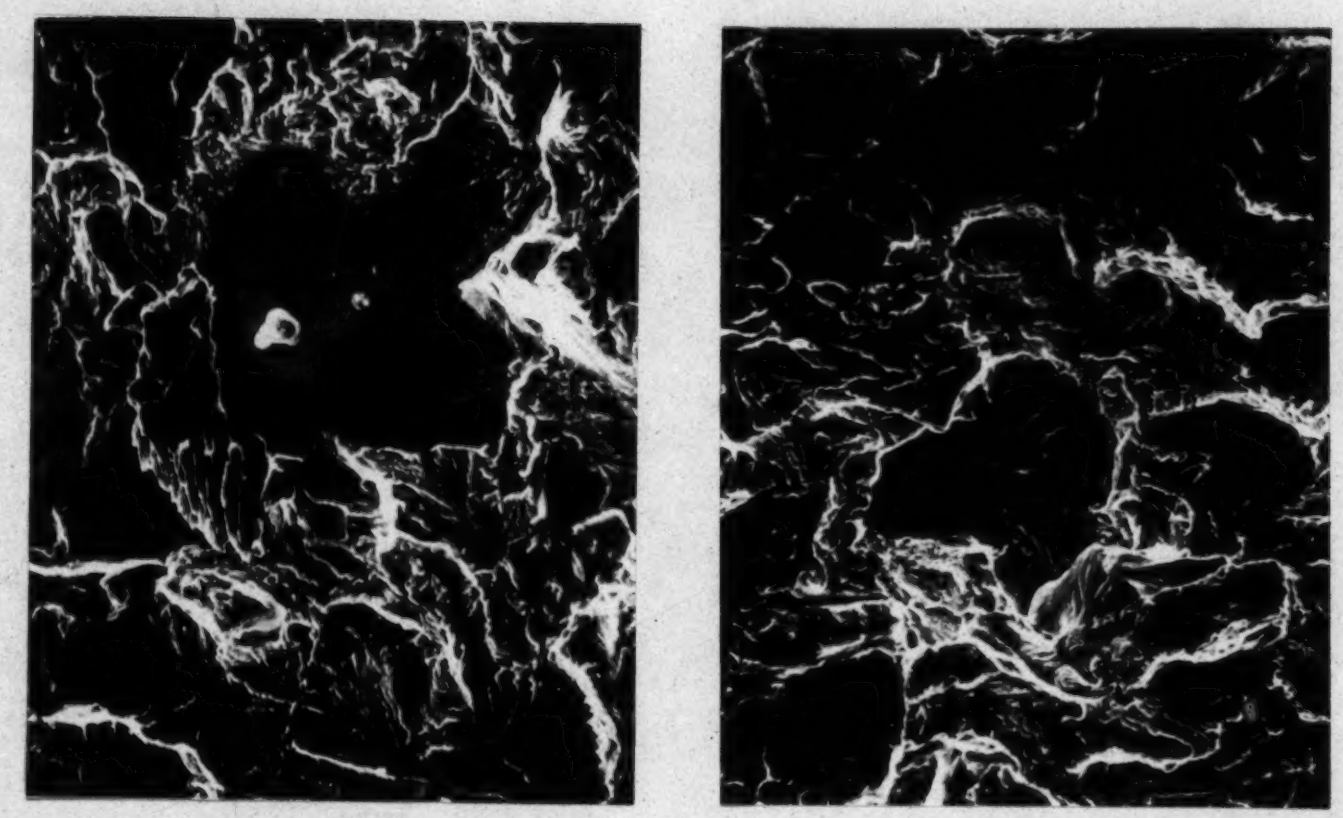

-50 °C 21 °C

Figure 37. Scanning electron microscope fractographs of fatigue specimens tested in hydrogen (X2500).

argon used until the crack started . hydrogen used throughout the test

Figure 38. Surface plastic zones of specimens fatigued in argon and hydrogen.

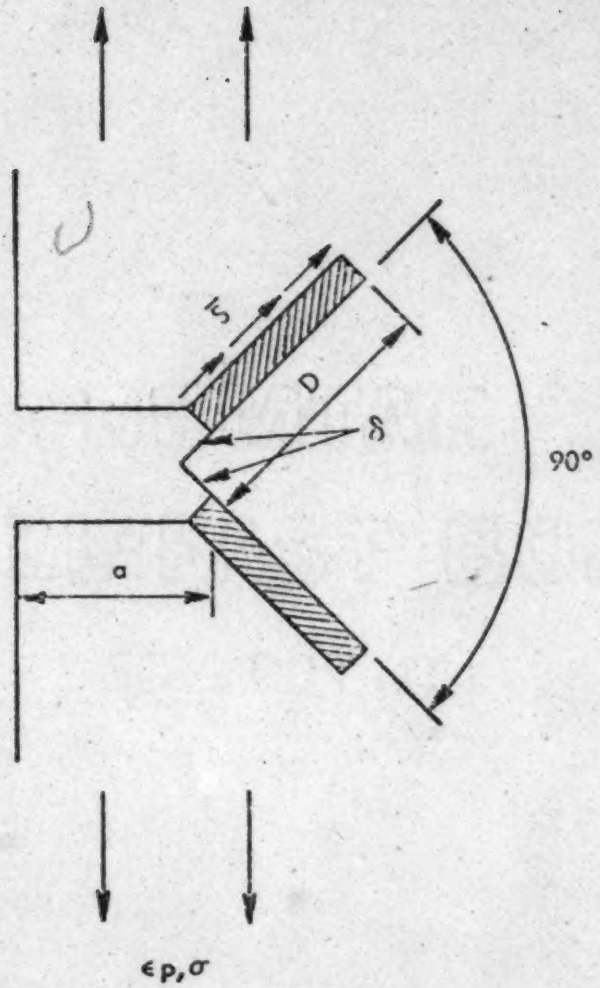

Figure 39. Model of fatigue crack advance due to shear on 45° stress planes (54).

Crack length = 4/64"
(1. 78 mm)

Crack length = 8/64"
(3. 56 mm)

Crack length = 16/64"
(5. 34 mm)

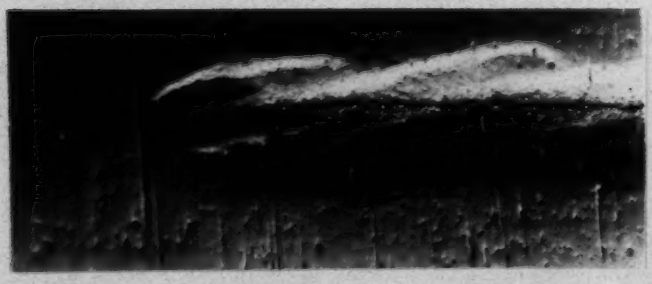

Crack length = 23/64"
(10. 23 mm)

Figure 40. Surface plastic zones for increasing crack length at 21 °C in argon.

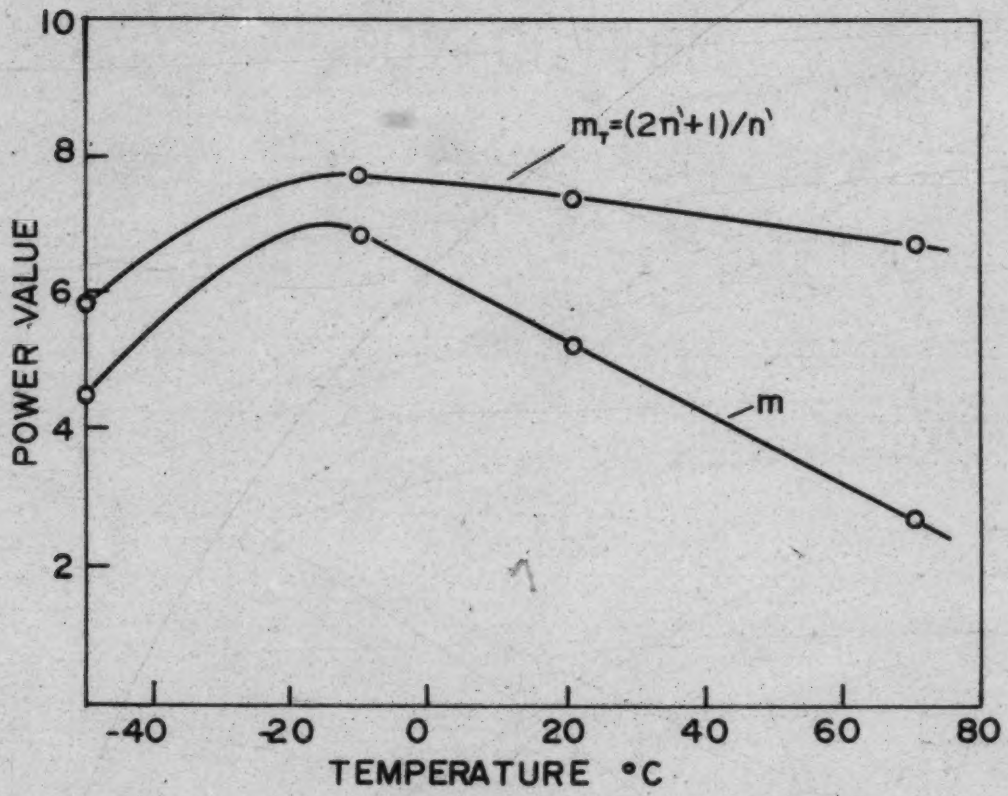

Figure 41. Power values m and m_t, a function of test temperature.

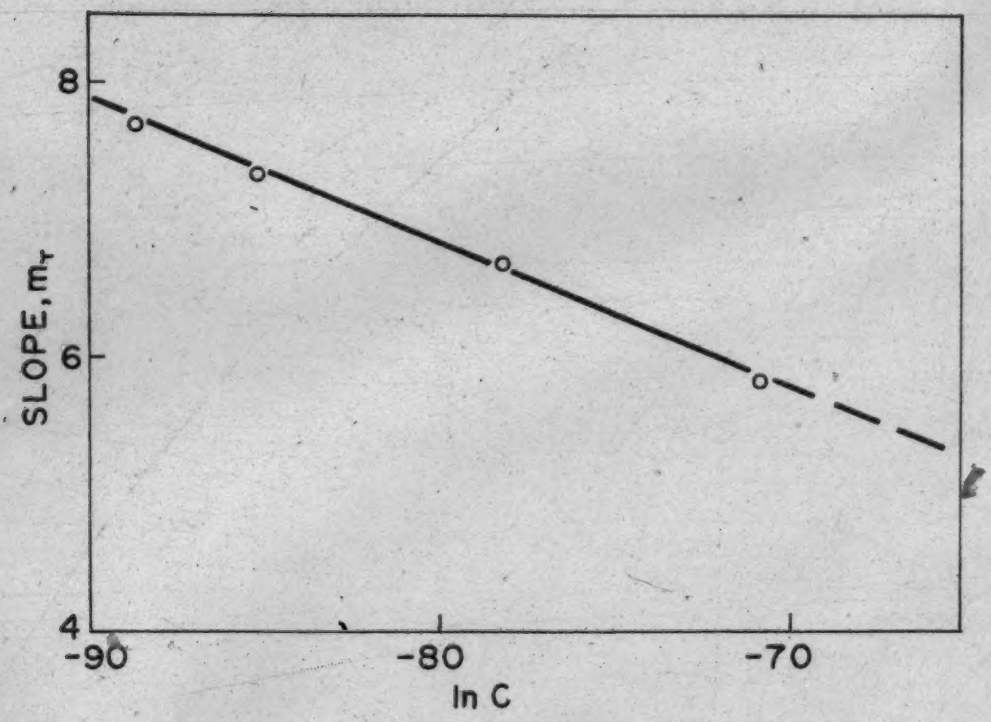

Figure 42. Slope m_t versus ln C^1 which illustrates the linear relationship as shown previously in Figure 17 for m versus ln C.

REFERENCES

1. "High Strength, Low Alloy Steels", Metals and Materials, Vol. 6, No. 12, Dec. 1972.

2. McCutcheon, D. B., Jamieson, R. M., "Low Temperature Thermal-Mechanical Treatment of Low Carbon Steels, C. I. M. Conf. of Metallurgist, Nova Scotia, 1972.

3. Metals Progress, "Technology Forecast '73", American Society for Metals, Jan. 1973.

4. Metals Progress, "Technology Forecast '72", American Society for Metals, Jan. 1972.

5. Crooker, T. W., "Basic Concepts for Design Against Structural Failure by Fatigue Crack Propagation", N. R. L. Preliminary Report 7347.

6. Gertsman, S. L., Thurston, R. C. A., "Metals and Alloys for Arctic Use", Dept. of Energy Mines and Resources, Physical Metallurgy Division, Report # PM-M-72-10, 1972.

7. Clark, W. G., Trout, H E., "Influence of Temperature and Section Size on Fatigue Crack Growth Behaviour in Ni-Mo-V Alloy Steel", Engineering Fracture Mechanics, Vol. 2, 1970.

8. Rolfe, S. T., Munse, W. H., "Fatigue Crack Propagation in Notched Steel Plates," Welding Research Supplement, June, 1963.

9. American Society for Testing Materials, Part 1, Ferrous Metals, pp. 1645, 1955.

10. Kettunen and Kocks, "Fatigue Hardening and Fatigue Life", Acta Met., Vol 20, Jan. 1972.

11. Kies, J. A., Smith, H. L., Romine, H. E., Bernstein, H., "Fracture Testing of Weldments", A. S. T. M., S. T. P 381, Fracture Toughness Testing, 1965.

12. Meyn, D. A., "Observations on Micromechanisms of Fatigue Crack Propagation in 2024 Aluminum", Trans. of A. S. M., Vol. 61, No. 1, 1968.

13. Wilson, W.K., "Stress Intensity Factors for Deep Cracks in Bending and Compact Tension Specimens", Engineering Fracture Mechanics, 1970, Vol. 2.

14. 1971 Annual Book of ASTM Standards, Part 31, pp. 919.

15. Paris, P., Erodogan, F., Journal of Basic Engineering, Vol. 85, 1963, pp. 528.

16. Paris, P., "The Fracture Mechanics Approach to Fatigue", Fatigue an Interdisciplinary Approach, Sagamor Army Materials Research Conference 10, 1963.

17. Head, A.K., Phil. Mag. 44, 1953, pp. 925.

18. Frost, N.E., Dugdale, D.S., J. Mech. Phys. Solids, 6, 1958, pp. 92.

19. McEvily, A., Illg, W., NACA, IN4394, Sept. 1958.

20. Weibull, W., Acta. Met. 11, 1963, pp. 745.

21. Liu, H.W., Applied Mat. Research, 3, 1964, pp. 229.

22. Liu, H.W., Journal of Basic Engineering, Trans. of A.S.M.E. 83, 1961, pp. 23.

23. Liu, H.W., Journal of Basic Engineering, Trans. of A.S.M.E. 85, 1963, pp. 116.

24. Donahue, R.J., Clark, H., Atanmo, P., Krumble, R., McEvily, A.J., "Crack Opening Displacement and the Rate of Fatigue Crack Growth", Int. Jour. of Fract. Mech., Vol. 8, No. 2, 1972.

25. Anctil, Kula, A.S.T.M., S.T.P. 462, 1970, pp. 297.

26. Miller, G.A., "The Dependence of Fatigue Crack Growth Rate on the Stress Intensity Factor and Mechanical Properties of High Strength Steels", Trans. of A.S.M., Vol 61, 1968.

27. Manson, S., Hirschberg, M.H., NASA, TN3146, 1967.

28. Pelloux, R., "Ultra-Fine Grain Size Metals", 16th Sagamore Conf., Syracuse University, 1969.

29. Wilson, D. V., Phil. Mag. 1970, 21, pp. 643.

30. Klesnil, M., Lukas, P., Jour. Iron and Steel Inst., 205, 1967, pp. 746.

31. Forrest, P. G., "Speed Effects in Fatigue", Proc. of the Royal Society, A 242, 1957.

32. Levy, J. C., Sinclair, G. M., "An Investigation of Strain Ageing in Fatigue", A. S. T. M. Proceedings, Vol. 55, 1955, pp. 866.

33. Achter, M. R., "Effect of Environment on Fatigue Cracks", Fatigue Crack Propagation, A. S. T. M., S. T. P. 415, 1967.

34. Paxton, H. W., "Precipitation Reactions in Irons and Low Alloy Steels", Precipitation from Solid Solution, A. S. M. Publ. 1959, Cleveland, Ohio.

35. Hundy, B. B., "The Strain-Age Hardening of Mild Steel", Metallurgia, Vol. 53, No. 315, 1956.

36. Pugh, H., et al., "Tensile Properties of High Purity Iron From -196 °C to 200 °C at Two Rates of Strain", Phil. Mag., 1963, 8, 753.

37. Forsyth, P. J. E., "The Physical Basis of Metal Fatigue", American Elsevier Publ. Co. Inc., New York, 1969.

38. Laird, C., "The Influence of Metallurgical Structure on the Mechanisms of Fatigue Crack Propagation", Fatigue Crack Propagation, A. S. T. M., S. T. P. 415, 1966.

39. Rice, J. R., "Mechanisms of Crack Tip Deformation and Extension by Fatigue", Fatigue Crack Propagation, A. S. T. M., S. T. P. 415, 1966.

40. Oates, G., Wilson, D. V., "The Effect of Dislocation Locking and Strain Ageing on the Fatigue Limit of a Low Carbon Steel", Acta. Met., Vol 12, Jan. 1964.

41. Yoshikawa, A., Sugeno, I., "Factors Responsible for the Sharp Fatigue Limit in Iron and Steel", Trans. of the Met. Society of AIME, Vol. 233, 1965.

42. Mintz, B., Wilson D. V., "strain Ageing During the Fatigue of Carbon Steels", Acta. Met., Vol 13, 1965.

43. Kenneford and Nichols, "The Fatigue Properties at Low Temperature of a Low Carbon and Alloy Steel", J. Iron and Steel Inst., 1960.

44. Weiss, B. Z., Meyerson, M. R., "Plastic Zone Formation and Fatigue Crack Extension During High Cycle Bending of Steels", Engineering Fracture Mechanics, Vol. 3, 1971.

45. Irwin, G. R., "Plastic Zone Near a Crack and Fracture Toughness", Proc. 7th Sagamore Ordnance Mater. Res. Conf., 1960.

46. Bernstein, I. M., "The Role of Hydrogen in the Embrittlement of Iron and Steel", U. S. Steel Corp. Res. Center, Monroeville, Pa.

47. Elsea, A. R., Fletcher, E. E., "Hydrogen Induced Delayed Brittle Failures of High Strength Steels", DMIC Report 196, 1964.

48. Williams, D. P., "Scripta Met. 2, 1968.

49. Vitovec, F. H., "Effect of Hydrogen Environment on Creep and Fracture of Steels", Proceedings of the First International Conference on Fracture, Vol. 2, 1965.

50. Jackson, J. S., "Some Issues Involved in the Corrosion Protection of Steel Springs", Coil Spring Journal, 20, 1950.

51. Beachem, C. D., "A New Model for Hydrogen Assisted Cracking (Hydrogen "Embrittlement"), Met. Trans. Vol. 3, No. 2, 1972.

52. Barnett, W. S., Troiano, A. R., "Crack Propagation in Hydrogen Induced Brittle Fracture of Steel", Trans. of American Inst, of Mining, Metallurgical and Petroleum Engineers, Vol. 209, 1957.

53. Bilby, B. A., Swinden, K. H., Proc. of Royal Soc., A285, Vol. 22, 1965.

54. Tomkins, B., "Fatigue Crack Propagation - An Analysis", Phil. Mag., Series 8, Vol 18, 1965.

55. Dugdale, D. S., J. Mech. Phys. Solids, 8, 100, 1960.

56. Freudethal, A. M., Weiner, J. H., "On the Thermal Aspects of Fatigue", Jour. of Applied Physics, Vol. 27, No. 1, 1956.

57. Williams, J. G., "The Thermal Properties of a Plastic Zone", Applied Materials Research, April, 1964.

58. Rice, J. R., Levy, N., "Local Heating by Plastic Deformation", Physics of Strength and Plasticity.

59. Barsom, J. M., "Fatigue Crack Propagation in Steels of Various Yield Strengths", Trans. of ASME, Vol. 93, Series 3, No. 4, 1971.

60 Brothers, Yukowa, "Fatigue Crack Propagation in Low Alloy Heat Treated Steels", Trans. of ASME, Journal of Basic Engineering, Vol. 89, Series D, No. 1, March, 1967.

61 Crooker, T. W., "Effect of Tension-Compression Cycling of Fatigue Crack Growth in High Strength Alloys, N. R. L. Report 7220, 1971.

62. Hickerson, J. P., Aertzberg, R. W., "The Role of Mechanical Properties in Low Stress Fatigue Crack Propagation", Met. Trans., Vol. 3, No. 1, Jan. 1972.

63. Landgraf, R. W., "The Resistance of Metals to Cyclic Deformation", Achievement of High Fatigue Resistance in Metals and Alloys, A. S. T. M., S. T. P. 467, 1969.

64. Brock, D., and Schijve, J., "The Influence of the Mean Stress on the Propagation of Fatigue Cracks in Aluminum Alloy Sheet", N. R. L. -TRM 2111, National Lucht-en Ruimtevaart/Aboratorium, Jan. 1963.

65. McMillan, J. C., Pelloux, R. M. N., "Fatigue Crack Propagation under Program and Random Loads", Fatigue Crack Propagation, A. S. T. M., S. T. P. 415, 1967.

66. Roberts, R., Erdogan, F., "The Effect of Mean Stress on Fatigue Crack Propagation in Plates under Extension and Bending", Trans. ASME Series D, Vol. 89, 1967.

67. Walker, K., "The Effect of Stress Ratio During Crack Propagation and Fatigue for 2024-T3 and 7075-T6 Aluminum", Effects of Environment and Complex Load History on Fatigue Life, ASTM, S. T. P. 462, 1970.

APPENDICES

APPENDIX 1

The Effect of Mean Stress on Fatigue Crack Propagation Rates.

Several researchers have explored the effect of mean stress on fatigue crack propagation rates. Brock and Schijve (64), McMillan and Pelloux (65), Roberts and Erdogan (66), and Walker (67) have proposed a general equation of the following form:

$$da/dN = C\, Kmax^{m1}\, \Delta K^{m2} \qquad (1)$$

The explicit form of equation(1)may vary by rearrangement of the variables. However, the above researchers have evaluated only data for aluminum and their final form of equation(1)indicates that m_1 is approximately equal to m_2; therefore, equation(1)can be rewritten as:

$$da/dN = C_1 (Kmax\ \Delta K)^{m3} \qquad (2)$$

For the purpose of evaluating the data from this research the general form of equation(1)is expanded in the following manner with no previous assumptions regarding the power values.

$$da/dN = C\, (\Delta K/2 + Km)^{m1}\, \Delta K^{m2} \qquad (3)$$

where $Kmax = \Delta K/2 + Km$ and $\Delta K/2$ is the stress intensity amplitude equal to Ka and Km is the mean stress intensity. ΔK is defined as Kmax - Kmin. Equation(3)becomes:

$$da/dN = C\ \ \Delta K^{m1}\ /2^{m1}\ (1 + 2Km/\Delta K)^{m1}\, \Delta K^{m2} \qquad (4)$$

which is equal to:

$$da/dN = C\ \ 1/2^{m1}\ (1 + 2Km/\Delta K)^{m1}\ \ \Delta K^{m2+m1} \qquad (5)$$

The stress ratio is defined as $A = Ka/Km$. Equation (5) then becomes:

$$da/dN = C \quad 1/2^{m1}(1 + 1/A)^{m1} \Delta K^{m2+m1} \qquad (6)$$

The data of this research were converted for the effect of mean stress, i.e. mean stress intensity factor according to the following equation:

$$da/dN = C \left[1/2^{n}(1 + 1/A)^{n} \Delta K\right]^{m} \qquad (7)$$

By taking $\log (1 + 1/A)$ versus $\log \Delta K$ for a constant crack growth rate the power value n was calculated using a regression analysis. The results for the tests in argon are as follows:

Temperature °C	n	r
-50	1.45	0.931
-10	2.17	0.997
21	0.58	0.851
71	6.80	0.971

Comparison of equation (6) and (7) give the following identity:

$$m_1 = nm$$
$$m_1 + m_2 = m$$

Thus one can write equation (8) as follows:

$$da/dN = C_2 \quad 1/2^{m1} \quad (1 + 1/A)^{m1} \Delta K^{m} \qquad (8)$$

where:

Temperature °C	m1	m
-50	6.50	4.49
-10	14.75	6.80
21	3.01	5.19
71	18.10	2.66

Given below are the modified values which consider the mean stress effect:

Temperature	ln C ave.	lnΔK ave.	m ave.	s* lnΔK	s* ln da/dN
-50°C	-58.57731	10.34455	4.495	0.07740	0.39744
-10°C	-81.50162	10.05730	6.81	0.06614	0.45907
21°C	-65.12777	10.06434	5.195	0.1443	0.60097
71°C	-41.07833	10.49487	2.66	0.15401	0.39786

Shown in Figures 12 to 14 inclusive are the crack propagation rates versus the stress intensity range for the various testing conditions. The dashed border lines represent the standard deviation of the stress intensity and the solid line represents the mean.

---

s*=the standard deviation

APPENDIX 2

Calculation of Temperature Maximum in the Reversed Plastic Zone Calculated from a Cylindrical Heating Source Embedded in a Similar Matrix

Approximate Calculation of Temperature Maximum within Reversed Plastic Zone

In this analysis, the system is approximated by a cylindrical wire embedded in a matrix of the same material. The heat is generated within the wire and dissipated into the surrounding material. The heat flux per second is calculated from hysteresis loop measurements. The volume of the reversed plastic zone, assumed to be a cylinder is then divided into the heat flux and the heat per second per unit volume is then known for each temperature studied. The amount of energy converted to heat is assumed to be proportional to the radius of the reversed plastic zone, i. e. the larger the zone the more energy converted to heat, but the heat per unit volume may be less. It is further assumed that at some distance from the center of the reversed plastic zone the temperature is at the ambient. For comparative purposes this distance is assumed to be the radius of the surface plastic zone. The temperature distribution within the reversed plastic zone is not constant but since the zone is so minute it is assumed to be at a constant temperature. The temperature is then calculated for the center of the reversed plastic zone. The values obtained show only that a temperature rise occurs. The actual localized temperature on individual slip planes may be much higher but the problem of calculating this temperature becomes extremely complex. Following

is the temperature calculations.

The solution for the temperature in this case is:

$$T = \frac{q}{4k}(Rg^2 - Rr^2) + \frac{q\,Rg^2}{2k}(\ln A\,Rg - \ln Rg) + To$$

T = maximum temperature in the reversed plastic zone.

q = heat flux cal / cm^3 sec

k = thermal conductivity cal/sec cm ^oC = .12

Rg = radius of large plastic zone (cm)

Rr = radius of reversed plastic zone (cm)

A = ratio of Rg/Rr

To = ambient temperature

q	Temperature ^oC
2784 cal/cm^3 sec	- 50
1789 cal/cm^3 sec	- 10
626 cal/cm^3 sec	21
1126 cal/cm^3 sec	71

The values of the Rg and Rr are given in Section 6. 4. The temperature values are:

Ambient Temperature ^oC	Approximate Temperature in Reversed Zone
- 50	162 ^oC
- 10	135 ^oC
21	98 ^oC
71	389 ^oC

The values of the temperature calculated in this manner range from 100 ^oC to 390 ^oC while those calculated in Appendix 3, using a different approach range from approximately 100 ^oC to 500 ^oC. In both cases a

temperature rise of approximately the same magnitude occurs. From this it can be concluded that a rise in temperature occurs although it is thought to be of a much more localized and intense nature in the slip bands found using the above solution.

APPENDIX 3

Maximum Temperature in the Reversed Plastic Zone as Calculated from a Slip Plane Model

Introduction

The concept of localized heating in the crack tip region has been studied by Freudenthal and Weiner (56), Williams (57) and Rice (58). Overall or homogeneous temperature rises have been observed by Oates (40) and many others. The maximum temperature rise will be calculated according to the method derived by Freudenthal and Weiner as it applies more directly to fatigue.

Thermal Aspects of Fatigue

The basic criterion is that a highly localized temperature is developed in the front of any active slip plane resulting from the conversion of work into heat. When slip proceeds by motions of dislocations under forces applied to the external surfaces of a crystal, the work of these forces, W, is transformed into potential energy of elastic distortion, We, and kinetic energy of the moving dislocations, Wk, and the energy, Wd, irreversibly dissipated in this motion by producing permanent change of shape. Wk is neglected and for relatively large permanent deformations and $We \ll Wd$ which results in $Wd = W$. The dislocations are all considered parallel so the process is two dimensional. It is further assumed that the conversion of mechanical energy into heat takes place on the slip plane over regions of significant atomic misfit, that is over widths of the dislocations, and also that the aggregates of dislocations required to

produce the total slip are separated by the width of an individual dislocation so dislocations form a piled up group. The trail of dislocations on a given slip plane represents a moving band heat source. The heat released over the band source may be estimated as follows:

$$Wd = W = \tau nba$$

where τ is the component of applied stress on the slip plane, a is the area swept out by the dislocation, b is the unit step produced by the motion of a single dislocation and n the number of slip steps to produce the total slip distance $\delta = nb$.

The dislocations move with an average velocity, V, and the work is completed during the time $t = a/V$ so the average rate at which work is done $W/t \approx dW/dt = \tau\delta V$. The width of the dislocation in a slip plane is equal to mb, the length λ of a moving heat source is $\lambda = nmb$ and dW/dt is dissipated uniformly over this length, the uniform heat-flux density q released over a band of length λ is $q = \tau\delta V/nmb = \tau V/m$. The velocity, V, of the moving trail of dislocations is assumed to be between 0.1 and 0.9 the velocity of sound in the material and the distance m between consecutive dislocations is roughly between 3b and 7b. The solution for a moving heat source in an infinite medium can apply to a tiny reversed plastic zone at the tip of a fatigue crack. Considering the band heat source of length, λ, which is taken as the radius of the reversed plastic zone and the flux energy q moving in an infinite medium the heat conduction is governed by the following equation:

$$k(\partial^2 T/\partial x^2 + \partial^2 T/\partial y^2) - V\,\partial T/\partial x = 0$$

The boundary conditions are:

$$-K(\partial T/\partial y) = q/2 \quad \text{for } 0 < x < \lambda;\ y = 0 \qquad \text{and}$$

$$(\partial T/\partial y) = 0 \quad \text{for } x < 0,\ x > \lambda;\ y = 0 \qquad \text{and}$$

$$\lim_{x \to \pm\infty} T = \lim_{y \to \pm\infty} T = 0$$

$T = 0$ is taken as the temperature of the undisturbed temperature of the medium. Heat conduction in the direction of the medium is neglected and the maximum temperature T occurring at $x = \lambda$, $y = 0$ is with the use of $q = \tau V/m$; $T = \tau/mK(k\lambda V/\pi)^{1/2}$

The calculation of the maximum temperature is made substituting in various values of λ and corresponding values of τ for a given strain for each of the four fatigue test temperatures. The maximum temperatures calculated serve only to show that the tip temperature is increased and the values are not to be considered exact. There are many possible reactions and effects that increased temperature may promote. Several of these are listed below and some could become a research topic:

1. thermal softening
2. local precipitation
3. heat straining and oxide formation
4. increased rate of strain-ageing
5. resolution of fine precipitates under action of shear and temperature
6. decrease in local tensile and yield strength depending on actual temperature rise.

7. Possibility of over ageing

8. Much faster diffusion rates of interstitial solute atoms

9. In the case of hydrogen, a much faster and deeper penetration into the specimen due to faster diffusion rates.

10. Formation of compounds such as nitrides, carbides, possible hydrides, which required additional energy in the form of heat.

11. In the case of local heat flashes on individual slip planes, very severe thermal stress gradients which may be in the order of the tensile strength which may be a plausible mechanism of crack initiation.

Calculation of Temperature at Crack Tip

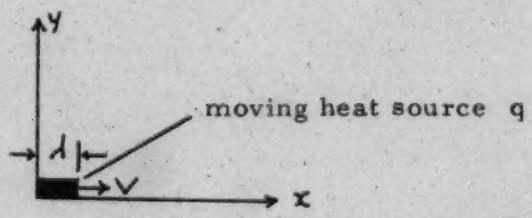

Solution for Moving Heat Source in an Infinite Medium

$$T = \tau/mK\,(k\,\lambda\,V/\pi)^{1/2}$$

T = maximum temperature °C

τ = stress = 1/2 cyclic stress at 0.01 strain

K = thermal conductivity 0.12 cal/sec cm °C

k = thermal diffusivity = $K/\rho c$ = 0.1388 cm^2/sec

m = 5

ρ = density 7.86 gms/cm^3

c = specific heat 0.11 cal/gm °C

V = velocity of dislocation $0.1\,V_o$ - $0.9\,V_o$
V_o = speed of sound in material = 51.3×10^4 cm/sec

d^* = length of band heat source

d^* is taken as radius of reversed plastic zone as measured for each temperature

Temperature °C	d
- 50	1.143×10^{-3} cm
- 10	1.778×10^{-3} cm
21	5.08×10^{-3} cm
71	2.539×10^{-3} cm

Vo = 51.3×10^{4} cm/sec

.1 Vo = 51.3×10^{3} cm/sec

.45 Vo = 23.1×10^{4} cm/sec

.9 Vo = 46.2×10^{4} cm/sec

Temperature °C	τ psi	τ (dynes/cm^2)
- 50	22,750	1.568 x 10
- 10	19,500	1.3444 x 10
21	18,750	1.292 x 10
71	17,250	1.189 x 10

Temperature °C	Dislocation Velocity	Maximum Temperature °C
- 50	.1 Vo	100.46
	.9 Vo	301.3
	.45Vo	213.1
- 10	.1 Vo	107.52
	.9 Vo	322.54
	.45Vo	228.07
21	.1 Vo	174.65
	.9 Vo	523.9
	.45Vo	370.46
71	.1 Vo	113.6
	.9 Vo	340.8
	.45Vo	241.0